

Experimental Analysis of Waves in Environmental Flows

Doctoral dissertation

By: Karim Medjdoub



ELTE
EÖTVÖS LORÁND
UNIVERSITY

EÖTVÖS LORÁND UNIVERSITY, FACULTY OF SCIENCE
DOCTORAL SCHOOL OF ENVIRONMENTAL SCIENCES
ENVIRONMENTAL PHYSICS PROGRAMME

Supervisor: **Dr. Miklós P. Vincze,**

Eötvös Loránd University, Faculty of Science,
von Kármán Laboratory of Environmental Flows

Consultant: **Prof. Dr. Imre M. Jánosi,**

University of Public Service, Faculty of Water Sciences,
Department of Water and Environmental Policy

von Kármán Laboratory

Budapest

2022

Acknowledgments

I thank my eternal almighty Allah, source of will, patience, courage and strength that allowed me to accomplish this work.

I am deeply grateful to my supervisor Dr. Miklós P. Vincze, for continuously guiding and supporting me with patience and dedication by his scientific and moral help during the years of my Ph.D. journey. I highly benefited from the orientations, encouragement and valuable advices.

I warmly express my gratitude for my consultant Prof. Dr. Imre M. Jánosi, for his immense knowledge, experience, and encouragement throughout my academic research and daily life.

I extend my sincere appreciation to the person who taught me how patience is a path to success, my beloved father Elhani. And to whom kept supporting me towards my goals and ambitions, for the patience and encouragement, to my beloved mother Bariza. Special thanks to the companions of a pure and elegant house, my dearest sisters; Amel, Ahlem, and Nesrine for their love, support and encouragement.

I acknowledge the Ministry of Higher Education and Scientific Research (Algeria) and the Tempus Public Foundation (Hungary), for providing me with the *Stipendium Hungaricum* scholarship, funding, and financial support.

The essential contributions of Tamás Tél, Balázs Gyüre, Katalin Ozogány, and the late Adelinda Csapó to the early, exploratory stage of dead water-related research at the Kármán Laboratory, are highly acknowledged. I am also very grateful to Csilla Hrabovszki and her family who provided the ‘red’ ship model.

My research work was supported by the Eötvös Loránd University (ELTE) and the Stipendium Hungaricum Scholarship of the Tempus Public Foundation. Also the János Bolyai Research Scholarship of the Hungarian Academy of Sciences, the National Research Development and Innovation Office (NKFIH), New National Excellence Program of the Ministry of Human Capacities of Hungary, under grant numbers [FK125024 and K125171], and by the ÚNKP- 18-4 New National Excellence Program of the Ministry of Human Capacities of Hungary.

Abstract

This thesis presents three projects; two projects were conducted to study through laboratory experiments the applicability of linear wave theory on the prediction of interfacial internal waves in quasi-two-layer stratified water, and an additional project to study the complementarity of wind and solar energy resources for the electricity production in the north western of Africa.

Interfacial internal wave excitation in the wake of towed ships is studied experimentally in a quasi-two-layer fluid. At a critical ‘resonant’ towing velocity, whose value depends on the structure of the vertical density profile, the amplitude of the internal wave train following the ship reaches a maximum, in unison with the development of a drag force acting on the vessel, known in the maritime literature as ‘dead water’. The amplitudes and wavelengths of the emerging internal waves are evaluated for various ship speeds, ship lengths and stratification profiles. The results are compared to linear two- and three-layer theories of freely propagating waves and lee waves. We find that despite the fact that the observed internal waves can have considerable amplitudes, linear theories can still provide a surprisingly adequate description of subcritical-to-supercritical transition and the associated amplification of internal waves. We argue that the latter can be interpreted as a coalescence of frequencies of two fundamental stable wave motions, namely lee waves and propagating interfacial wave modes.

The damping of water surface standing waves (seiche modes) and the associated excitation of baroclinic internal waves are studied experimentally in a quasi-two-layer laboratory setting with a topographic obstacle at the bottom representing a seabed sill. We find that topography-induced baroclinic wave drag contributes markedly to seiche damping in such systems. Two major pathways of barotropic–baroclinic energy conversions were observed: the stronger one – involving short-wavelength internal modes of large amplitudes – may occur when the node of the surface seiche is situated above the close vicinity of the sill. The weaker, less significant other pathway is the excitation of long waves or internal seiches along the pycnocline that may resonate with the low-frequency components of the decaying surface forcing.

We analyzed wind speed and solar irradiation data of high spatial and temporal resolution for an extended area of north-western Africa including the Mediterranean Sea. We exploit the ERA5 data bank compiled and maintained by the European Centre for Medium Range Weather Forecast (ECMWF). One of the new products they provide is horizontal wind speed components at a height of 100 m (modern wind turbines have a hub height between 80 and 120 m). We demonstrate that the desert area is an optimal location for wind- and solar electricity production for two peculiar aspects. Firstly, the wind speeds at 100 m over the Sahara are al-most as large as wind speeds over the open sea. Wind speed differences between the standard 10 m altitude and 100 m level are considerably larger over the desert area than over the sea. Secondly, there are utilizable anti-correlations between local wind speeds at 100 m and surface solar radiations over the Sahara. As far as we know, such anti-correlations over our target area are not considered until very recently as an exploitable source of combined solar-wind electricity production. We provide a theoretically optimum combination of the two resources in a simple model framework. The result is that resource combinations between 60-40% and 70-30% wind-solar electricity aggregation (depending on the geographic location) provide and optimally smooth output with a minimal loss of total production achieved by either pure wind or pure photo-voltaic generation.

Contents

1	General introduction	1
2	Internal wave generation	3
2.1	Introduction	3
2.2	Stratified water characteristics	6
2.2.1	Instability in stratified flow	7
2.2.2	Definition of the Froude number	10
2.3	Flow-obstacle interaction	10
2.3.1	Barotropic to baroclinic energy transfer	11
2.3.2	Lee waves	15
2.3.3	On the dead water phenomenon	16
2.4	Linear dispersion relation	19
2.4.1	Governing equations of motion	19
2.4.2	Linear stratification	20
2.4.3	Homogeneous deep and shallow water	21
2.4.4	Two-layer approximation	23
2.4.5	Three-layer dispersion relation	24
2.5	Laboratory wave modeling	24
3	Laboratory modeling: methods and setup	28
3.1	Introduction	28
3.2	Experimental wave tanks	28
3.3	Density profiles	31
3.4	Wave excitation	34
3.5	Image processing and projection	35
4	Experimental study of the resonant feature of internal gravity waves in the case of 'dead water' phenomenon	38

4.1	Introduction	38
4.2	Results	39
4.2.1	Qualitative description of the flow	39
4.2.2	Parameter dependence of the critical towing speed	42
4.2.3	Comparison with linear two- and three-layer theories	45
4.2.4	Lee-wave dynamics	48
4.3	Discussion	50
5	Laboratory experiments on the influence of stratification and a bottom sill on seiche damping	53
5.1	Introduction	53
5.2	Results	53
5.2.1	Qualitative description	53
5.2.2	Surface waves	56
5.2.3	Source-filter dynamics	58
5.2.4	Topographic energy conversion	62
5.3	Energy conversion in Gullmar fjord vs laboratory observations	64
5.4	Discussion	66
6	Combined wind-solar electricity production potential over north-western Africa	68
6.1	Introduction	68
6.2	Data and methods	70
6.2.1	Spatial correlations of wind fields	72
6.2.2	Wind electricity estimate	73
6.2.3	Combined solar and wind electricity estimate	73
6.3	Results	75
6.3.1	Mean wind speeds and capacity factors	75
6.3.2	Spatial correlations of wind speeds	78
6.3.3	The correlations of wind speeds vs solar radiations	80
6.3.4	Combined wind-solar electricity production	84
6.4	Discussion	87
7	General conclusion	89

Chapter 1

General introduction

Understanding of the laws of nature and the environmental characteristics enabled humans to adapt and built a convenient medium to serve their benefits, achieving a crucial development we are currently living through, which created a life of well-being and met the increasing needs arising with population growth. Despite the advancement of science and technology, having passed through generations, we still face important issues potentially preventing our survival in many ways. The problems of this world and the degradation of quality of life continue to exist and make the task of mankind in protecting his race more difficult. Such global issues involve climate change and extreme weather patterns that are some of the most pressing issues of our time and in history. It is critical to admit that human activities most likely have the highest impact on the ongoing change of their physical environment. Such actions have important contributions to the increase in the level of greenhouse gases, leading to global warming, global acidification, deoxygenation of the ocean and the rising of the sea surface level [1].

Water bodies significantly contribute to in the energy stored in the climate system, considerably due to the high capacity of heat energy storage and being the source of more than 50% of the atmospheric oxygen. Marine life is affected by the global warming effect of greenhouse gases, pollution and acidity of the water caused by human activities. On the other hand, people, oceans, and the climate are irretrievably linked. Therefore, to take positive actions toward our environment, it is a prerequisite to develop a knowledge-base for better ideas about how the environment works, with an emphasis on the marine environment.

Internal waves are ubiquitous in stratified water bodies with deep water like oceans, seas or fjords, and shallow water such as lakes. They are essential components of the marine ecosystem, carrying a significant physical and biological impact. Energy, heat and momentum are transferred in the ocean for long distances, mainly by nonlinear internal

waves; their breaking enhances the mixing of water components and nutrients, modifying properties of the medium. As a result, they are responsible for substantial ocean mixing, energy dissipation, and thermohaline circulation. They also significantly impact the water temperature in shallow and deep coral reefs by transporting cold and nutrient-rich water in nearshore regions, as well as aggregating phytoplankton near the water surface. Therefore, understanding the behavior of the waves in stratified systems and finding simplified mathematical theories to accurately describe their motion will lead to an increase in the accuracy of climatological models.

It is realized that linear wave theory is the simplest way to describe the propagation of wave phenomena. However, it is also known that there are limitations due to nonlinearity, which is a topic of focus in numerous studies. The topic of the thesis follows an experimental based study, predominantly focusing on the extent of the applicability of linear wave theories in understanding and predicting nonlinear internal waves phenomena in quasi-two-layer stratified water.

The use of fossil fuels as a source of energy is undoubtedly the largest source of greenhouse gas emission. Therefore, dependence on renewable energy is considered as the most needed action to avoid the harmful effects of climate change [2]. Despite the urgency to use renewable energy, we still face several challenges such as the high fluctuation energy pattern and the lack of sufficient storage technology. In order to accelerate the replacement of fossil fuels with renewable energy, combining multiple sources can contribute towards maximising and smoothing the electricity production signal. A secondary topic for the thesis is a statistical optimisation on the combination of two sustainable forms of energy (wind and solar) over north-western Africa.

Chapter 2

Internal wave generation

2.1 Introduction

Waves are familiar to humans due to their ubiquity in the environment, including those that appear on the surface of water bodies, which cover more than two thirds of Earth's area. The wave propagates as a result of certain imbalance of energy in the water, yielding an oscillatory interchange between kinetic energy and potential energy of the water parcels [3]. Although, surface waves are noticeable even to the unaided eye, internal waves are rather complicated to detect, even with the powerful tools of remote sensing such as the aerial and space photography, synthetic aperture radars (SAR) mounted on aircraft and satellites, shore based- and ship-based radars. That is because the internal interfacial waves are gravity waves exist along the sharp or diffuse interface between layers of water of different densities.

A classical example of a relatively easily detectable interfacial wave is in the the Strait of Gibraltar region that separates the tip of the Iberian Peninsula (Spain) and Tangier in Morocco, and constitutes the only natural link connecting the Atlantic Ocean with Mediterranean Sea (Alboran Sea). Due to the shallowness and transparency of the upper (less saline) layer, the internal waves that are created by this particular bathymetric formation are visible from the space shuttle; such as those which propagate towards the Mediterranean Sea – the main interfacial waves are produced due the presence of the highest sill in the strait (Camarinal sill) – as photographed by an astronaut from the space shuttle (See Fig. 2.1 by Alpers et al. [4]). Here the lower layer consists of saltier water from the Alboran Sea (salinity approximately 38 PSU – practical salinity units) and the top layer is made up of a lighter water from the Atlantic Ocean (salinity approximately 36 PSU) [5]. This stratification is composed of the water flowing from the Atlantic into



Figure 2.1: **Astronaut photograph taken from the space shuttle for the Strait of Gibraltar "STS-41-G missions in October 1984, 11st at 12:22 UTC".** It displays two internal wave pockets propagating into Mediterranean sea, (the astronaut: Paul Scully-Power) [4].

the Mediterranean, while a counterflow is propagating below it from the Mediterranean water. The Eastward wave pocket to the Mediterranean Sea contains a group of individual solitons (nonlinear internal waves with characterized by large amplitude) that propagate with different velocities, and are generated by the semidiurnal internal tide that have extremely large peak-to-through amplitudes – the full vertical displacement – reaching up to 200 m [6], and the velocity of tidal current over Camarinal sill is controlled mainly by the barotropic tides [7]. A westward-propagating internal wave pocket, or – in case of supercritical flow – an undular bore can also develop, however it is much weaker than its Eastward-propagating counterpart [8, 9].

Radar imaging theory based photography of the Strait of Gibraltar in Fig. 2.1 exhibits light and dark bands which are created through distinguishing the roughness of the water surface by means of “Bragg Scattering”. It enhances the returned radar signal that vary affected by the convergence and divergence of the internal wave crest, in which the rough surface tends to appear lighter in contrary of the smooth surface is much darker [10, 11].

E.g., Fig. 1 in Ref. [12] by the Global Ocean Associates, shows the locations internal waves of large amplitudes that occurs within the global water bodies; 54 regions where the internal waves are discovered in the global environment, mainly based on water surface signatures in remote sensing images.

In natural water bodies, surface waves can be generated due to several reasons: e.g. tidal attraction, seismic earth activity, ships motion, and more frequently wind stress along the water-air interface causing a disturbance of the water surface, and thus the movement of surface water to a non-equilibrium state. Subsequently, gravity plays a role of the restoring force acting on the water – after it gains a potential energy – and works on returning it to the equilibrium state in wave-like motion due to the potential kinetic energy exchange. Water-air interface is between two fluids of high density difference; this keeps the gravity effect strong and yield considerable wave frequencies. In comparison with small density differences – air-air or water-water interfaces – between two layers of the same fluid the gravity acceleration g is reduced to g' ($g' = g\Delta\rho/\rho_0$), and causes slower oscillations of the interface, yielding small frequency and large wavelength. Several external forces may contribute to generating internal perturbations; it is significantly driven by barotropic or baroclinic tidal currents interacting with bottom topography; e.g. submerged mountains, ridges or continental shelves [13]. Internal tides were observed first by Fridtjóf Nansen in his expedition to the North Pole [14], motivating the early experimental studies conducted by Nils Zeilon [15, 16] on the generation of tidal interfacial waves of two-layer stratified flow.

Important portion of barotropic tidal energy is converted into internal waves or internal tides by forcing the baroclinic vertical displacement in the deep ocean with the presence of rough bottom topography [17, 18], which radiate into the open ocean, as it may dissipate locally leading to a vertical mixing near to the obstacle or the breaking of the internal waves occurs far further [19]. These types of waves are observed in different regions of the ocean, e.g. Hawaiian Ridge [20], Mid-Atlantic Ridge in the Brazil Basin [21]. Also for smaller reservoirs, multiple fjords got attention of oceanographers because of the interesting properties of the bottom topography within enclosed or semi enclosed silled basins and cases where two basins are separated by a sill [22], like Canadian fjords [23], Scandinavian fjords [24], and particularly the fast damping of their barotropic seiches due to the barotropic to baroclinic energy transfer [25]. Apel et al [26] concluded that the height efficiency of vertical mixing comes along with the dissipation of the internal seiche (internal standing wave). The mechanism of the internal wave generation from barotropic to baroclinic energy transfer is further explained in the subsection 2.3.1, as well as seiche damping caused by the flat and rough bottom topographies.

2.2 Stratified water characteristics

Large number of water bodies such as Oceans, Seas, Fjords and Lakes are formed of stratified water for a certain period, either permanent or temporary [27, 28]. The density variability along the water depth is caused by several factors: salinity, temperature, sedimentation, suspension of materials. The layer where the vertical salinity profile exhibits the strongest gradient is called *halocline*, and its analogue for temperature is the *thermocline*. Due to the direct contact with the the air and solar irradiance, the water surface receives more heat and becomes warmer than the deep basin, therefore lighter to cause a stable stratified system; where a longer period of hot weather leads to stronger stratification. contrarily, in winter the water surface becomes cooler, thus denser creating unstable medium that boosts vertical water circulation.

Salinity is the concentration of ions in a volume of water [29] (mostly sodium and chloride which strongly contribute to the variation of water density). At latitudes, intense evaporation of water increases the salinity of the surface waters. However, does not yield unstable density stratification, as large as its effect is compensated by thermal expansion [30, 31]. At high latitudes, the density in the surface is affected by the freezing and the melting process; in polar regions ice is a fresh water with very low salinity (brackish), it keeps the surface of water at lower salinity and therefore less dense. The water density in cold areas decreases with the temperature in the interval: $T > 4^{\circ}\text{C}$, and when the water temperature T is less than 4°C the density increases with temperature (the highest peak density is corresponds to $T = 4^{\circ}\text{C}$). In contrary of the equatorial regions which exhibit only negative linear relationship between density and temperature of water, so the density decreases with increases of temperature. Distinctly, the oceans and seas show high salinity concentration, and even some lakes show high salinity beyond the ocean concentration [32]. The density gradient can be found in the vicinity of external inflow like groundwater seepage, water from melted iceberg; also the decomposition of organic matters changes the water composition that leads to the decantation of several matters such calcite [28]. Another factor is the pressure with considerable effect on the density of the water in the deep ocean in the deep ocean.

Density strongly depends on temperature and salinity; The simplified Equation (Eq. 2.1) shows the variation of the density anomaly σ as a function of water temperature T , salinity S , water thermal expansion coefficient α_T and the coefficient of dependence of density on salinity β_S in which σ_0 , T_0 and S_0 are the reference density, temperature and salinity values respectively.

$$\sigma = \sigma_0 + \rho_{\text{ref}}(-\alpha_T[T - T_0] + \beta_S[S - S_0]) \quad (2.1)$$

Where

$$\beta_S = \frac{1}{\rho_{\text{ref}}} \frac{\partial \rho}{\partial S} \quad \alpha_T = -\frac{1}{\rho_{\text{ref}}} \frac{\partial \rho}{\partial T}$$

Equation 2.1 obtained by drawing short lines tangent to the isopleths of σ in the figure 2.2

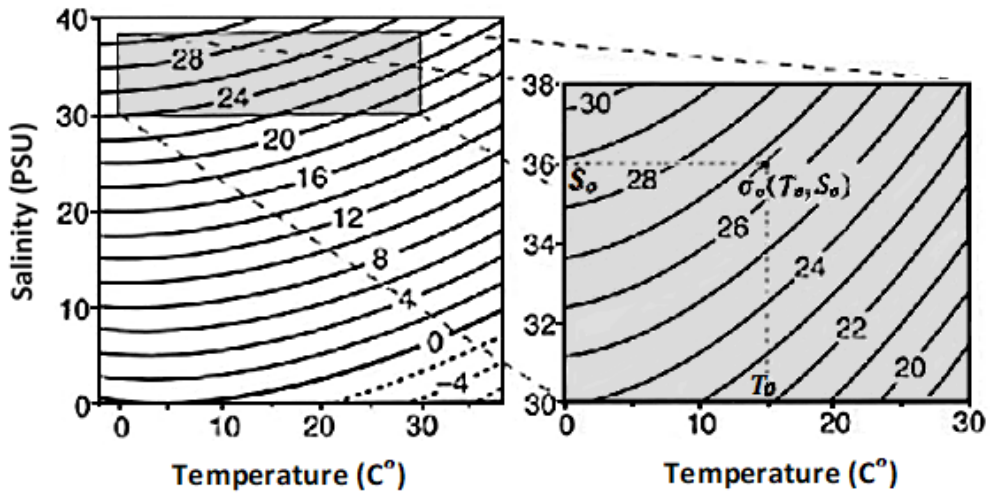


Figure 2.2: Seawater density anomalies ($\sigma = \rho - \rho_{\text{ref}}$ in kg m^{-3}) as a function of salinity (in $\text{psu} = \text{g.kg}^{-1}$) and temperature (C°) at the level of sea surface. Note that the density anomalies σ in the open ocean is within the range $[20-29] \text{ kg m}^{-3}$, while Temperature $T \in [0-30] C^\circ$ and Salinity $S \in [33-36] \text{ psu}$. The zoomed panel in right indicate the oceanic relevance range (Ref. [33]).

2.2.1 Instability in stratified flow

Frequently, the flow currents in the environment are driven by gravity and density, whether in the atmosphere or the ocean. One of the crucial keys of the flow induced instability is the rise of potential energy in a certain stratification characteristics, when the heavier medium in lower altitude is exposed to heat that leads to a convection caused by the means of thermal expansion [34]; and shear stress from the pre-existing kinetic energy of the disturbance of the interface of stratified flow specified by two superposed homogeneous fluid layers of adjacent horizontal domains of different velocities [35]. Such energy carried within the mean flow may be transferred to traveling waves [36, 37].

A system is considered unstable when its state gets further from equilibrium as a response to any perturbation. whereas a stable system responds by driving its state back to its equilibrium. In our case, the restoring force acting on the considered systems is gravity.

If we assume a fluid parcel of horizontal cross-section ∂A and height ∂z_p is displaced vertically by a distance z' from a medium of position z with equivalent density $\rho_p = \rho(z)$ to another with a different density $\rho(z + z')$ in a position $(z + z')$ so that $\rho(z + z') < \rho(z)$, that causes the parcel to gain a potential energy that pushes the parcel to turn back towards its original position of hydrostatic equilibrium state.

Using Newton's second law ($\sum F = ma$) the net external forces acting on the parcel in the vertical direction can be written as:

$$F_{\text{up}} + F_{\text{down}} + F_{\text{P}} = m \frac{\partial^2 z'}{\partial t^2} , \quad (2.2)$$

where the weight of the parcel

$$F_{\text{P}} = g \rho_p \partial A \partial z_p . \quad (2.3)$$

The external force of the environment on the parcel (buoyancy force), the resultant force of upward and downward hydrostatic pressure represented in F_{up} and F_{down} are respectively;

$$F_{\text{up}} + F_{\text{down}} = g \rho(z + z') \partial A \partial z_p , \quad (2.4)$$

$$g \rho_p \partial A \partial z_p \frac{\partial^2 z'}{\partial t^2} = g \partial A \partial z_p (\rho(z + z') - \rho(z)) , \quad (2.5)$$

$$\frac{\partial^2 z'}{\partial t^2} = \frac{g}{\rho_p} (\rho(z + z') - \rho(z)) , \quad (2.6)$$

the linear approximation of $(\rho(z + z') - \rho(z))$ is $\frac{\partial \rho(z)}{\partial z} z'$, thus after replacing it in (2.6) we get:

$$\frac{\partial^2 z'}{\partial t^2} = \frac{g}{\rho_p} \frac{\partial \rho(z)}{\partial z} z' . \quad (2.7)$$

Based on the variation of density according to the height we distinguish the state of the environment (see Fig. 2.3), so it is unstable if:

$$\frac{\partial \rho(z)}{\partial z} > 0 ,$$

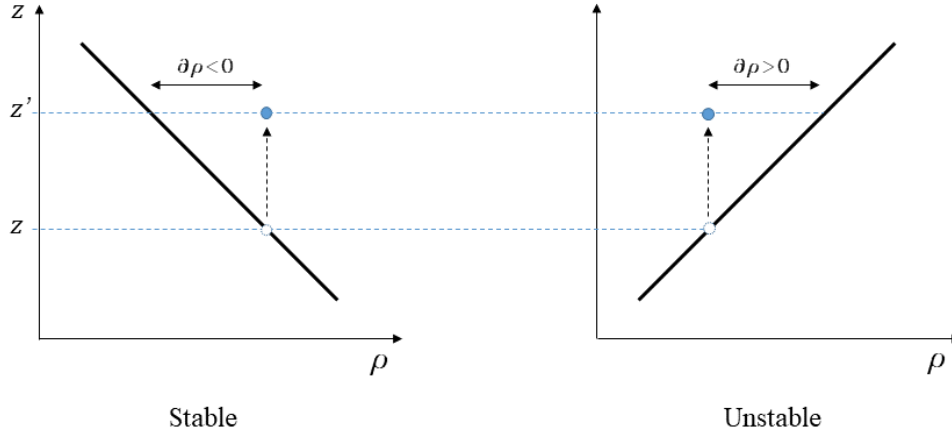


Figure 2.3: **Schematic for the stability and instability of displaced fluid parcel.** The black line is the monotonic relationship between the density ρ and height z . The parcel moves from initial position z 'white circle' to position z' 'blue'.

and it is a stable environment in the case that:

$$\frac{\partial \rho(z)}{\partial z} < 0 .$$

Brunt-Väisälä frequency

The differential equation (2.7) has a solution for the stable system (negative $\frac{\partial \rho(z)}{\partial z}$), in which the vertically displaced parcel is in oscillatory motion characterized by the frequency N in a continuous stratified layer (a layer identified by a constant density gradient in height z), the concerned frequency is called Brunt-Väisälä or buoyancy-frequency, what it is written as:

$$N \equiv \sqrt{-\frac{g}{\rho_0} \frac{\partial \rho(z)}{\partial z}} , \quad (2.8)$$

here $\rho_0 = 1 \text{ kg/l}$ is a reference density that describe the density of the parcel in fresh water.

In multi-layer stratified fluid each layer characterized by different buoyancy frequency, therefore the above equation can be written as:

$$N_j \equiv \sqrt{-\frac{g}{\rho_0} \frac{d\rho}{dz} \Big|_j} . \quad (2.9)$$

in which every layer can be indexed differently as $j = 1, 2, 3, \dots$ depending on the number of layers and also by their approximate thicknesses h_j .

2.2.2 Definition of the Froude number

Generally, Froude number Fr is the quantity that represents the ratio of velocities due to inertia and due to gravity, describing the disturbance of a system and wave propagation state by the dominant forces acting on the flow, which affect substantially the kinetic energy and the potential energy. Froude number identifies subcritical ($Fr < 1$), supercritical ($Fr > 1$) and critical flows ($Fr = 1$).

The expression that is in general use for open channels is $Fr = v/C$, where v is the flow mean velocity and C is the maximum celerity of free propagating waves that can be reached in such homogeneous fluid system. In a simple case of inviscid flow, Froude number is written as $Fr = v/\sqrt{gH}$, H is the vertical scale that represent the total depth of the water (usually for shallow water); when the bottom is characterized by small horizontal topographic boundary, the length scale in Froude number is replaced by length of topography (obstacle) L_{obs} that is interacted with the flow. However, in stratified fluids the reduced gravity g' is taken into account, so the internal Froude number in two-layer stratified system with a top layer of h_1 height superposed over layer h_2 is often written as $Fr = v/\sqrt{g'H_r}$, the expression we used concerning that the water is shallow; $H_r = (h_1h_2/H)$ represent the characteristic vertical scale of the two-layer stratification, the so-called 'reduced height'. In continues stratification $Fr = v/NH$ is used mostly in the applications regarding to lee waves where the spatial scales of the mountains are so small compared to the thickness of atmospheric layers.

2.3 Flow-obstacle interaction

The geometry of bottom topography plays a crucial role in the environmental fluid transport, mixing and changing of the flow circulation in the atmosphere or water bodies, and hence the pattern of energy distribution within the fluid body [38, 39]. When the flow in the bottom layer of a stratified fluid is forced by a shallow uneven topographic obstacle such as a bottom sill, it causes a change in the resultant vertical forces which yield a perturbation of the interface between the fluid layers. Different types of interfacial waves are induced by this vertical periodic motion of the fluid traveling and carrying kinetic energy and medium characteristics away from that topographic obstacle.

Due to the crucial impact of the bottom topography on the water circulation in stratified media, numerous researches focused on the concerned influence of the shape, asymmetry, dimensions of the basin topography on the enhancement of vertical diffusion, turbulence and wave generation; e.g. the asymmetry of the reservoirs affects the vertical

structure of the seiche (standing wave), and flow current concentration zones where the medium is led to a higher mixing in the case of continuous (linear) stratification (the study was investigated numerically by Münnich et al [40]).

The internal solitary wave generated at the pycnocline (two-layer stratification) by the presence of the bottom sill can be modified to a standing wave at the the presence of the second sill of the same height [41, 42], or in the case of jet produced by single sill is intensified with the presence two sills [41] as observed in increasing of mixing rate in the Ringdalsfjord-Idefjord at the Swedish-Norwegian border between Bjallvarpet and Svinesund sills [43].

The forthcoming subsections present the detailed impact of the bottom topography (single sill/obstacle) on the distribution, conversion in stratified system.

2.3.1 Barotropic to baroclinic energy transfer

Water circulation distribution and mixing led by energy conversion over bathymetric formations is an important part of the global ocean dynamics [44]. The coupling between barotropic tidal waves at the sea surface and internal gravity waves facilitates heat and material exchange between the uppermost and deeper layers [45, 46, 47, 48, 49, 50]. This largely interconnected dynamics is particularly pertinent in semi-enclosed basins, bays, and fjords with density profiles characterized by sharp gradients [24, 25, 40, 43, 50, 51, 52, 53, 54, 55, 56, 57, 58, 59, 60, 61, 62, 63, 63, 64, 65, 66, 67].

The exchange between waves at the surface and at the pycnocline can be especially well studied in the situation where standing waves develop at the water surface, known as seiches [68, 69]. Such oscillatory motions of a water body are typically initiated by temporally changing wind stress, especially pulse-like wind bursts, or storms. Strong wind shear gets balanced by a certain tilt of the water surface throughout the basin, but when the storm subsides, the restoring forces, predominantly gravity, yield a damped “sloshing” of the free surface, until it settles in its equilibrium (horizontal) position. Tidal barotropic waves, even tsunamis and other seismic disturbances are known to generate large inflows into coastal harbors and may also yield strong seiche activity [68].

Energy dissipation in seiche modes

The energy dissipation rate (or decay rate) of surface seiches in natural enclosed water bodies, e.g. lakes or fjords is determined by the physical properties of the fluid body (e.g. its stratification profile) and the geometry of the basin. In the presence of bottom topography, surface gravity waves generate internal waves, a process also referred to as

barotropic to baroclinic energy conversion, or – in the specific case of tidal surface waves – tidal conversion. The first demonstration of such a wave excitation mechanism over a tilted bottom topography dates back to the work of [51] in the case of a two-layer stratification. [52] explained the observed current oscillation at the Florida Straits with the interaction of barotropic tides and the continental slope that yields a generation of baroclinic tidal waves, periodically modulating the flow. Although these pioneering studies did not consider the dissipative effect of the excited baroclinic modes on the surface waves, it is obvious that freely propagating internal waves use up a significant fraction of the energy stored in the e oscillations, and hence speed up the decay of the latter.

There are, however, substantial differences between the seiche modes excited in enclosed and semi-enclosed basins. In the former configurations the boundary conditions “select” such standing waves that have antinodes at all boundaries (at least in the idealized case of vertical sidewalls), whereas, in the semi-enclosed systems the open boundary (e.g. the mouth of the bay) facilitates maximum horizontal flux, leading to the formation of a wave node at the surface. Obviously, the internal waves generated by the waves over topographic obstacles may also exhibit different behaviour in the two settings. In the semi-infinite domain travelling internal waves are excited which “radiate” away the kinetic energy of the surface waves when the topographic obstacles at the bottom reach up to the pycnocline [70]. If, however, the basin is closed, resonant mode selection can also occur as internal seiches are generated at the pycnocline.

The effect of damping on the frequencies of the seiche modes was addressed by the paper of [60] who concluded that in enclosed water bodies the oscillation periods of surface seiche modes do not depend on the stratification significantly. However, in semi-enclosed systems the surface seiche period was found to be more sensitive to the stratification. This effect of internal wave excitation on the decay of surface seiches was further investigated by [71]. When the characteristic (e.g. diurnal) frequency of the wind forcing matches that of a seiche eigenmode, a resonant amplification of the latter may occur. However, as the seasonal changes of the freshwater inflow (e.g. from glacier runoff) influence the depth of the pycnocline, the natural frequencies of the internal waves also change, and – as the resonant frequencies shift – so does the decay coefficient of the dominant surface seiche mode, as shown by [57, 58]

The basin geometry of certain fjords, e.g. the Gullmar fjord of Sweden is especially interesting, as their bottom topography involves a sill reaching up to the pycnocline between the saline seawater and the upper freshwater layer, see the example sketched in Fig. 2.4, taken from Stigebrandt [72]. Parsmar et al [25] investigated the damping of tidally excited surface seiches in the Gullmar fjord and concluded that the drag caused by baroclinic

internal wave excitation at the sill contributes far more to the damping of the seiche than bottom friction or other phenomena.

Barotropic-baroclinic coupling

When the surface seiche oscillates back and forth, it creates a barotropic flow over the topographic obstacle. The obstacle blocks the horizontal flow in the bottom domain, while the top layer flow can maintain its horizontal velocity. The experimental investigation on internal waves conducted by Andow et al [37] in a stratified shear flow demonstrated that the interface disturbance is led by the flow velocity differences between the upper and lower layer of stratified water. In fjord stratification the denser layer trapped by the bottom sill, in which the pycnocline exists at the level of the sill; so the denser fluid lifts above the sill level and thus it can pass over it and create progressive waves traveling on the downstream side [56]). The sketch in 2.4 by [72] displays four types of seiche energy lose, and the pycnocline behavior in enclosed or semienclosed fjords due to baroclinic to barotropic energy transfer forced by the presence of bottom sill at the level of interface.

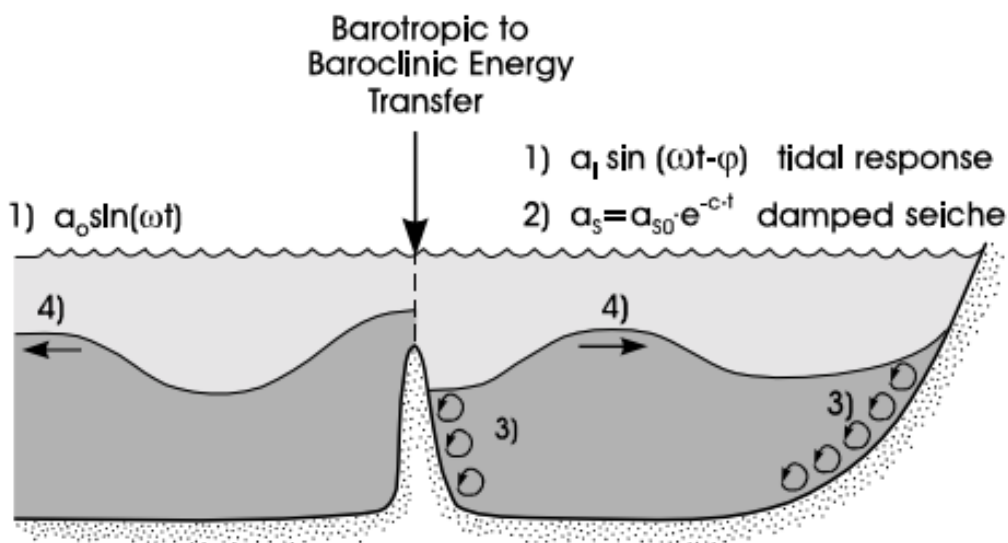


Figure 2.4: Sketch explains the barotropic and baroclinic waves propagation on fjords characterized by a sill located in the mouth: (1) Tidal response in fjords, (2) damping of surface seiches, (3) diapycnal mixing, and (4) interfacial waves radiation from the sill (Ref. [72]).

The barotropic tides entering and reflecting in a narrow bays such as fjord basins is transformed to take a form of a barotropic seiche as a tidal response, in which part of its energy is transferred to baroclinic layer where it is dissipated locally by turbulence

and diapycnal mixing or/and it is carried in a form of progressive waves with a possible strong non-linearity – they are generated in the occasions when the flow over the sill is critical or subcritical characterized by a densimetric Froude number $Fr \leq 1$ – traveling away from the sill that usually dominating the energy lose in fjords dynamics, these waves may radiate back or dissipate in a remote place depending on the form of the basin [67].

Fig. 2.3.1 illustrates horizontal flow from denser layer in two layer stratified water over the sill caused by small difference of surface water level in the laboratory tank established by [73]; small perturbation in surface seiche led to strong shear in the interface near to the sill, subsequently the level of the pycnocline between the sill sides set apart leading to horizontal pressure drive a strong horizontal motion of the water from the bottom layer in the highest level to lower level of pycnocline on the sill.

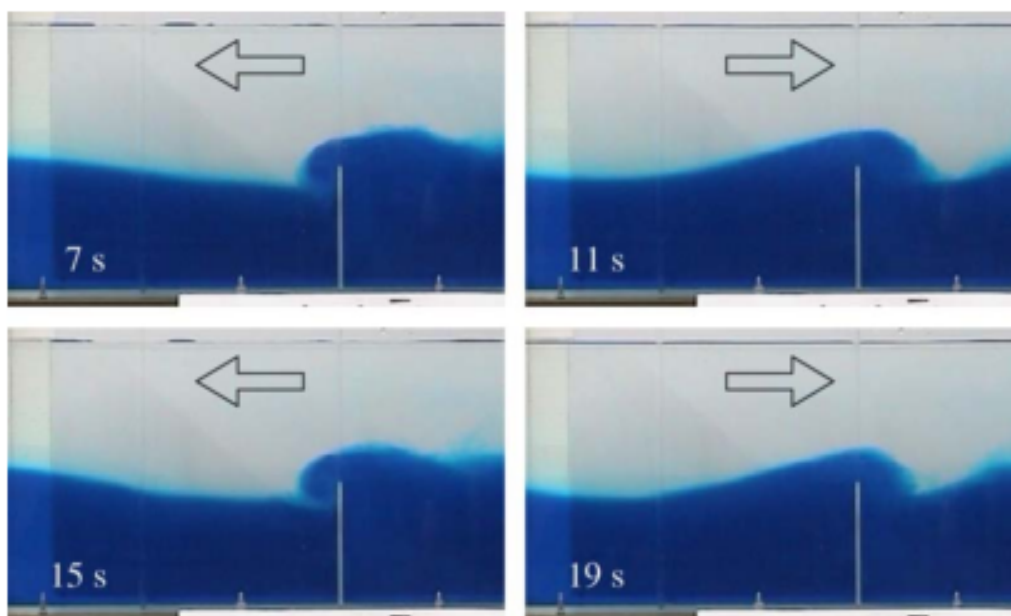


Figure 2.5: **Pycnocline motion over a sill of height 9 cm after an instant excitation of water surface in two layer stratification.** Time and flow direction are indicated (Ref. [73]).

Laboratory work [74] investigated interfacial internal wave generation experimentally in a quasi-two-layer wave-tank with a bottom obstacle at its center, reaching up to the pycnocline, motivated by the fjord geometry. It was found that shear instability developed at the tip of the obstacle and the emerging billows press down the pycnocline at the lee side of the obstacle (with respect to the direction of the oscillating horizontal flow in the upper layer) and generate the observed internal waves. However, the energetics of the damping of surface seiches was not addressed there.

Internal wave excitation by surface seiche modes has also been investigated in laboratory experiments by [61]. They modeled resonant barotropic-baroclinic energy conversion of a periodically forced shallow water system in a rectangular tank without topographic obstacles in order to quantify the energy flux pathways between the applied forcing and the internal wave field. A similar setting (i.e. a rectangular tank with a flat bottom) has also been studied recently by [66], with a special focus on internal wave excitation and seiche damping. Similar laboratory models can provide illuminating results for the interpretation of direct oceanic observations, because they make possible to focus on specific phenomena that are inevitably loaded with disturbing effects in natural environments.

2.3.2 Lee waves

Generally, the wind blowing in the lower altitude of the troposphere may be blocked by mountains which force the upward motion of the air flow at the upstream side. In stable linearly stratified atmosphere, the upward movement of the denser air from a lower level to an upper level uphill by a sufficient vertical force reach to an environment of lighter surrounding atmosphere; subsequently that air will be forced to sink down in the lee side of the mountain under the response of gravity as what is called buoyancy effect. Simply, a *lee wave* (mountain wave) is formed by this up and down motion of the air while maintaining the original horizontal flow speed. When all energy is confined to the lower altitude of the atmosphere, vertical wave propagation occurs, and excites trapped waves in certain levels within the troposphere.

Lee waves can be remarkable by human eyes when air moisture condense in the crest of lee waves in a form of lines, as shown in Fig. 2.6. The reason behind these lines of clouds is that when a moisture oscillates within the air parcel, it condenses in each phase when they reach a higher level, due to the fact that the temperature in troposphere decrease with altitude.

A simpler visible analogy in the nature is a shallow river flow or a stream of high velocity (supercritical flow), and consequently a sufficient kinetic energy that push the water surface to rise over the obstacles in the river bed, and down afterward in the downstream side of the obstacle. The resultant is undular water surface (case slightly Froude number greater than 1) due that the very sharp density difference between water and air. The aforementioned regime is presented in Ref. [76] that studied classification scheme for a single layer flows over a fixed obstacle. Not visible lee waves are observed in the deep ocean [77], mesoscale ocean [78], and also observed shallow water bodies such as the strait of Gibraltar [79].

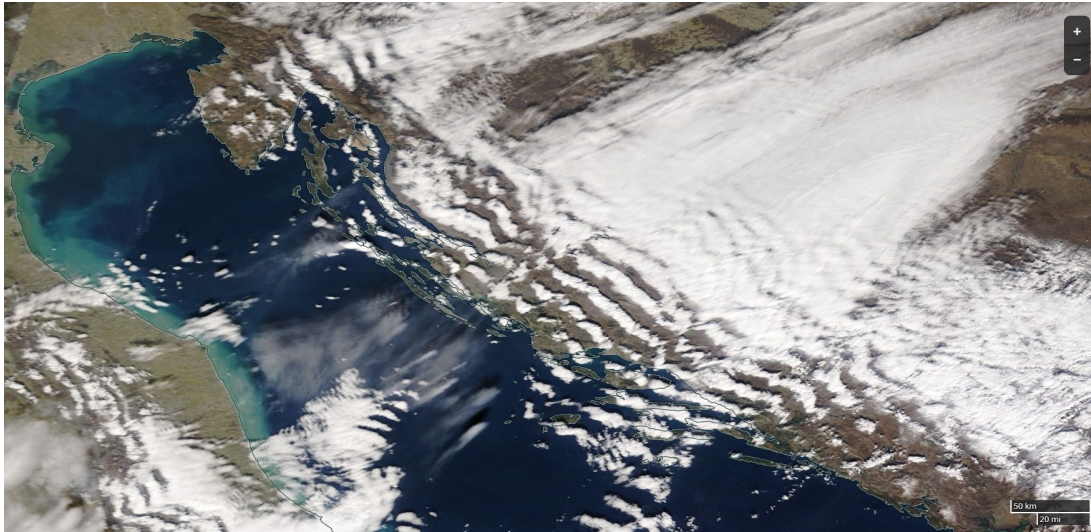


Figure 2.6: **Lee wave clouds above the Adriatic sea.** The photograph was taken on Monday Feb 25th, the clouds formed white lanes by accumulating in the crests of waves (Ref. [75]).

2.3.3 On the dead water phenomenon

When a ship is travelling through a strongly stratified water body a certain amount of its kinetic energy is being used up for the excitation of internal waves in its wake, hardly noticeable from the surface, yet perceived as a drag force acting on the vessel. For centuries, the phenomenon has been known to Norwegian seamen as “dödvand” or dead water and it was experienced by several sailors in which they observed extreme reducing in the ships speeds almost to standstill in certain localities in the near Siberian sea, Norwegian fjords, rip between rivers and seas as in the Congo river, Georgia strait... In the fjords of the Scandinavian coastline fresh water from slow glacier runoff gently sets on top of the saline seawater without substantial mixing and hence nearly jump-wise vertical density profiles can develop [25]. These circumstances facilitate particularly strong dead water effect associated with large amplitude wave activity along the internal density interface (pycnocline).

Ekman’s work on the dead water phenomenon

In the logbook of the 1893-96 Norwegian Polar Expedition Arctic explorer Fridtjof Nansen reported experiencing marked dead water drag on board research vessel *Fram* that reduced the ship’s speed to a fifth part. Nansen’s original observations were further analyzed by (the then-PhD student) V. W. Ekman, who, in order to understand the phenomenon, has conducted laboratory experiments in a quasi-two-dimensional wavetank, filled up

with a two-layer working fluid consisting of saline- and freshwater, after the early suggested explanation by prof. Bjerknes that the reason the *Fram* lose speed is her movement on fresh water (or brackish) layer which itself rest on salty (denser) layer [80]. In these measurements a scale model of *Fram* was towed along the surface subjected to either constant or gradually changing force as control parameter, against which the model's velocity U was measured [81]. Ekman found that for smaller towing forces (and smaller U) dead water drag F_{dw} follows a quadratic scaling $F_{\text{dw}} \approx \zeta U^2$ up to a certain threshold, where coefficient ζ is a function of the density profile $\rho(z)$ and the wetted area of the ship.

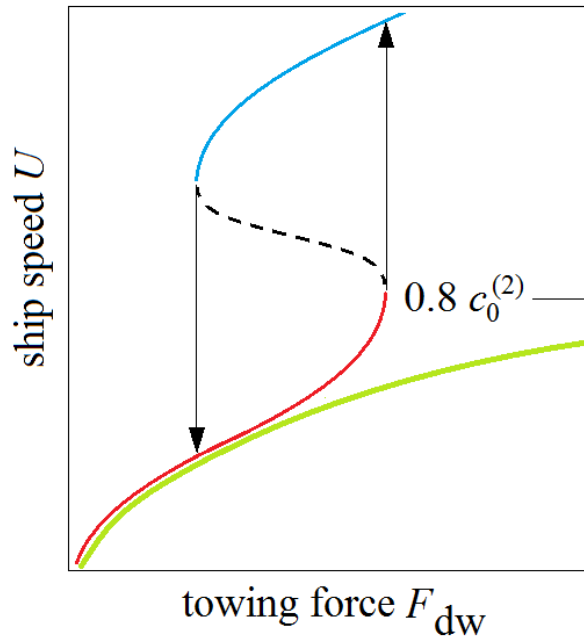


Figure 2.7: **Hysteresis of ship speed – as observed and discussed by Ekman in his original work – illustrated graphically as a function of changing towing force (decreasing branch: blue, increasing branch: red).** The unstable branch is marked with a dashed line. The green curve represents the (inverse of) subcritical relationship $F_{\text{dw}} \approx \zeta U^2$.

However, when U reaches a critical value of $U \approx 0.8 \cdot c_0^{(2)}$, where $c_0^{(2)}$ denotes the long-wave velocity of interfacial waves on the pycnocline (to be discussed later) the corresponding F_{dw} starts to decrease significantly. At this domain, where the Froude number $Fr \equiv U/c_0^{(2)}$ is in the range of $0.8 - 1$ the drag acting on the ship reaches a maximum, coincidentally with the excitation of interfacial waves of the largest amplitude along the pycnocline.

Then, in Ekman's "changing force"-type experiments a hysteresis was encountered,

as sketched in Fig. 2.7. When the gradually increasing towing force reached a certain tipping point (the right end of the red branch in Fig. 2.7) the speed of the ship suddenly jumped to a higher value. An analogous drop of U could be observed when decreasing the towing force in time (blue branch of Fig. 2.7). The unstable branch (dashed line) is inaccessible to the system for any prescribed towing force. When initiating experiments with a *constant* force within this hysteretic regime, Ekman found that the ship’s velocity U exhibited large fluctuations, comparable to the mean value [81].

If one intends to explore the dynamics in this unstable branch it is therefore beneficial to conduct experiments in which, instead of the applied force, the towing velocity U is prescribed. Such settings are common in the laboratory modeling of lee-wave dynamics (see, e.g. [82, 83, 84, 85], where obstacles of various shapes are being towed at the surface (or at the bottom) in a tank of stratified working fluid and the properties of the generated internal waves, hydraulic jumps and ‘wave rotors’ are evaluated [86, 87, 88].

The non-linear nature of interfacial waves

In the experimental work presented in the chapter 4 of the thesis we follow a similar approach to address the dead water phenomenon, by pulling a ship model at a constant speed and – instead of the experienced drag – analyzing the properties of the excited interfacial waves on the pycnocline. Here the ‘critical regime’ is characterized by wave patterns whose vertical extent is comparable to the height of the upper layer. The fact that wave amplitudes show strong dependence on the wave velocity (that is set by ship speed U) implies that the waves are of nonlinear nature [89]. Even for velocities where no wave trains are observed, the localized bump following the ship at the pycnocline resembles the solitary wave solutions of the nonlinear Korteweg–de Vries equation [42, 90].

A large pool of theoretical, numerical and experimental studies exists discussing the properties of internal waves emerging in the dead water problem addressing nonlinear wave excitation both in the subcritical [91, 92, 93] and supercritical [94, 95] regimes, as well as the applicability of the theoretical findings to observational data, including the historical logs of *Fram* [96].

The aforementioned characteristic feature of dead water phenomenon that internal wave drag (and amplitude) exhibits a peak at around $Fr \approx 0.8 - 1$ can already be explained in linearized finite-depth two-layer theories, as shown by e.g.[97, 98]. Despite of the obvious nonlinearity of the problem, as far as the large-amplitude interfacial wave forms are concerned when this peak is encountered, the effect of nonlinear corrections is often found to be surprisingly minor in this respect (see, e.g. Fig. 5 of [94]. Also

in a series of laboratory experiments on topography-induced large amplitude interfacial waves by [74] who have also demonstrated that linear three-layer theories, e.g. the one of Fructus & Grue [99] may yield remarkably good fits to experimental data.

2.4 Linear dispersion relation

2.4.1 Governing equations of motion

Dispersive waves have different phase speeds for different wavelengths; eventually, the dispersion relation describes the connection between the frequency and the wave-number, and therefore the dependence of the phase velocity on the wavelength.

Solving the mathematical equation of the conservation of momentum able to give several dispersion relationships for the surface and internal waves according to the boundary conditions. In environmental hydrodynamics Navier-Stokes is the governing equation of the flow motion that is written as:

$$\frac{\partial u}{\partial t} + (u \cdot \nabla)u = -\frac{1}{\rho_0} \nabla P + g + \nu \nabla^2 u - \mathcal{F} \hat{z} \times u \quad , \quad (2.10)$$

where, u is the flow velocity, ν the kinematic viscosity of the fluid and \mathcal{F} is Coriolis parameter.

It is still difficult to find an exact solution of the wave motion due to the non-linearity that is presented within the equation of motion. The term $(u \cdot \nabla)u$ is clearly visible as the nonlinear term in equation. So, there is a possibility of removing that term to linearize the problem, via assuming a propagating wave characterized by a small amplitude; where the changes in velocity, density and pressure also remain small. Linear solution of the equation of motion still work well as long as amplitude of the waves remain sufficiently small.

For further simplification to the governing equations after assuming that the flow is inviscid by neglecting the viscosity; also neglecting Coriolis effect as $\omega^2 \gg \mathcal{F}^2$. Therefore, we obtain a linearized Euler's equation in which can be used and written as:

$$\frac{\partial u}{\partial t} + \frac{1}{\rho} \nabla P - g = 0 \quad (2.11)$$

Assuming incompressible flow, the equation of continuity expressed by:

$$\nabla u = \frac{\partial u}{\partial x} + \frac{\partial v}{\partial y} + \frac{\partial w}{\partial z} = 0 \quad , \quad (2.12)$$

and that the fluid is fully irrotational, thus:

$$\nabla \times u = 0 \quad , \quad (2.13)$$

which conducts us to the potential flow that is described as:

$$\nabla \phi = 0 \quad , \quad (2.14)$$

thus substitute 2.14 into 2.12 entails to the 3D Laplace equation:

$$\Delta \phi = \frac{\partial^2 \phi}{\partial x^2} + \frac{\partial^2 \phi}{\partial y^2} + \frac{\partial^2 \phi}{\partial z^2} = 0 \quad (2.15)$$

2.4.2 Linear stratification

Concerning a linear stratification in environmental fluids like ocean or atmosphere, the density variations according to fluid depth is usually small to what makes these variations neglected, however it's still considerable in view of the buoyancy of fluid. The equation of the harmonic oscillation of a parcel with a displacement η in this linear stratification is written in the derivative form:

$$\frac{d^2 \eta^2}{dt^2} + N^2 \eta = 0 \quad . \quad (2.16)$$

The Boussinesq approximation involved in neglecting these density differences in the equations except when they are multiplied by acceleration gravity g in the buoyancy term which is usually much bigger than the vertical accelerations within the fluid.

The reduced gravitational acceleration $g' = g\rho'/\rho_0 = g(\rho_z - \rho_0)/\rho_0$ is replaced in Navier-Stokes Eq. 2.10 to get the Boussinesq approximation (written below), and the density variation was taken into account only if it is multiplied by gravity g ,

$$\frac{\partial u}{\partial t} + (u \cdot \nabla)u = -\frac{1}{\rho_0} \nabla P + g \frac{\rho'}{\rho_0} + \nu \nabla^2 u \quad (2.17)$$

Linearising 2D Boussinesq equations of motion gives us:

$$\frac{\partial u}{\partial t} = -\frac{\partial P}{\partial x} \quad (2.18)$$

$$\frac{\partial w}{\partial t} = -\frac{\partial P}{\partial z} - g' \quad (2.19)$$

$$\frac{\partial y}{\partial t} = -wN^2 \quad (2.20)$$

$$\frac{\partial u}{\partial x} + \frac{\partial w}{\partial z} = 0 \quad \text{Continuity} \quad \frac{w}{u} = \frac{k_x}{k_z}, \quad (2.21)$$

note that k_x and k_z are the horizontal and vertical wavenumbers and u , v , w are the horizontal and vertical velocity components respectively.

Solving the linear equations above in view of a plane wave solution in two dimensional harmonic motion gives the dispersion relation of the energy propagation by angle θ of vertical fluid parcel displacement in a linear stratification, which is characterized by a constant frequency, as follows:

$$\frac{\omega}{N} = \cos \theta, \quad (2.22)$$

where θ is the tilt of the wavenumber vector \vec{k}_{lee} from the horizontal ($|\vec{k}_{\text{lee}}| = k_{\text{lee}}$). This dispersion relation also defines *lee waves* of a fixed frequency that propagate behind an obstacle emerging at the downstream side of mountain (or seamount) ridges in a stratified fluid [87, 88]. If the system is characterized by a single buoyancy frequency N (linear stratification) and the obstacle is moving at velocity U with respect to the medium then $U = N \cos(\theta)/k_{\text{lee}}$ holds [100]. Thus the maximum achievable k_{lee} becomes $k_{\text{lee}} = N/U$ [101], it is corresponding to fully horizontal wave propagation. [$(N/U)^2$ is referred to as ‘Scorer parameter’ in stationary lee wave theory [87] in which determine whether lee wave is in favorable conditions to be vertically propagating.]

2.4.3 Homogeneous deep and shallow water

If we assume that the wave has a very small amplitude propagating in a homogeneous layer of depth H at frequency ω and characterized by wavenumber k , then the linear dispersion relation is written as:

$$\omega(k) = \sqrt{gk \tanh(Hk)} = \sqrt{gH} \sqrt{\frac{\tanh(Hk)}{Hk}} k \quad (2.23)$$

Then, the general equation of the phase velocity $C = \omega/k$ of a linear surface wave propagation over any depth driven from the potential flow theory can be written as:

$$C = \sqrt{gH} \sqrt{\frac{\tanh(Hk)}{Hk}}, \quad (2.24)$$

and it can be simplified depending on the depth to wavelength ratio.

For deep ocean ($Hk \gg 1$) (where $\tanh(Hk) \approx 1$)

$$C \approx \sqrt{\frac{g}{k}}, \quad (2.25)$$

For shallow water ($Hk \ll 1$) (where $\tanh(Hk) \approx Hk$)

$$C \approx \sqrt{gH} \quad (2.26)$$

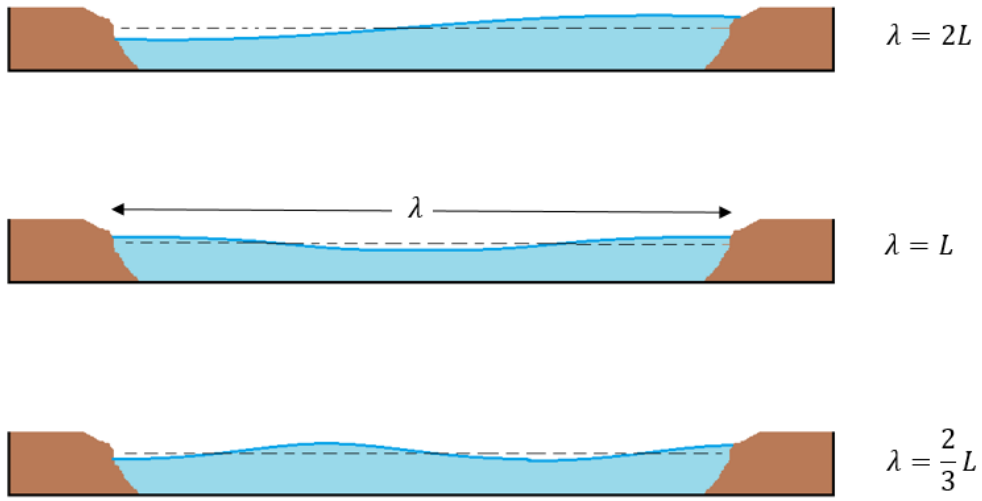


Figure 2.8: **Sketch explains three surface seiche modes $m=0,1,3$.** Note that the seiche mode represents the number of nodes (exhibited in the crossing between the dashed line and water surface).

The surface waves in the deep ocean are dispersive as the wave velocity depends on the wavelength, while in the shallow water the wave velocity is constant for all wavelengths in the same water depth. Standing wave (seiche) is characterized by a large wave length compared to basin depth, for that the velocity expression in Eq. 2.26 is used for calculating the actual lakes seiche period T [102].

$$T = \frac{\lambda}{C} = \frac{\lambda}{\sqrt{gH}}, \quad (2.27)$$

where wavelength λ can be the integer fraction of double basin length $2L$, e.g. $\lambda = 2L/n$. Three seiche modes ($n = 1, 2, 3$) are displayed in Fig. 2.8.

2.4.4 Two-layer approximation

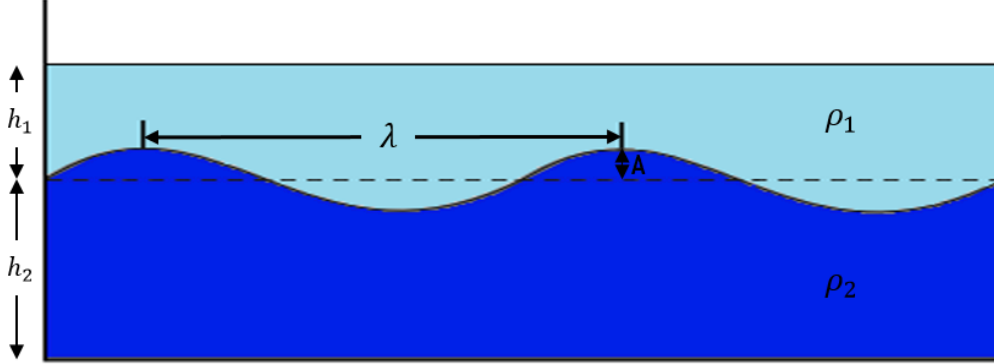


Figure 2.9: **Schema of a two-layer of water.** The denser water ρ_2 with height h_2 in the bottom while a lighter water of density ρ_1 with height h_1 rest on top of it in which $\rho_2 - \rho_1 \ll \rho_0$.

In two-layer stratified water, the internal interface between the two layers of constant densities (see figure 2.9) propagates at a frequency ω and characterized by a relatively infinitesimal amplitude A and the displacement takes the form $\chi(x, t) = A \cos(kx - \omega t)$. A simplified analytical solution can then be derived from the Laplace equation, together with the kinematic and dynamic boundary conditions of the flow at the interface, while assuming a rigid water surface [103].

According to the aforementioned conditions, the equation that describes the wave speed of interfacial internal wave by a given wave number (Ref. [103]) reads as:

$$c^{(2)}(k) = \sqrt{\frac{g}{k} \frac{\rho_2 - \rho_1}{\rho_1 \coth(h_1^{(2)} k) + \rho_2 \coth(h_2^{(2)} k)}} , \quad (2.28)$$

where k denotes the wavenumber (in this case, along the pycnocline), h_1 and h_2 are the thicknesses and ρ_1 and ρ_2 are the densities of the top and bottom fluid layers, respectively, and $\Delta\rho = \rho_2 - \rho_1$ is their difference (see Fig. 2.9). As a dispersive internal waves, the fastest waves is the long-wave ($k \rightarrow 0$) limit the relationship which takes the form of equation $c_0^{(2)}$,

$$c_0^{(2)} = \sqrt{g \frac{\rho_2 - \rho_1}{\rho_1} \frac{h_1 h_2}{h_1 + h_2}} , \quad (2.29)$$

therefore $c^{(2)}(0) \equiv c_0^{(2)}$, note that the index (2) indicates the two layer configuration to the stratified system.

2.4.5 Three-layer dispersion relation

The linear three-layer theory described in [99] has provided a quite accurate description of the observed interfacial velocities and wavenumbers in flow-topography interaction experiments [74]. This approximation assumes rigid top surface, small-amplitude waves, trains with a horizontal wavenumber k one can obtain two-dimensional streamfunctions (that are continuous at the two interfaces) corresponding to k by solving the Taylor–Goldstein equation [104]. The dispersion relation $c^{(3)}(k)$ can be derived numerically from the implicit equation

$$K_2^2 - T_1 T_2 - T_1 T_3 - T_2 T_3 = 0, \quad (2.30)$$

where $K_j = \sqrt{N_j^2 / (c^{(3)})^2 - k^2}$ is the vertical wavenumber in layer j and $T_j = K_j \cot(K_j h_j^{(3)})$, and three layers with depths $h_j^{(3)}$ ($j = 1, 2, 3$) characterized by buoyancy frequencies N_j (see eq. 2.9).

The maximum wave speeds $c_0^{(3)}$ corresponding to the long-wave ($k \rightarrow 0$) limit can be also derived numerically from the above formulae.

2.5 Laboratory wave modeling

Experimental investigations have been conducted in laboratories by a large scientific community to study and understand the complexity of environmental flows for centuries. Experiments play a crucial role in validating theories and enhancing the qualitative and quantitative scientific knowledge. Most importantly, finding fundamental ideas that usually cannot be driven from a complex environment and also the difficulty in solving nonlinear problems of flow phenomena that are usually connected to fluid instability. Vertical stratification is an essential feature in the nature of the environmental phenomena on the globe, which cannot be overlooked when constructing reduced models to simplify the complexity in physical phenomena of environmental flows. Thus establishing two-, three-, multi-layered and linearly stratified water in laboratory tank is the first condition for modeling environmental flows experimentally.

Numerous studies relied on generating internal waves experimentally, through crating stratified system in laboratory tanks. As for the two-layer stratification with extremely sharp interface, water and a freon-kerosene mixture lead to a suitable non-diffusive interface, ideal for interfacial wave studies [105, 106], however it was widely avoided because of safety reasons and environmental considerations. Carbon tetrachloride [107], silicone oil [108] or isoparaffin oil [109] as an upper layer superposed on water (the layer at the bottom), with low difference in viscosity, which creates two-layer system of immiscible

liquids used for investigating the generation of internal waves even though it is consisting higher densities ratio than in the environment. It is more practical in most researches to achieve a wide range of densities ratio with water-salt mixture [42, 110, 111, 112, 113], also density change due to the water temperature deference [114, 115]. These profiles give better understanding on the influence of stratification on various waves generation within large scale environment. Normally, the filling up of the tank to create two- or multi-layer system leads to small a vertical mixing between the layers (i.e. high linear density gradient in the interface).

In the ocean, most cases are composed by an upper layer known by mixing layer (epilimnion), transition layer (metalimnion) that is situated within the interface (thermocline) between the weakly turbulent interior and the strongly turbulent surface mixed layer [116, 117]. Schematic examples in ?? (a) and (b) are the most relevant vertical structures to the oceanic thermocline [118], and an example of the representative equatorial density profiles of the Pacific, Indian, and Atlantic oceans in 2.11 which are showing the typical interface depth in these oceans.

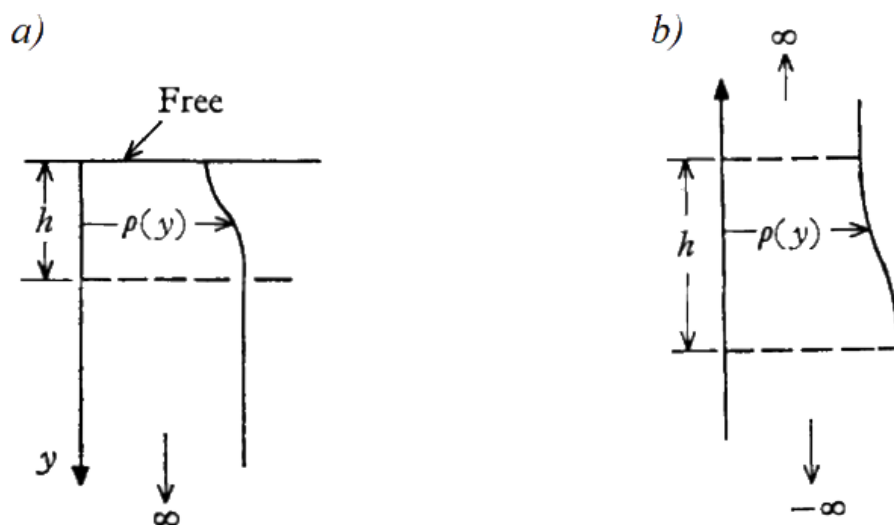


Figure 2.10: Illustration of various heterogeneous-ocean systems in general category under investigation [118].

A two-layer system that is consisting a shallow transition layer (the pycnocline) can be treated as a three-layer system regarding the generation of internal dispersive waves, in which the three-layer approximation describing the relation between interfacial phase speed and the wave number for the sake of correction to the deviation that the two-layer approximation led [74]. While the transition layer was neglected in studying the effect of shear flow in interface displacement when a top layer of fresh water slides with a

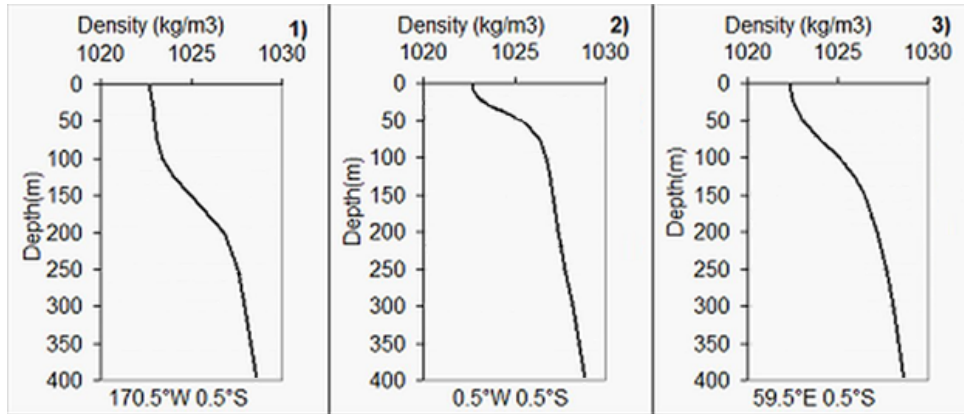


Figure 2.11: **Representative density profiles of equatorial oceans to determine the depth of the interfaces for the Pacific (1), the Atlantic (2) and the Indian (3) Oceans [119].**

slow mean velocity on a stagnant saline layer [37]. The double bucket technique (double-tank method) aides the experimentalist to easily produce more difficult density profiles by varying the initial liquid depths, and it is widely approved in forming a linear stratification [120]; it is relied on the forced-drain and free-drain approaches that is a new version the method of Oster [121] which relies on the forced-drain approach, as the volume flow rates between connecting tanks are controlled by mechanical pumps. Then the density profiles can be identified through the popular methods. The density can be measured by the conventional method rely on conductivity measurements in depth using conductivity probe [122, 123] (usually in multi-layer stratification). Or “Schlieren” method and its enhanced version are appropriate to examine internal waves in linear stratified water by means of their density dependent index of optical refraction [124]. A third way of visualisation is coloring the water layers with dye. unlike the above two methods this is ideal for the case of two to multiple layers of uniform densities.

Selecting the suitable wave-maker to generate internal wave in laboratory tank depends on the stratification, sought-after type of wave, while the wave dimensions (the wavelength) highly depends on the boundary condition of the physical boundaries of the wave maker imposed by the forcing technique [125]. In a narrow tank/channel of a simplified geometry (rectangular) that is tilted once by a small angle (maximum 23° with respect the horizontal), surface and internal seiche are generated propagating in the direction where the whole tank is tilted oscillating back and forth generating first surface and internal seiche mode. If the tank is sealed the interface passes by several stages rapidly from horizontal standing wave (seiche) of first mode and linear model to strongly nonlinear progressive and solitary waves which are all clearly observed [126, 127]. For

continuous excitation of the interfaces, all system can be periodically forced along the longitudinal axis about a central pivot point [61], or indirect method in the way of using a vertical wave maker oscillating with a constant frequency pushing the surface of water [74]. Internal waves could be excited by a moving object along the interface, e.g. Laboratory observations of internal interfacial waves follow the bow of a model ship – dead water phenomenon – towed on the surface of two- or three layer had been examined [81, 128], and lee waves in downstream of artificial seamount at the bottom by either cases pulling that seamount horizontal [129]. Freely propagating interfacial wave also were generated by gravitational collapse dam-break flow from the side of the tank [130, 131, 132]. It is also possible that the recirculation system with a control unit monitors constant flow rates run from two separated sources with different densities for each layer in order to keep an uniform and unchangeable stratified flow, while the wave propagation is forced by a fixed obstacle at the bottom [133].

Chapter 3

Laboratory modeling: methods and setup

3.1 Introduction

Several experiments were conducted in the von Kármán laboratory of environmental flows to study fundamentally two types of waves, standing and propagating waves – at the surface and/or at the interface between water layers in a stratified setting – in laboratory tanks. Specific setups and methods were used for the experimental analysis of a resonance-like wave amplification associated with the so-called dead water phenomenon, and also for studying the damping of surface seiches in a basin characterized by uneven/flat bottom topography. The sections are presented as follows: tanks and of the related equipment, density profiles preparation, the generation of waves, processing of recorded videos for the analysis.

3.2 Experimental wave tanks

Dead-water tank

The experiments #D have been carried out in a narrow rectangular laboratory tank made of transparent acrylic (Plexiglas) of high light transmissivity with thickness $e = 0.6$ cm. The tank is characterized by geometrical dimensions of length $L = 239$ cm and width $w = 8.8$ cm. A schematic sketch of the tank and of the related equipment is presented in Fig. 3.1. The tank was filled up partially to the level $H = 12$ cm composed of saline water (made of well mixed kitchen salt, tap water and red or blue food dye) at the bottom and pure tap water in the top.

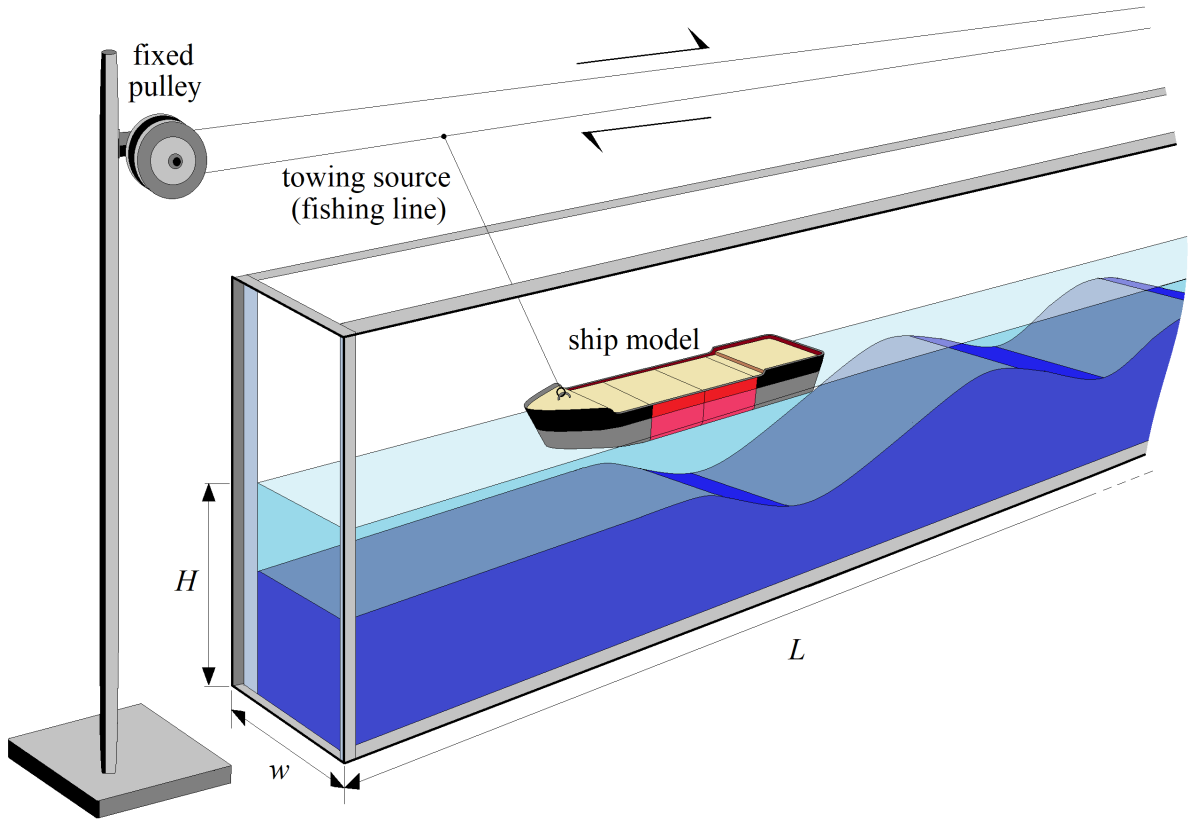


Figure 3.1: **The schematics of the set-up prepared for the Dead-water experiments.** The geometrical parameters of the tank are $L = 239$ cm (total length, not fully shown), $w = 8.8$ cm, and $H = 12$ cm.

We used LEGOTM ‘tug boat’ models (series 4005 and 4025) [134]. These toy ships have a modular design of a bow and a stern building block and four removable identical intermediate segments. Thus five configurations (S_1 to S_5) with different lengths l_s could be investigated, as listed in Table 3.1 and shown in Fig. 3.2. The width of the models was 5.9 cm, comparable to tank width w . The ship model was towed by a (nylon) fishing line

configuration	S_1	S_2	S_3	S_4	S_5
l_s (cm)	9.8	16.2	22.6	29	35.4

Table 3.1: **The lengths of the used ship configurations.**

spanned horizontally above the water surface by ca. 10 cm (as sketched in Fig. 3.1) and driven by a DC motor whose voltage (and hence, the towing speed) could be adjusted between the experiment runs. The ship models’ draught d (i.e. the vertical distance between the surface waterline and the bottom of the hull) was found to be approximately 1 cm in all cases.

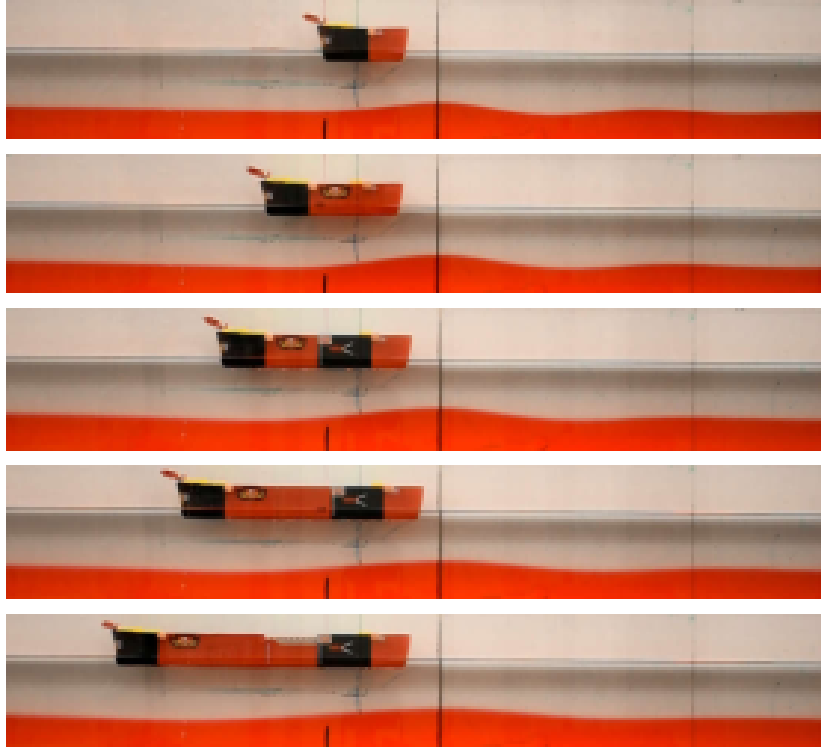


Figure 3.2: **The five different ship configurations of increasing length l_s , marked $S1$ to $S5$ (downward, cf. Table 3.1).** The bottom layer is visualized using red food dye. The snapshots are organized such that the first wave crest locations behind the ship models are underneath each other.

Seiche tank

We conducted experiments $\#S$ in a smaller tank of length $L = 80\text{cm}$ and width $w = 5\text{ cm}$ made of the same material (acrylic or plexiglass) as in the previously mentioned tank. Also the filling process took place in a two phases as mentioned earlier, to ensure the quasi-two-layer character of the stratified water. Blue colored saline water was used for the bottom layer of invariable thickness $h_2 = 4\text{ cm}$ in all experiments, while the upper layer with variable thickness h_1 was freshwater colored by red dye. An upside-down U-shaped small plastic obstacle was placed in the middle of the tank to the bottom; its height h matched the thickness of the bottom (saline) layer $h = h_2\text{ cm}$. A schematic sketch tank and its setup of the tank is shown in Fig. 3.3.

A suspended wave maker consisting of a metallic rod and six rectangular rubber foam 'bumpers' of equal size was placed above the water surface (their length combined is $l_r = 1/2L$ and width $w_r \approx w$, cf. Fig. 3.3). The bumpers could be placed in various configurations along the rod to facilitate the excitation of surface seiche modes.

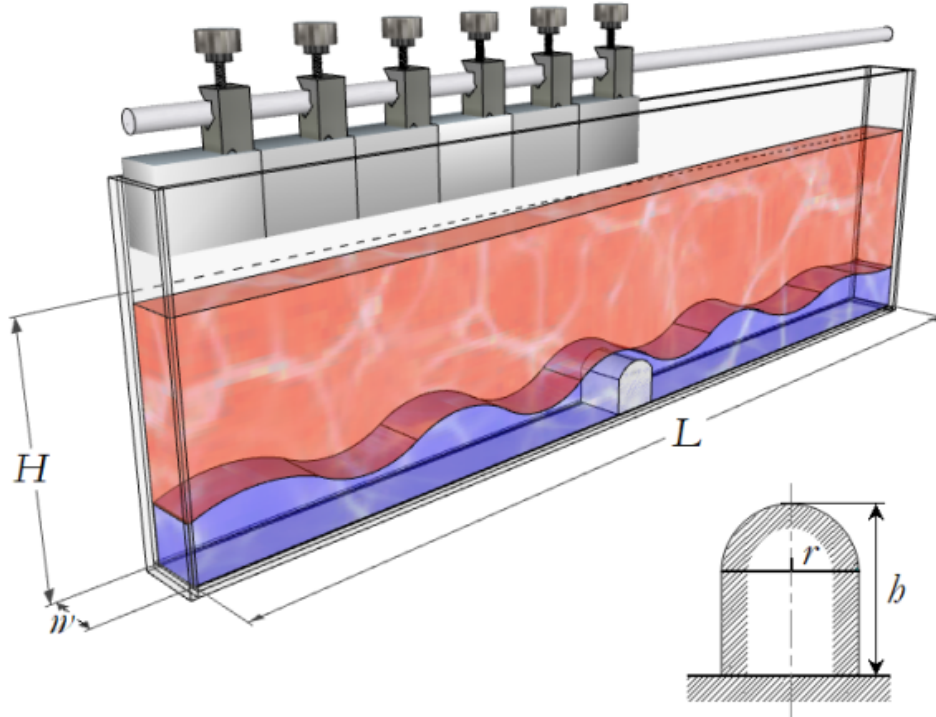


Figure 3.3: **The schematics of the set-up prepared for the seiche experiments.** The geometrical parameters of the tank are $L = 80$ cm, $w = 5$ cm. The shape of the obstacle is sketched in the bottom right corner ($h = h_2 = 4$ cm, $r = 1.75$ cm).

3.3 Density profiles

Density profiles for dead-water experiments

Following the preparation of the stratification, freshwater was poured through a sponge slowly onto the water surface in order to minimize mixing effects and to yield quasi-two layer density profiles, characterized by an approximately 2 cm thick region of steep density increase (see Fig. 3.4) or ‘gradient layer’. The temperature differences within the water body were negligible.

The properties of the 11 different stratification profiles used in the #D series are summarized in Table 3.2. $h_1^{(2)}$ and $h_2^{(2)}$ mark the effective thicknesses of the upper and bottom layers, respectively, using the two-layer approximation (hence the upper index ‘(2)’), i.e. assigning a jump-wise effective density change to the mid-height of the gradient zone. As a characteristic vertical scale in the system a ‘reduced thickness’ H_r can be introduced as the harmonic mean of $h_1^{(2)}$ and $h_2^{(2)}$, i.e. $H_r = (h_1^{(2)}h_2^{(2)})/(h_1^{(2)} + h_2^{(2)})$. Table

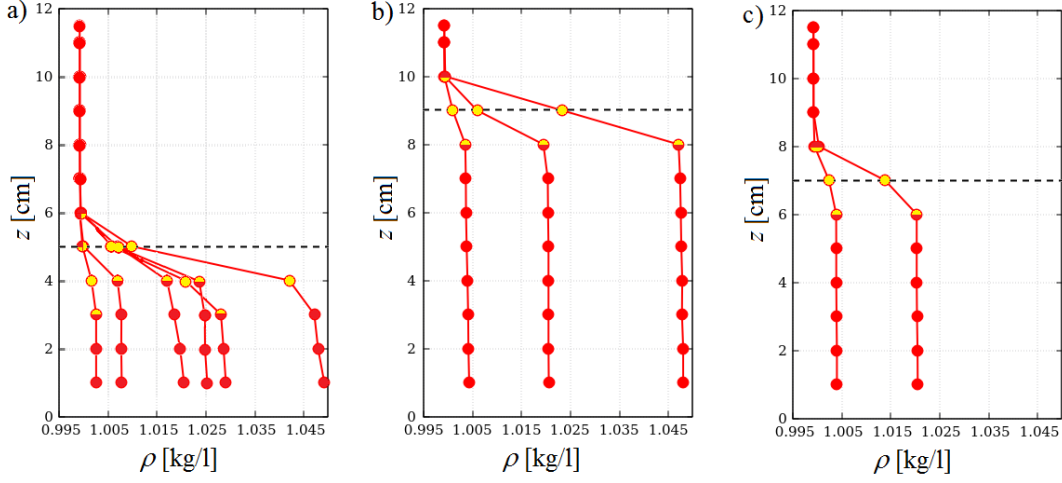


Figure 3.4: **Vertical density profiles of the experiments as measured with a conductivity probe (cf. Table 3.2).** Three configurations of two-layer thicknesses were prepared with various bottom layer densities, as shown in the three panels (the dashed lines mark the theoretical interfaces of the two-layer approximation.) (a) $h_1^{(2)} = 7$ cm, $h_2^{(2)} = 5$ cm; (b) $h_1^{(2)} = 3$ cm, $h_2^{(2)} = 3$ cm; (c) $h_1^{(2)} = 5$ cm, $h_2^{(2)} = 7$ cm. The middle layer thicknesses $h_2^{(3)}$ of the three layer approximations for the same profiles are also indicated by yellow coloring (cf. Table 3.2).

3.2 also lists the values of the average density ρ_2 of the bottom layer and the corresponding two-layer linear interfacial wave velocity $c_0^{(2)}$ in the long-wave limit (see 2.29), while $\rho_1 \approx 1$ kg/l is the average density in the top (freshwater) layer [83].

For a more precise treatment of the density profiles a three-layer approximation can

Experiment series	#1	#2	#3	#4	#5	#6	#7	#8	#9	#10	#11
$h_1^{(2)}$ (cm)	7	7	7	7	7	7	3	3	3	5	5
$h_2^{(2)}$ (cm)	5	5	5	5	5	5	9	9	9	7	7
H_r (cm)	2.9	2.9	2.9	2.9	2.9	2.9	2.25	2.25	2.25	2.9	2.9
ρ_2 (kg/l)	1.019	1.029	1.008	1.003	1.047	1.025	1.004	1.020	1.048	1.004	1.020
$c_0^{(2)}$ (cm/s)	7.30	8.92	4.63	2.71	11.28	8.29	2.92	6.64	10.02	3.35	7.56
$h_1^{(3)}$ (cm)	6	6	6	6	6	6	2	2	2	4	4
$h_2^{(3)}$ (cm)	2	3	3	3	3	2	2	2	2	2	2
$h_3^{(3)}$ (cm)	4	3	3	3	3	4	8	8	8	6	6
N_1 (rad/s)	0.18	0.32	0	0.03	0.16	0.23	0.10	0.27	0.37	0.24	0.55
N_2 (rad/s)	2.95	3.04	1.67	1.05	4.58	3.45	1.45	3.14	4.84	1.47	3.13
N_3 (rad/s)	1.05	0.69	0.15	0.0	1.50	0.73	0.33	0.39	0.36	0.17	0.21
$c_0^{(3)}$ (cm/s)	6.96	8.1	4.4	2.75	12.25	7.95	2.95	6.25	9.55	3.4	7.2

Table 3.2: **Geometrical and physical parameters of the experiments for the two- and three-layer approximations.**

also be applied [99], in which the top, gradient and bottom layers (indexed with $j = 1, 2, 3$, respectively) are characterized by their approximate thicknesses $h_j^{(3)}$ and density gradients, or equivalently, their buoyancy (or, Brunt–Väisälä) frequencies N_j that take the form of the equation 2.9.

The values of $h_j^{(3)}$ and N_j are obtained via piecewise linear regression to a given profile by determining the intersection points and slopes of the fitted lines. In the three-layer theory of Fructus and Grue [99] for ‘piecewise linear’ stratification there is no such an explicit formula for the long wave velocities $c_0^{(3)}$ as in the two-layer approximation 2.29, as will be addressed later. Hence, the $c_0^{(3)}$ -values in Table 3.2 are numerical results.

Density profiles for the seiche damping experiments

To inhibit mixing at the interface (i.e. diapycnal mixing) during the filling-up procedure the same technique was followed, and the sponge was placed right over the obstacle in the the beginning of the filling. The experiments were prepared with the obstacle installed, and so the runs with the obstacle were performed first for each stratification. Then, for another series of runs, the obstacle was removed from the tank (slowly, in the vertical direction, to minimize turbulent mixing) and the dynamics was studied in the absence of the topographic obstacle.

The prepared density profiles of the experiment series $\#S$ are presented in Fig. 3.5, as measured by a conductivity probe. The physical parameters of the two-layer approximation, namely layer thicknesses h_1 and h_2 and the respective densities ρ_1 and ρ_2 were obtained as follows. h_1 and h_2 were measured directly (with a ruler) based on their color (and indeed, the intended thickness $h_2 = h = 4$ cm matching the obstacle height could be achieved within ± 0.25 cm in all cases). The characteristic density ρ_2 of the saline layer was taken as an average of the measured density profile in the $z \leq h_2$ domain, as sketched in the inset of Fig. 3.5. The density profiles were measured before and after experiments when there was no flow in the tank anymore. In all cases, the difference between the two profiles were negligible. The relevant adjustable parameters of the stratification are summarized in Table 3.3 for all nine experiment settings.

Experiment series	#1	#2	#3	#4	#5	#6	#7	#8	#9
h_1 (cm)	11	11	15	15	13	13	13	13	13
ρ_2 (kg/l)	1.0592	1.0076	1.0872	1.0019	1.1114	1.1136	1.1114	1.0437	1.0084

Table 3.3: **Geometrical and physical characteristics of the experiment series.**

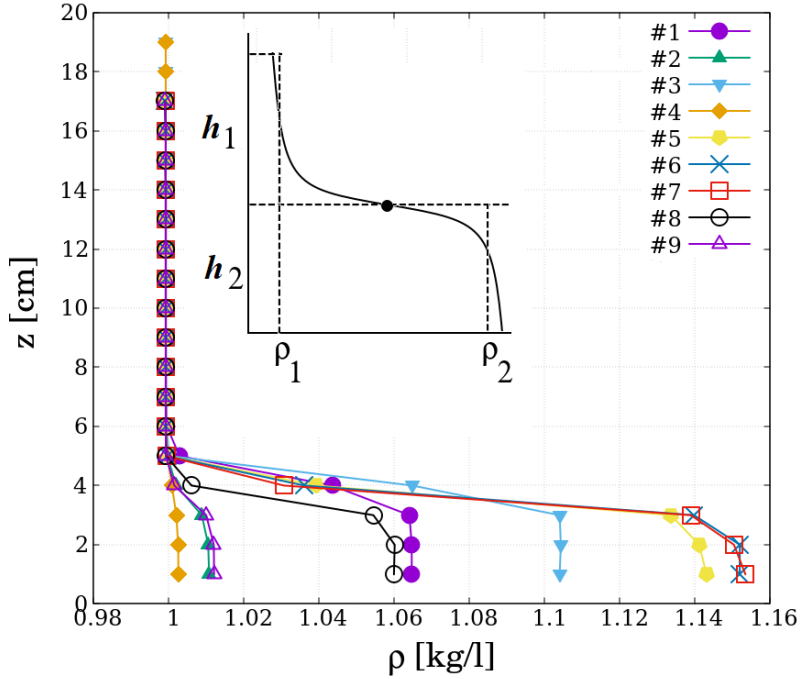


Figure 3.5: **Density ρ as a function of vertical position z from the bottom, for all experiments series (cf. Table 3.3).** The sketch in the inset demonstrates the meaning of the parameters of the two-layer approximation.

3.4 Wave excitation

In the laboratory modeling of dead-water phenomenon (series **#D**), propagating internal gravity waves were generated due to the moving of the ship-toy on the surface of water tank. It is noted that in such a narrow tank the flow is practically two dimensional, therefore we did not (and could not) investigate the three dimensional structure of the wake. The ship model was pulled several times in each experiment letting the water layers to settle down before each run. The ship was pulled at constant velocity in each experiment, which could be adjusted via DC power supply unit.

To generate surface seiche, each experiment (series **#S**) consisted of five runs with and other five without the obstacle. Due to the limited adjustability of the wave maker our analysis was restricted to experiments with dominant surface seiche modes $m = 1, 2, 3, 4,$ and 6 (see fig. 3.6a) – where m denotes the number of nodes of the standing waveform – while the standing wave pattern with a dominant mode of $m = 5$ was found to be very hard to to excite with this device.

In the beginning of each run, the wave maker was pushed down (only once) to the

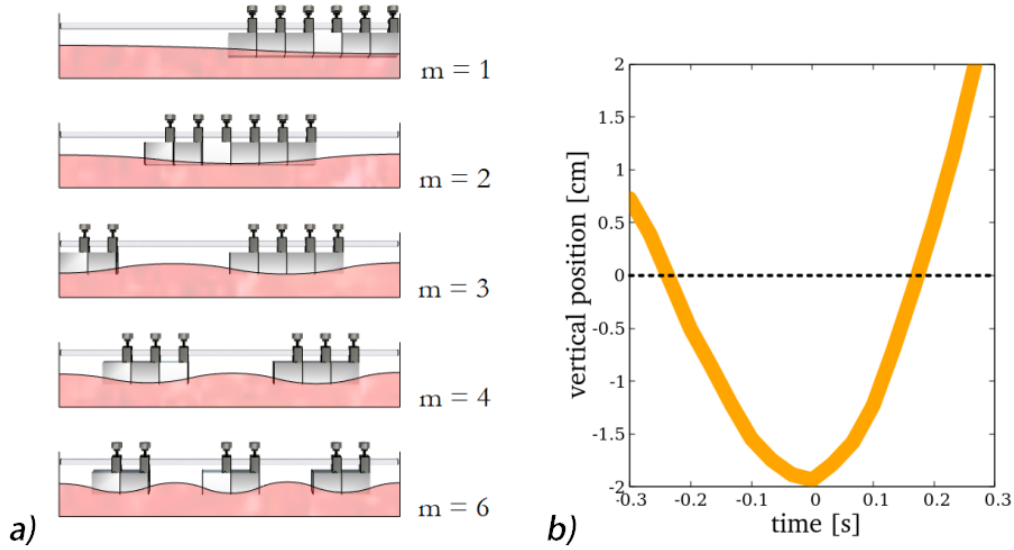


Figure 3.6: (a) The configurations of the six rubber foam bumpers of the wave maker for the excitation of the various surface seiche modes and the sketch of the corresponding waveform. (b) The vertical motion of the bottom of the rubber foam bumpers at the initiation. The position is given with respect to the unperturbed water surface. The width of the line represents the error of reproducibility.

water surface by speed was attempted to match the water restoration speed to induce less perturbed water surface, reaching a maximum depth of 1.65 ± 0.25 cm in a standardized manner and was then instantaneously pulled up, out of the water. Internal seiche and/or internal propagating waves could be generated via surface seiche excitation. The vertical motion of the bumper at initiation is shown in (Fig. 3.6b), as acquired from video tracking. Apparently, the characteristic timescale of the impact, i.e. the duration that the bumper spent below the unperturbed water height (indicated with dashed line) was approximately (0.4 ± 0.06) s, i.e. shorter than the basin-crossing timescale of a surface perturbation.

3.5 Image processing and projection

Experiments were recorded using two HD video cameras (for #D were recorded at frame rate 50 fps resolution of $720\text{px} \times 1280\text{px}$, while #S was at 30 fps, $1080\text{px} \times 1920\text{px}$) pointing perpendicularly to the sidewall close to the middle of the tank, yielding a spatial resolution of ca. 0.5 mm/px in all experiments.

To scale from 2D image plan (pixels) in to the real world dimensions (centimeters), a direct linear transformation was applied to convert spatial variables between these two

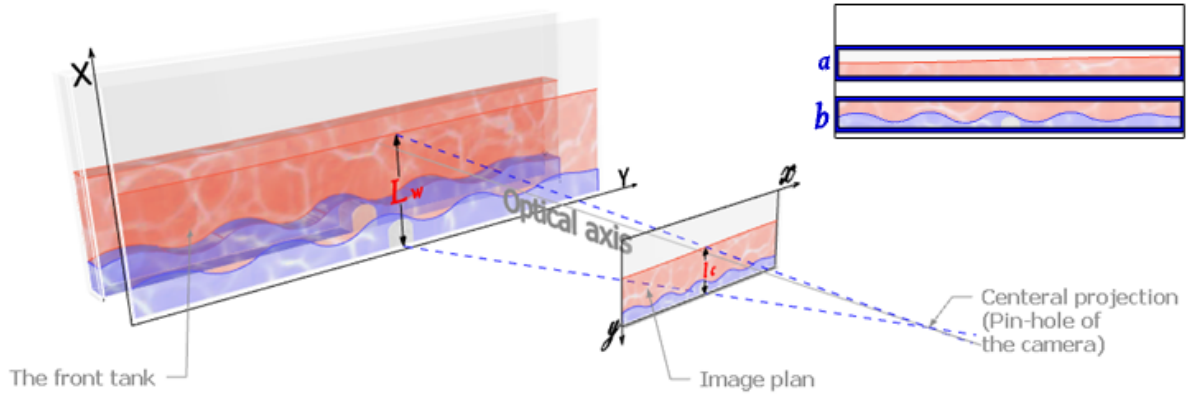


Figure 3.7: **Sketch of linear projection of real-digital coordinates for the experiments.** Example of seiche damping experiment.

different coordinate systems. The tank front represent a plane that is parallel to the projected image on the sensor on the camera, that simplified the calibration and the analysis using no normalization by just ignoring Z – parallel to the optical axis of the camera – dimension, besides the waves in these narrow tanks behave as a plane wave in the way that the physical quantities didn't show change. Two dimensional presentation of the conversion can be a simple matrices system as follow:

$$\begin{pmatrix} X \\ Y \end{pmatrix} = \begin{pmatrix} 0 & f_x \\ f_x & 0 \end{pmatrix} \begin{pmatrix} x \\ y \end{pmatrix}$$

we have $f_x = f_y$, as the image grid characterized by square pixels and the calibration value is taken by any known length in the front-wall of the tank dividing the length (L_w) in the real world by its match from frame pixels (l_c); for example the total height of the water as exhibited in Fig. 3.7.

Clear distinction of the interfaces and sharp difference RGB color intensity could be found in the line between the layers (blue-red and red-white), that was the fundamental tool in processing the recorded videos seeking for qualitative and qualitative analysis. Local area that was processed covers the range of interfaces fluctuations as indicated in boxes a and b in Fig. 3.7, as an example of the case of $\#S$. In the case of $\#D$ the sum of vertical RGB was calculated in order to get a qualitative characteristics of the wave motion (more details in the next Chapter 4).

The open source correlation based feature tracking software Tracker (<https://>

physlets.org/tracker/) was used to acquire the precise value of ship velocity U , and the time series of surface and pycnocline motion.

Chapter 4

Experimental study of the resonant feature of internal gravity waves in the case of 'dead water' phenomenon

4.1 Introduction

The work presented in this chapter focuses on the applicability of linear theories to the dead water phenomenon (aforedescribed in Section 2.3.3). Our aim here is to explore the ship velocity (U) dependence on the wavelength and amplitude of internal waves in the wake and contrast the results with predictions of the linear theory for lee waves and for freely propagating three-layer interfacial waves. These measurements supplement the 'constant force' experiments of Mercier et al. [128] who have conducted state-of-the-art measurements with a prescribed towing force (utilizing a falling weight) to propel a ship model in a rather similar set-up. It is to be emphasized that the difference between the 'constant force' and 'constant velocity' settings may be a crucial issue from the maritime applicability point of view (ships are driven at constant power usually), but is not an essential difference in the framework of the present study.

The main finding to be reported here is that the largest interfacial wave amplitudes emerge when the typical wavelength of the freely propagating interfacial wake waves (whose velocity is set by the speed of the ship model) is equal to the wavelength associated with 'trapped' lee waves (whose frequency is determined by the buoyancy frequency of the density profile) and thus a coalescence of frequencies and wavenumbers develops between these two fundamental co-existing wave motions. Similar resonance-like amplification involving e.g. vorticity waves and internal gravity waves have already been reported in

stratified systems, see e.g. [135]. Yet, to the best of our knowledge, the work described in this chapter was the first to interpret the problem of dead water phenomenon in this framework.

4.2 Results

4.2.1 Qualitative description of the flow

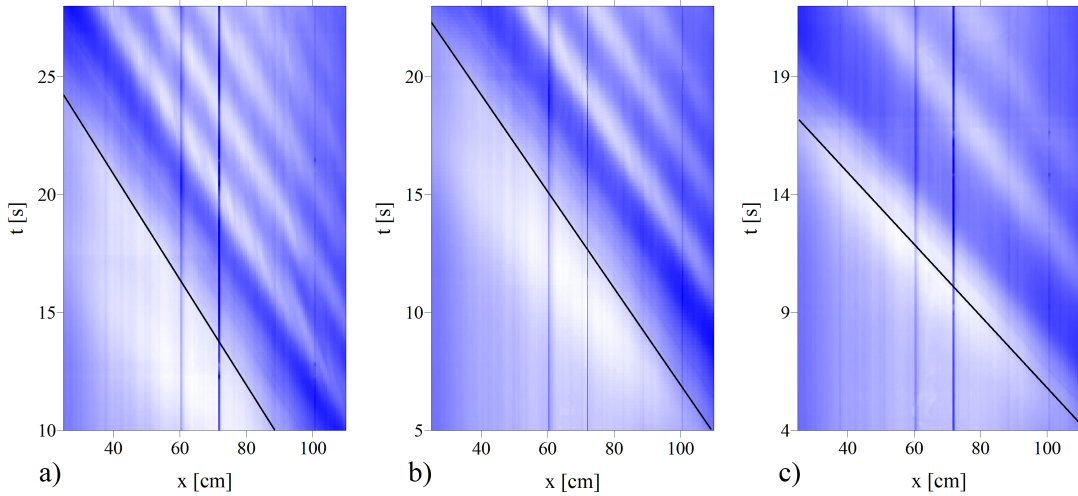


Figure 4.1: **Space-time plots of interfacial wave propagation behind the ship model.** (Stratification profile #11, ship configuration *S2*.) The towing speeds are $U = 4.40$ cm/s (a) $U = 4.82$ cm/s (b) $U = 6.31$ cm/s (c) Horizontal position x and time t are measured from the left edge of the image and from the start of the ship motion, respectively. The coloring in each panel is normalized to the respective minimum and maximum values, thus amplitudes of the different cases cannot be compared to each other. The black lines represent the trajectories of the bow of the ship. The dark vertical lines are position markers on the tank itself, cf. Fig. 3.2.

As a ship model moves along the tank in the studied velocity range $U \in (1.3; 12.2)$ cm/s it generates pronounced waves on the internal interface, while the displacement of the free water surface remains negligible, as visible in Fig. 3.2. An important property of the observed dynamics is that the internal waves are following the ship and propagate at the same velocity as the ship itself. This is visualized in the space-time plots of Fig. 4.1 for three different constant towing speeds U (see caption). In these diagrams the shading of a point at horizontal position x and time t is given by the sum darkness (i.e. number of black pixels in grayscale-converted frames) of the pixel column at x as calculated from the video frame at time t , e.g. the ones shown in in Fig. 3.2. The interface displacement

at each time instant is obtained via subtracting the aforementioned sum darkness from its initial value at rest (obtained before the towing has started) at the given position x . As the background of the tank is stationary throughout the videos, the spatial and temporal changes in darkness are attributed to internal waves. The trajectory of the bow of the ship is highlighted with solid black line in each panel.

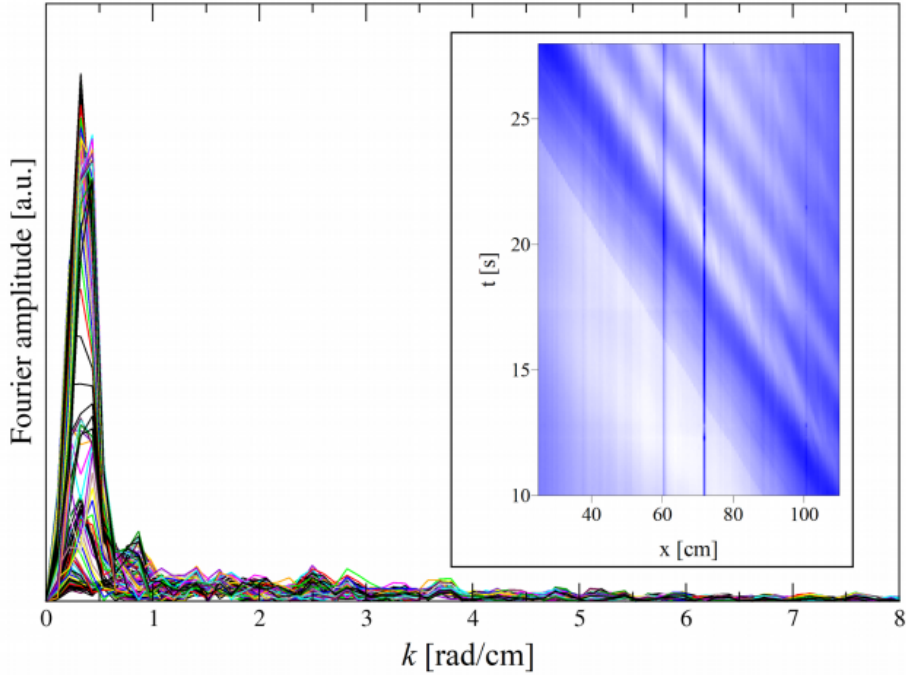


Figure 4.2: **Fourier transforms of internal interfacial displacement at several time-frames corresponding to space-time plot in the sub-figure.** Colors refer to time instants. ship speed $U = 4.82$ cm/s.

As shown in Fig. 4.1, a noticeable train of waves with matching velocity keep a fixed crest-to-crest range also visible in the Fourier spectra represented in Fig. 4.2, corresponding to the experiment whose space-time plot is exhibited in the same figure. The colors of the Fourier spectra refer to different time instants. Apparently, the emerging wave pattern is dominated by a single dominant wave number along the ship uniform movement (check Fig. 4.2). By far, the most dominant peak in this case appears at $k = 0.3$ rad/cm (i.e $\lambda \approx 20$ cm) which agrees with the value used in our analysis and demonstrates that a single wave number can yield an acceptable approximation for the description of the observed patterns.

The typical wavelength ($\lambda = 2\pi/k$) and the characteristic amplitude A of the internal waves are set by the towing speed U , the density profile $\rho(z)$, and the ship's length d . The $A(U)$ dependence is far from monotonous: for each stratification there exists an

intermediate velocity U^* at which internal waves of the largest amplitude develop. This ‘resonant’ amplification is demonstrated with the video frames in Fig. 4.3 for three values of towing velocity U , listed on the panels (stratification #11, ship configuration $S2$). The snapshots are aligned such that the largest displacements of the density interface (marked with black vertical lines) are beneath each other for better comparability. The ship model’s direction of motion is leftward in all images. At the smallest U (uppermost

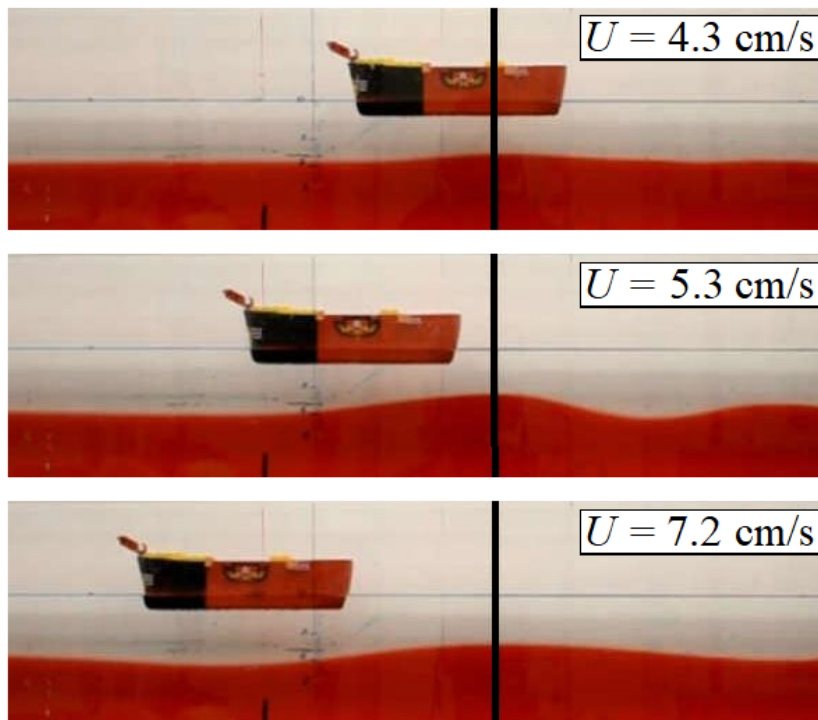


Figure 4.3: **Interfacial wave excitation behind ship model $S2$ for different towing velocities U at stratification profile #11 (cf. Table 3.2).** The snapshots are organized such that the first wave trough locations behind the ship models, marked by black vertical lines, are underneath each other. The wave amplitude is largest at $U^* = 5.3$ cm/s.

panel) a wave crest appears at the interface beneath the ship model. For larger U ’s a train of waves form (cf. Fig. 4.1) and the first crest shifts towards the stern of the ship, while the characteristic horizontal size (peak-to-peak wavelength λ) of the interfacial disturbance increases. Coincidentally, its vertical size (or, amplitude A) also increases and reaches a maximum at U^* , as captured in the second panel of Fig. 4.3. In the $U > U^*$ regime wavelength $\lambda(U)$ continues to increase, but amplitude $A(U)$ starts to decrease, as seen in the two bottom panels in Fig. 4.3. In the following subsection we explore the parameter dependence of U^* and the associated internal wave dynamics.

4.2.2 Parameter dependence of the critical towing speed

The observed maximum vertical interface displacements A (hereafter referred to as amplitudes) against towing speed U are shown in Fig. 4.4a for four exemplary experiment series. The symbols correspond to different stratification profiles (namely #5, #8, #9, and #10, see legend and cf. Table 3.2 and Fig. 3.4). All four series were conducted using ship configuration $S2$ ($d = 16.2$ cm) and were selected for demonstrational purposes. The error bars represent the spatial resolution of the analyzed video records. Apparently, criti-

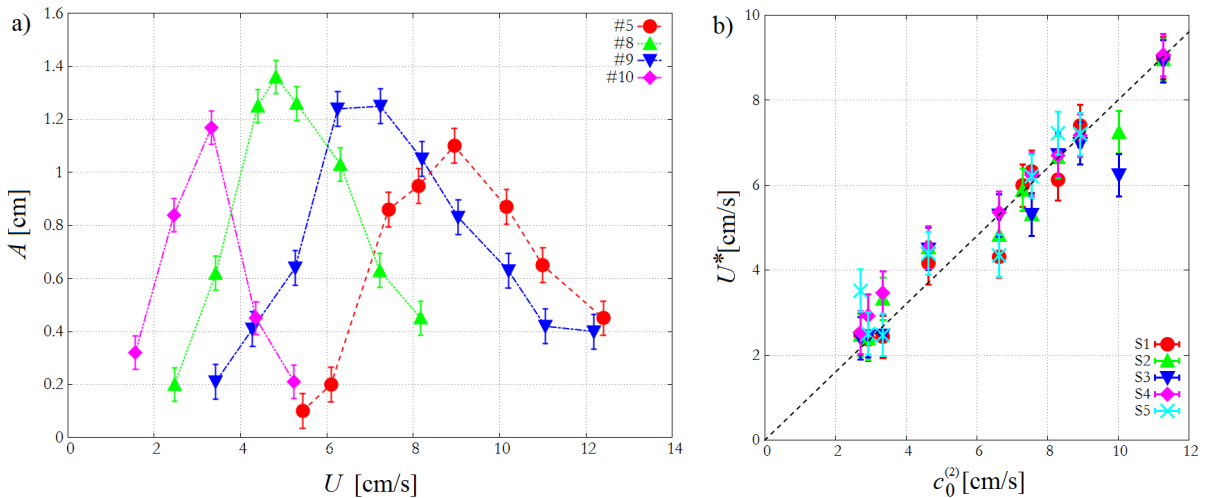


Figure 4.4: (a) Interfacial wave amplitudes A as a function of towing velocity $c_0^{(2)}$ for exemplary stratification profiles #5, #8, #9, and #10 (cf. Table 3.2) obtained with ship configuration $S2$. (b) Critical towing speed U^* as a function of two-layer long wave velocity $c_0^{(2)}$. The different symbols denote different ship configurations (see legend). Error bars represent the sampling of the towing velocities. The dashed line shows the linear fit $U^* = 0.8c_0^{(2)}$.

cal towing speed U^* markedly depends on the properties of density profile $\rho(z)$ with values ranging between 2.1 cm/s and 9.1 cm/s. Based on earlier results [97, 136] the relevant nondimensional velocity scale of the dead water problem is the internal Froude number Fr i.e. the ratio of the ship speed U and the two-layer long wave velocity $c_0^{(2)}$ (described in 2.2.2). U^* indeed scales linearly with $c_0^{(2)}$ as confirmed by the scatter plot of Fig. 4.4b. Here each data point represents the towing velocity maximizing amplitude A in the given series of experiments (the different symbols indicate the various ship configurations used, as indicated in the legend). The dashed line shows the linear fit of $U^* = 0.80(\pm 0.01)c_0^{(2)}$ to all data points.

Certainly, Froude number $Fr \equiv U/c_0^{(2)}$ appears to be an important parameter of the dynamics. However, as will be addressed in what follows, other physical parameters of the

stratification profiles and even ship length l_s affect the occurrence of maximum interfacial wave amplitudes. It is to be noted that due to the incompressibility of water, the flow

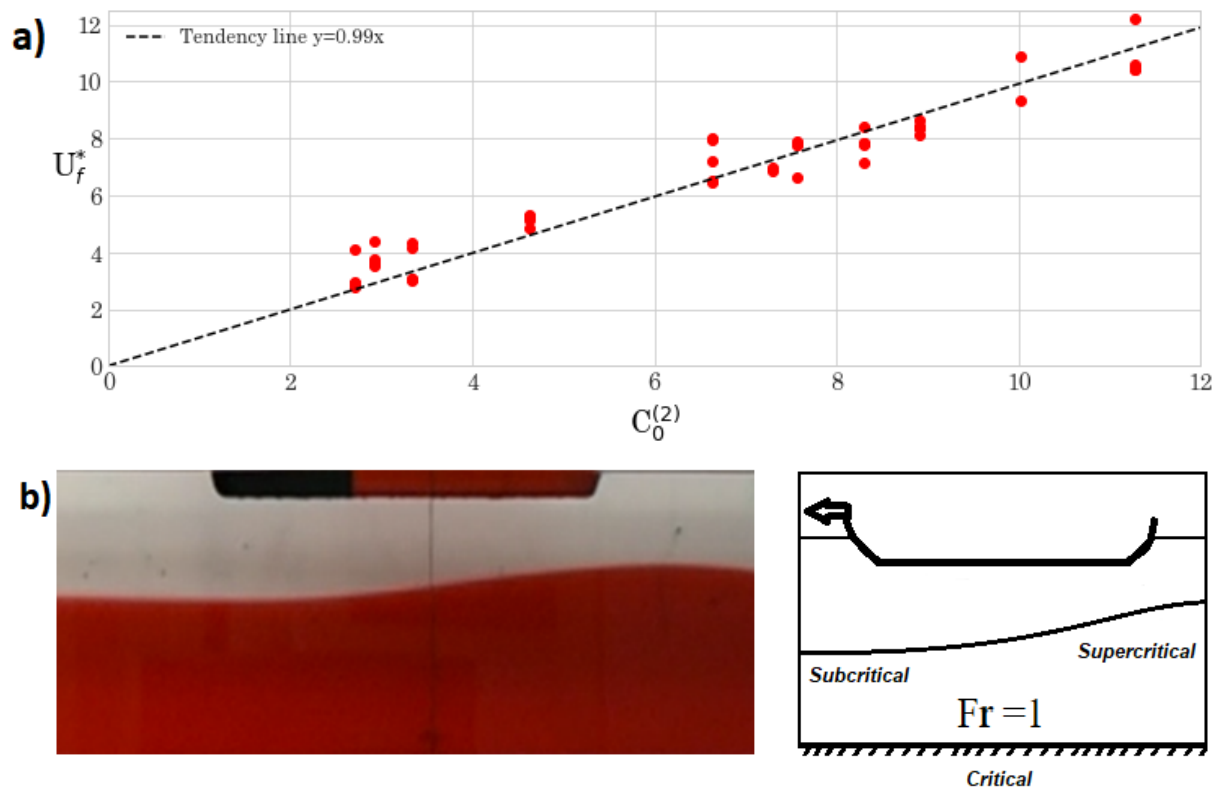


Figure 4.5: (a) Critical flow speed U_f^* under the ship as a function of two-layer long wave velocity $c_0^{(2)}$. The dashed line shows the linear fit $U_f^* = 0.99c_0^{(2)}$. (b) 'right' Snapshot of interfacial displacement in critical flow and its sketch 'left'. From stratified profile #11, and ship velocity $U^* = 5.3$ cm/s

mean speed U_f^* in the upper layer is not precisely equal to the critical towing speed U^* of the ship. From the equation of continuity we get $U_f^* = U^*h_1/(h_1 - d)$, where d is the wet depth of the ship. contrasting this value with the two-layer long-wave velocity $c_0^{(2)}$ yields a fit shown in Fig. 4.5a. The regression line has a slope of 0.99, implying that the maximum actually occurs at the critical speed ($Fr \approx 1$) if calculated with respect to the upper layer mean speed.

This maximum amplification coincides with the occurrence of the flow transition. Three flow regimes can be distinguished in this sense: subcritical $Fr < 1$, supercritical $Fr > 1$ flow in the bow and stern respectively, while the transition is in the halfway as at a critical flow $Fr \approx 1$ holds, meaning that the flow velocity under the bow of the ship is equal to the two-layer long wave speed. The right side of fig. 4.5b is a schematic to explain the transition while the exemplary screenshot in the left side correspond to the

maximum amplitude in the configuration #11.

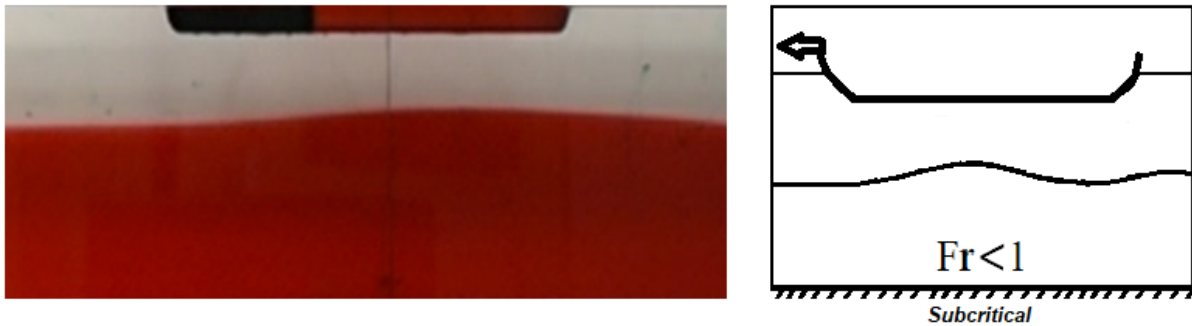


Figure 4.6: 'right': Snapshot of interfacial displacement in subcritical flow and its sketch (left). From stratified profile #11 and ship velocity $U = 4.35$ cm/s.

Low values of Froude number is in a flow characterized by small mean velocity around the ship compared to the internal long wave in two layer stratified system, i.e. subcritical flow in all sections of the fluid, then the interface is slightly curved upward (see Fig. 4.6), while the pressure remains nearly hydrostatic so the flow is restricted horizontally by the ship's bottom and the flow is assumed completely horizontal. Here the wave is excited by the difference in pressure along the interface between the section in the front of the ship and below it (due to the velocity differences). When the displacement of the pycnocline is

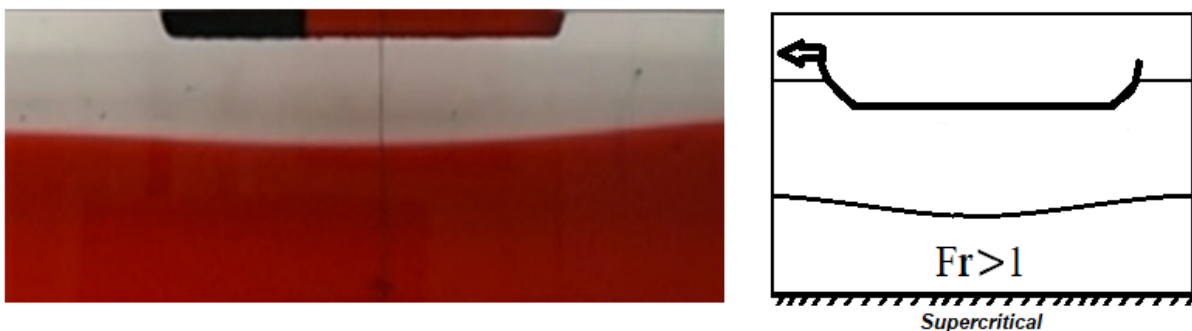


Figure 4.7: Snapshot of interfacial displacement in supercritical flow 'right', and its sketch 'left'. From stratified profile #11, and ship velocity $U = 7.16$ cm/s.

about to reach its maximum (Fig. 4.5b), the peak is pulled to the wake side and becomes completely located in the stern, while there is sufficient vertical kinetic energy beneath the bow that is transferred to potential energy and permit the interface to an imperceptible draw-down, which increases and moves toward the middle of the ship bottom as Froude number increases in all flow sections and the upstream subcritical flow changes to supercritical. Fig. 4.7 is screenshot from experiment #11, ship 2 with speed 7.16 cm/s

characterized by non-dimensional ship speed around 0.95 while the flow Froude number is 1.5. It appears that the pycnocline displacement may be affected by the slope associated with the length of the ship l_s and the wet depth d , e.i. ($d/(2l_s)$). Such geometrical restrictions do not play a role in the subcritical flow where the wave freely propagates under the ship, that even permits the existence of internal wave pockets across the lengthy ships.

4.2.3 Comparison with linear two- and three-layer theories

Here we compare the observed wave (and ship) speeds U and wavenumbers k to the available theoretical predictions of linear two- and three-layer theories. Assuming two homogeneous water layers of different densities separated by a sharp interface, describe the phase velocity described by equation (2.28), and the long-wave ($k \rightarrow 0$) limit the relationship takes the form of equation (2.29), as $c^{(2)}(0) \equiv c_0^{(2)}$ (see Sect. 2.4.4). Expressing the velocities and wavenumbers in the problem's 'natural' nondimensional units, i.e. $U/c_0^{(2)}$ and kH_r (hereafter referred to as k'), respectively, maps equation (2.28) to the same curve for all two-layer density profiles. This graph is shown with blue solid line in Fig. 4.8, alongside the measured data points. The symbol shapes mark different ship configurations (see legend) and the coloring represents nondimensional wave amplitude A' , i.e. the maximum vertical displacement A of the interface divided by the parameter a that measures the maximum of the fitted resonance curve of the given ship configuration. k' was calculated via measuring peak-to-peak wavelengths $\lambda = 2\pi/k$ between the second and third wave troughs. Note, that this method yields a considerable smaller value of λ than the typical length of the first wave trough (cf. Fig. 4.1). Runs where no wave train developed were omitted from this analysis.

The linear two-layer theory systematically overestimates the wave speeds for larger values of k' ; as the wavelength becomes comparable to the thickness of the pycnocline, the two-layer approximation – assuming step function-like density profiles – is not sufficient anymore. Interestingly, however, the best agreement between the data and the theory (in the $k' \approx 0.5$ domain) is observed at near-resonant wave speeds, i.e. where wave amplitudes A' are large (see Fig. 4.8).

When the scaled towing speeds $U/c_0^{(2)}$ are larger than 0.8, the observed wavenumbers remain larger than the predictions of the two-layer theory and exhibit a roughly inversely proportional scaling $U/c_0^{(2)} \propto k'^{-1}$ (see the gray hyperbolic guide curves in Fig. 4.8) the implications of which will be discussed in subsection 4.2.4.

For the proper treat of the aforementioned 'non-step function-like' property of the density profiles, our analysis rely on the dispersion relation 2.30 which is driven from

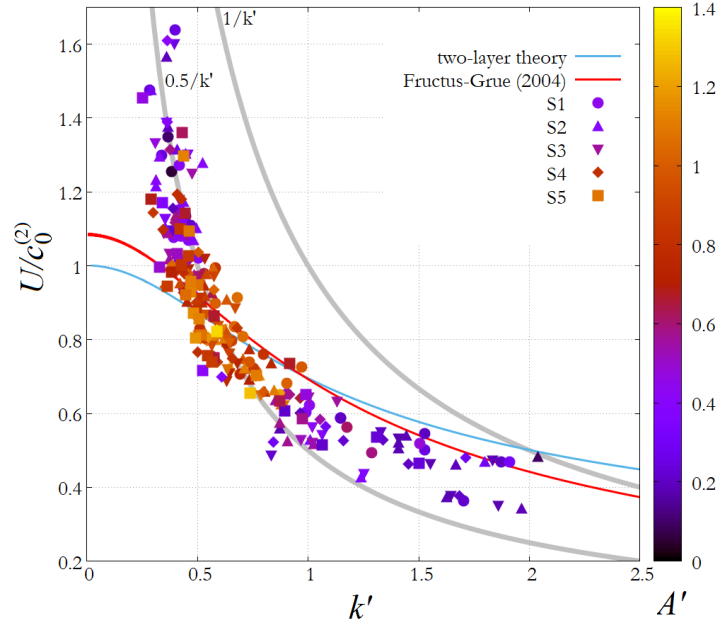


Figure 4.8: (a) **Nondimensional towing (wave) speeds $U/c_0^{(2)}$ as a function of nondimensional wavenumber $k' = kH_r$.** The symbol shapes mark different ship configurations (see legend), and the color scale marks non-dimensional amplitude A' , rescaled by the (polynomial-) fitted maximum values of the corresponding resonance curves (cf. Fig. 4.4). The blue curve represents the invariant (with respect to the nondimensional units used here) two dimensional velocity-wavenumber relation (2.28), the red curve denotes an exemplary three-layer relation, obtained for the parameters of experiment #5, based on the implicit formula (2.30) of Fructus and Grue (2004). The grey curves represent two hyperbolae, i.e. ‘iso-frequency curves’ in the corresponding nondimensional time units, $y = 0.5/x$ and $y = 1/x$, respectively.

linear theory and describe the wave number and phase velocity of wave evolves in the three layers stratified water characterized by linear Brunt-Väisälä frequency N_j in each layer (The numerical model already detailed in subsection 2.4.5)

To demonstrate the difference between the predictions of the two- and three-layer theories, the rescaled $c^{(3)}(k)$ curve calculated with the parameters of stratification profile #5 (see Table 3.2) is added to Fig. 4.8 in the form of a red curve. Note, that unlike the aforementioned two-layer curve (blue) the three-layer one is not invariant at all in the units used here. For instance, in this exemplary case $c_0^{(3)} > c_0^{(2)}$ holds, but for many other profiles the sign would be reversed (cf. Table 3.2). Therefore, the red curve in Fig. 4.8 should not be compared with all the data points in the plot, (only to those that are obtained for stratification profile #5, not highlighted in the figure).

Instead, for a meaningful presentation of the two models’ performance we plot the theoretical phase velocities of the two- and three- layer models against the measured wave

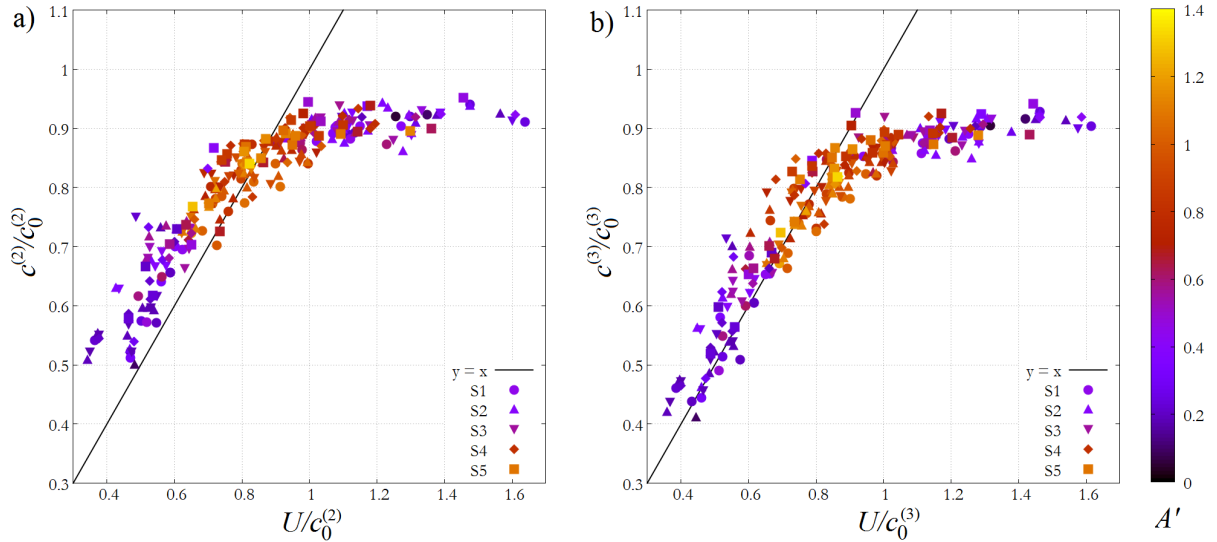


Figure 4.9: **Two-layer (a) and three-layer (b) theoretical velocities as a function of the measured towing (and wave-) speed U .** The symbol shapes mark different ship configurations (see legend), and the color scale marks non-dimensional amplitude A' , rescaled by the (polynomial-) fitted maximum values of the corresponding resonance curves (cf. Fig. 4.4). The values on both the horizontal and vertical axes are rescaled with respect to the long wave limit velocities of the respective approximation (two layer for panel a, three-layer for panel b). The black solid curves represent the $y = x$ line.

speeds U for each observed wavenumber k in the correlation diagrams of Fig. 4.9a and b, respectively. In both panels the theoretical long wave velocity ($c_0^{(3)}$ or $c_0^{(2)}$) was used as the unit for nondimensionalization. Symbol shapes denote different ship configurations and the coloring represents rescaled amplitude A' as in Fig. 4.8. It is to be remarked that with the particular density profiles applied here, where $N_2 \gg N_1, N_3$ holds, a further simplification of the model would be possible by setting $N_1 = N_3 = 0$. We found that in this case the numerical results of $c^{(3)}(k)$ remain the same within $\pm 5\%$.

As noted before, the two-layer theory systematically overestimates the speeds in the $U/c_0^{(2)} \lesssim 0.8$ range (i.e. when $U \lesssim U^*$), thus the vast majority of the data points scatter above the $y = x$ line (black) in panel a. The three-layer theory, however, yields a fairly good match with the observations in the same subcritical regime. In the supercritical range, however, both two- and three-layer approximations break down entirely, as indicated by the deviation of the data points from the $y = x$ line, implying that here another physical mechanism becomes relevant in the wavenumber selection.

4.2.4 Lee-wave dynamics

A hyperbola in a velocity-wavenumber ($c(k)$) dispersion plot marks a constant frequency ω (since $c = \omega/k$). For the nondimensional parameters of Fig. 4.8 the hyperbolic guide curves represent identical frequencies with respect to the stratification-dependent time unit $\sqrt{H_r \rho_1 / (g(\rho_2 - \rho_1))}$. Thus, the fact that the data points appear to follow hyperbolic scaling when $U > U^*$ implies that a characteristic frequency associated with the given density stratification $\rho(z)$ determines the observed wavenumbers.

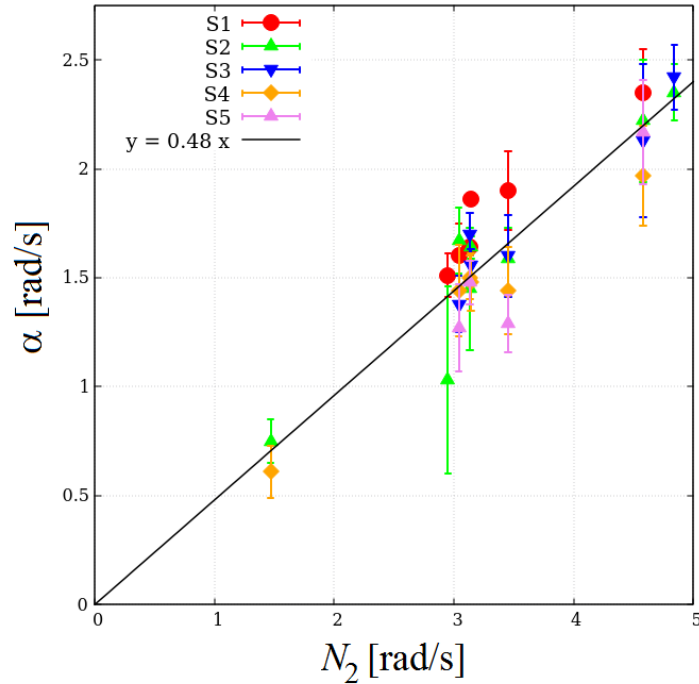


Figure 4.10: **Correlation plot between the intermediate layer buoyancy frequency N_2 and fitting parameter α , obtained by regression to the $U(k)$ plots in the $U > U^*$ velocity range.** The different symbols and colors represent different ship configurations (see legend). The error bars denote the fit errors (standard deviations) of α . The slope of the black linear function is 0.48.

Such physically meaningful ‘eigenfrequencies’ are the buoyancy frequencies N_j of the layers (see Table 3.2), among which the mid-layer value N_2 is the largest in all cases. Fitting the function α/k to the dimensional $U(k)$ data in the $U > U^*$ (supercritical) range yields the empirical frequency parameter α that is plotted against N_2 in Fig. 4.10. The error bars represent the regression errors, and the different symbols mark various ship configurations. The scattering of the data points indicate a linear relationship $\alpha = 0.48(\pm 0.01)N_2$. The result of the fit is shown with a black solid line.

As mentioned previously at the last paragraph of section 2.4, *lee wave* is a phenomenon that may propagate in a constant frequency when the system is stable and continuously stratified. Its linearized dispersion relation can be described as $U = N \cos(\theta)/k_{\text{lee}}$ in a system featured by flow velocity U and buoyancy frequency N . Here θ is the angle at which the wave propagate with respect to the horizontal axis [137]. Thus the wave is able to propagate vertically as well resulting upward energy flux in the form of trapped internal waves in the lee side of the topography.

Buoyancy frequencies N_1 and N_3 of the top and bottom layers are small in the studied density profiles, thus any lee wave activity is expected to be confined to the roughly 2 cm-thick intermediate layer which would then act as a ‘waveguide’ [74] for the observed oscillation frequencies (i.e. above N_1 and N_3) at the interface. Since the layer thickness is an order of magnitude smaller than the typical wavelengths in the $U > U^*$ regime, \vec{k}_{lee} is nearly horizontal here ($\phi \approx 0$).

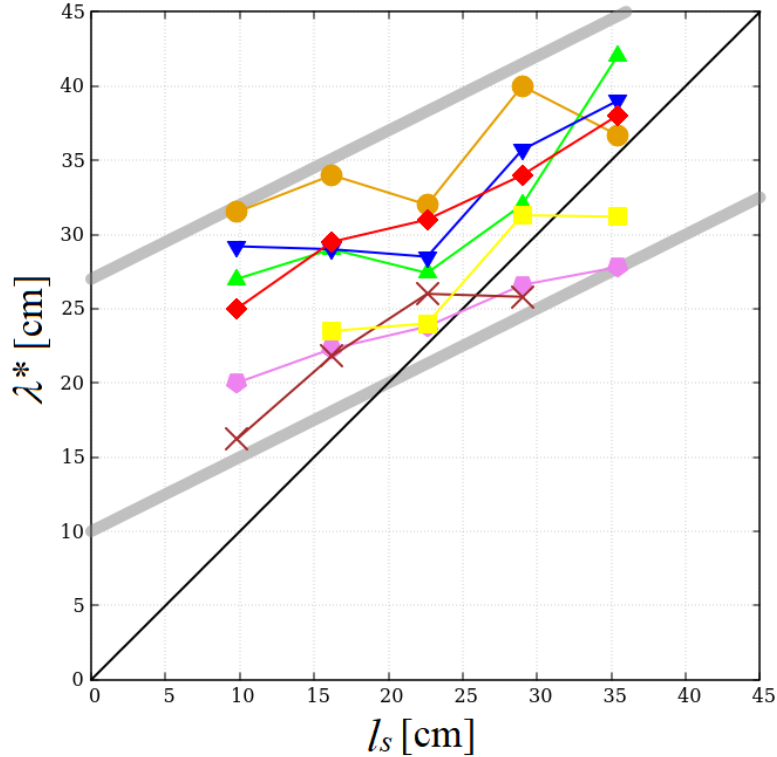


Figure 4.11: **Critical wavelength λ^* (corresponding to the maximum amplitude) as a function of ship length l_s .** The different symbol mark different stratifications. The slopes of the black and grey linear guidelines are 1 and 0.5, respectively.

The linear scaling presented in Fig. 4.10 appears to be consistent with the proposition that it is indeed lee wave-like dynamics that is observed in the supercritical regime, but

– due to the peculiarities of the stratification profile – not in its ‘classical’ form. As an empirical correction we may therefore introduce an effective buoyancy frequency $N_{\text{eff}} \approx 0.48N_2$ to characterize the stratification, whose possible physical interpretation will be addressed in the Discussion.

Finally, we investigated the critical wavelength $\lambda^*(\equiv 2\pi/k^*)$ corresponding to the maximum amplitude as a function of ship length l_s . The results are shown in Fig. 4.11 for seven different stratification profiles, marked by different colors and symbols. The solid black line marks $y = x$ and the gray guides are linear functions with a slope of 0.5 and a vertical offsets 10 cm and 27 cm. Apparently, the critical wavelength tends to increase with ship length, that roughly follows the empirical formula $\lambda^* \approx 0.5l_s + f(\rho(z))$, implying that the ship configuration also plays a role in the wavenumber selection.

4.3 Discussion

Inspired by the historical work of Ekman analyzing the ‘dead water’ phenomenon [81] we have conducted laboratory experiments on wave excitation by a ship model towed at a fixed speed over a salinity stratified water body. We have analyzed the dependence of the interfacial wavenumber k and amplitude A on the towing speed U , the stratification profile $\rho(z)$ and ship length l_s .

Due to the fact that in this setting the observed amplitudes are comparable to the characteristic vertical length scale H_r of the problem, the excited waveforms can only be explained, if at all, by means of nonlinear wave theories (see, e.g. [91][94]). Yet, we deliberately focused our analysis on linear approximations in order to explore to what extent can these account for the basics of the observed dynamics, most notably the resonance-like amplitude amplification around $U/c_0^{(2)} = 0.8$ and the associated transition in terms of the $U(k)$ dependence.

From the findings reported in the previous section it appears that the observable characteristic wavenumber k at a given U is set by the larger one of the corresponding 3-layer wavenumber $k^{(3)}(U)$ predicted by the linear approximation of Fructus and Grue [99] and the lee wavenumber $k_{\text{lee}}(U)$ derived using ‘effective buoyancy frequency’ $N_{\text{eff}} \approx 0.48N_2$. In other words, among the two competing mechanisms the one yielding shorter waves generates the first trough behind the ship model and, hence, sets the characteristic wavelength in the system. The crossing point of the two dispersion relations where $k_{\text{lee}} = k^{(3)}$ holds is encountered around the critical towing speed U^* , as sketched in Fig. 4.12. At this resonant wavenumber the two wave types would be superimposed onto each other resulting in an amplified interfacial wave excitation, that is confirmed by the observations.

As a secondary effect, the selection of the resonant wavelength λ^* was also found to be influenced by the length l_s of the ship, as shown in Fig. 4.11.

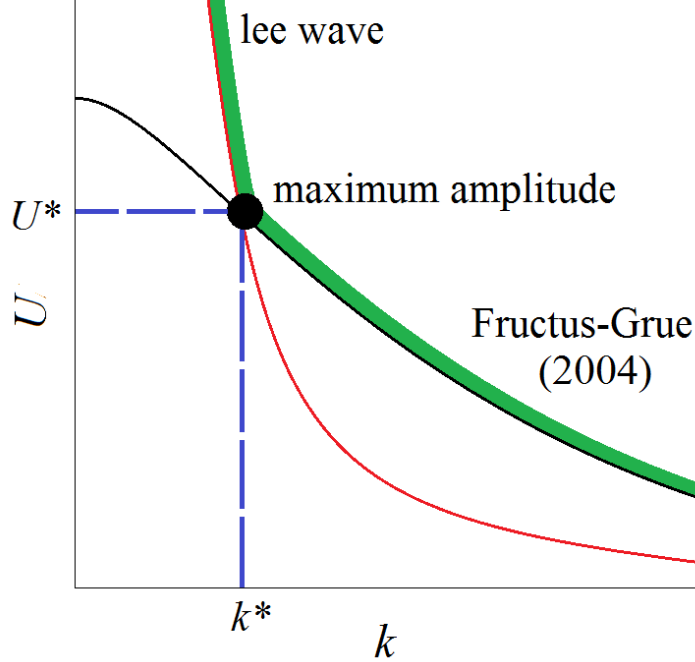


Figure 4.12: **The schematic wavenumber velocity diagrams of the lee waves (red curve), the 3-layer model of Fructus and Grue [99] (black), and the actually observable $U(k)$ domain (green) set by the maximum of the two competing $U(k)$ functions at each k . The intersection point $U^*(k^*)$ (black filled circle) fairly corresponds to maximum amplitude internal wave excitation.**

The reason for the occurrence of the aforementioned factor of 0.48 in the effective buoyancy frequency N_{eff} is unclear. Comparing this value to the internal wave dispersion relation $\omega = N_2 \cos(\phi)$ within the intermediate layer we find that it would imply a wave propagation whose lines of constant phase lie at an angle $\phi \approx 61^\circ$ to the vertical. However, we were not able to identify any geometrical constraint (e.g. one associated with the depression at the interface behind the ship) that would necessitate the presence of such a limiting angle.

On the other hand, taking the total bottom-to-surface density difference $\Delta\rho$ and assuming linear stratification along the full depth H gives a certain ‘mean buoyancy frequency’ $N_m = \sqrt{g/\rho_1 (\Delta\rho/H)}$ which is found to follow the average scaling $N_m \approx 0.46(\pm 0.04)N_2$ for the profiles listed in Table 3.2, that is fairly close to N_{eff} . Thus, the explanation may be that for long waves whose wavelength λ exceeds H , the otherwise complex three-layer profile can be simply ‘averaged over’ in terms of density gradients.

It is to be noted that the co-existence of boundary-trapped lee waves and internal waves (behind a step-shaped obstacle) has been investigated experimentally in [138]: there, however, the two wave types were propagating in a rather different manner, as the internal wave modes could freely enter the top domain of the tank due to the continuous linear stratification applied. (In the present case, these wave modes are also restricted to the vicinity of the pycnocline.)

Our results clearly demonstrate the somewhat surprising and unexpected message that linear theories can occasionally be applied for the description of interfacial waves in such velocity and amplitude ranges that otherwise belong to the domain of nonlinear wave dynamics. It is clear, however, that linear models are insufficient to describe more complex features of the observed phenomena, e.g. waveforms, vorticity, etc. We also hope to increase awareness in the community about the dead water phenomenon, which – despite being discovered over a century ago – is still an interesting ground for theoretical, numerical, and experimental research.

Chapter 5

Laboratory experiments on the influence of stratification and a bottom sill on seiche damping

5.1 Introduction

Here we report on laboratory experiments in a narrow water tank, filled up with quasi two-layer salinity stratified water, with a vertical obstacle installed in the middle of the domain in the bottom layer (as described in Chapter 3). We analyze the damping of various surface wave modes causing the generation of internal wave modes that develop after pulse-like initial seiche excitation at the water surface. To the best of our knowledge, these are the first experiments in the literature on surface seiche damping in the presence of a bottom sill yielding considerable baroclinic wave drag. The sections in this chapter are presented as follow; Qualitative description of the flow, analysis on surface and internal waves time series, decaying source-filter dynamics, topographic energy conversion in our laboratory tank and Gullmar fjord.

5.2 Results

5.2.1 Qualitative description

The flow dynamics in the set-up is driven by the decaying surface waves initiated by the aforementioned standardized instantaneous push of the wave maker in Subsection 3.6. In the qualitative sense, the decay of the resulting surface standing waves is not affected

by the presence or absence of the bottom obstacle (although the actual values of the decay rates are substantially different in the two configurations as will be discussed later). However, the dynamics at the pycnocline can be vastly different in the two cases. If the obstacle is installed, velocity shear can develop between the bottom and top layers that yields the excitation of baroclinic (internal) wave modes along the pycnocline [74]. In the control runs – i.e. without obstacle – the vertical displacement of the surface and the pycnocline are found to be co-aligned at each time instant, as if in a homogeneous fluid (barotropic wave modes).

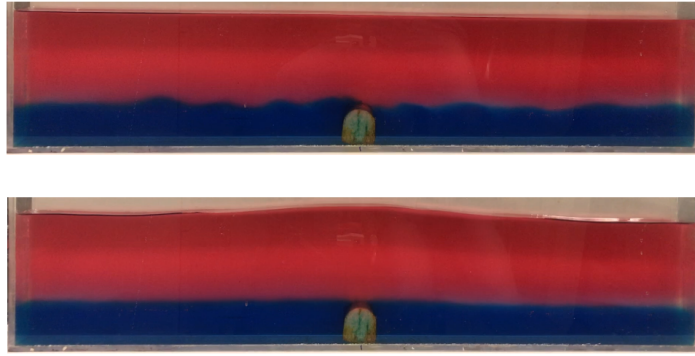


Figure 5.1: **(a) Snapshots from experiments with $m = 1$ (top) and $m = 2$ (bottom) surface seiche modes (configuration #3, cf. Table 3.3).**

Yet, even if the obstacle is present, large amplitude internal waves do not necessarily get excited, as demonstrated in Figs. 5.1 and 5.2. Fig. 5.1 shows snapshots from two experiments, characterized by the leading mode of the surface seiche that is $m = 1$ (base mode) and $m = 2$ in the top and bottom images, respectively. One can notice that in the former case, where a node of the surface wave form is located at the center of the tank, indicating purely horizontal flow right above the obstacle, slowly propagating internal waves of short wavelength appear “radiating away” from the obstacle with fairly large amplitudes. In the latter experiment, however, where the surface displacement has an antinode – and hence vertical oscillation of the fluid parcels – at the obstacle location, no progressive internal waves are visible.

The corresponding space-time plots showing the displacement of the surface $\eta(x, t)$ and of the pycnocline $\chi(x, t)$ with respect to their initial levels are presented in Figs. 5.2a and 4b, respectively, as obtained via video analysis. The dashed vertical lines in Fig. 5.2a represent the locations of the nodes of the dominant mode ($m = 1$ in the left and $m = 2$ in the right panels). After the initiation of the surface seiche at $t = 0$, propagating baroclinic waves dominate the picture in the $m = 1$ run (Fig. 4b left); later the waves get reflected

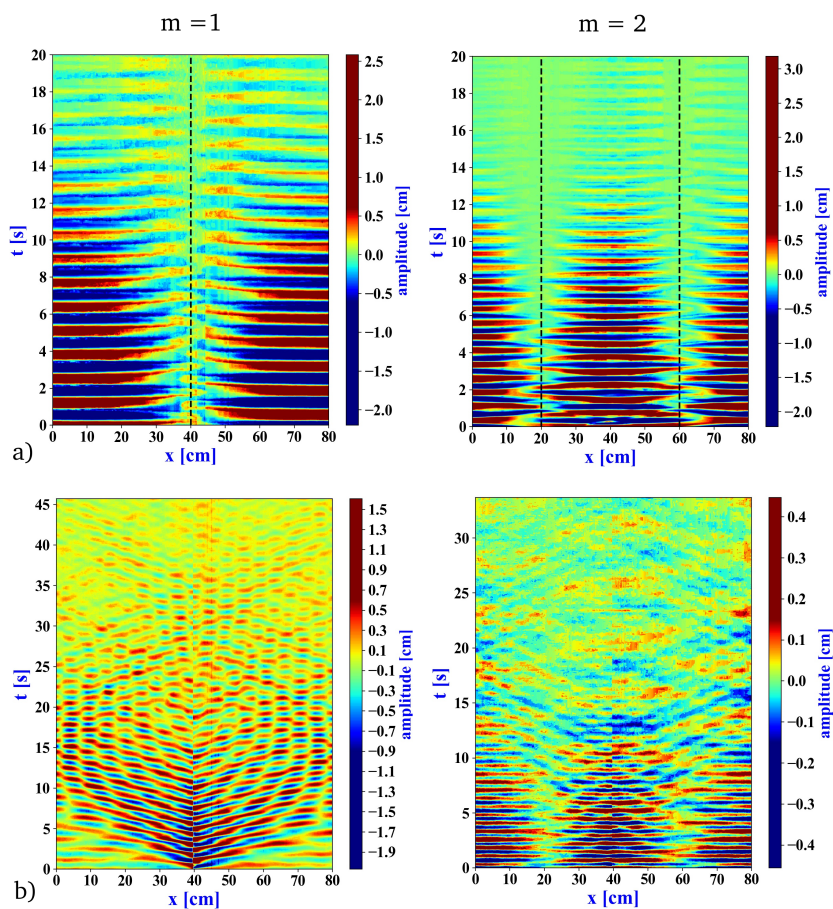


Figure 5.2: Space-time plots of the two experiments of Fig. 5.1, showing the vertical displacement of the surface $\eta(x,t)$ (a) and the pycnocline $\chi(x,t)$ (b) in the whole tank for dominant surface wave modes $m = 1$ (left) and $m = 2$ (right). Obstacle location is at $x = 40$ cm. Vertical dashed lines in the top panels denote the expected locations of nodes.

at the sidewall and thus evolve into internal standing wave-like interference patterns. In the $m = 2$ case, the large-scale decaying barotropic oscillation characterizes the entire domain with hardly any noticeable slowly propagating structures (Fig. 4b right). This duality of internal wave excitation is apparent throughout the higher seiche modes as well: antisymmetric surface wave forms associated with odd values of m (see Fig. 3.6a) tend to excite larger baroclinic wave activity via the obstacle placed in the geometrical center than the symmetric waves (even values of m).

5.2.2 Surface waves

Vertical displacement time series of the water surface $\eta(x, t)$ and the pycnocline $\chi(x, t)$ were logged at the vicinity of the sidewall (i.e. at $x \approx 0$ or L) in each experiment to ensure that all standing wave modes have antinode at the measurement location. Note, that due to the boundary conditions only here it is guaranteed that all standing wave components exhibit maximum amplitude. Examples of such records are shown in the panels of Fig. 5.3a and b for the η and χ signals (red and blue curves, respectively) from runs with dominant modes $m = 1, 2$, and 4 (from the left).

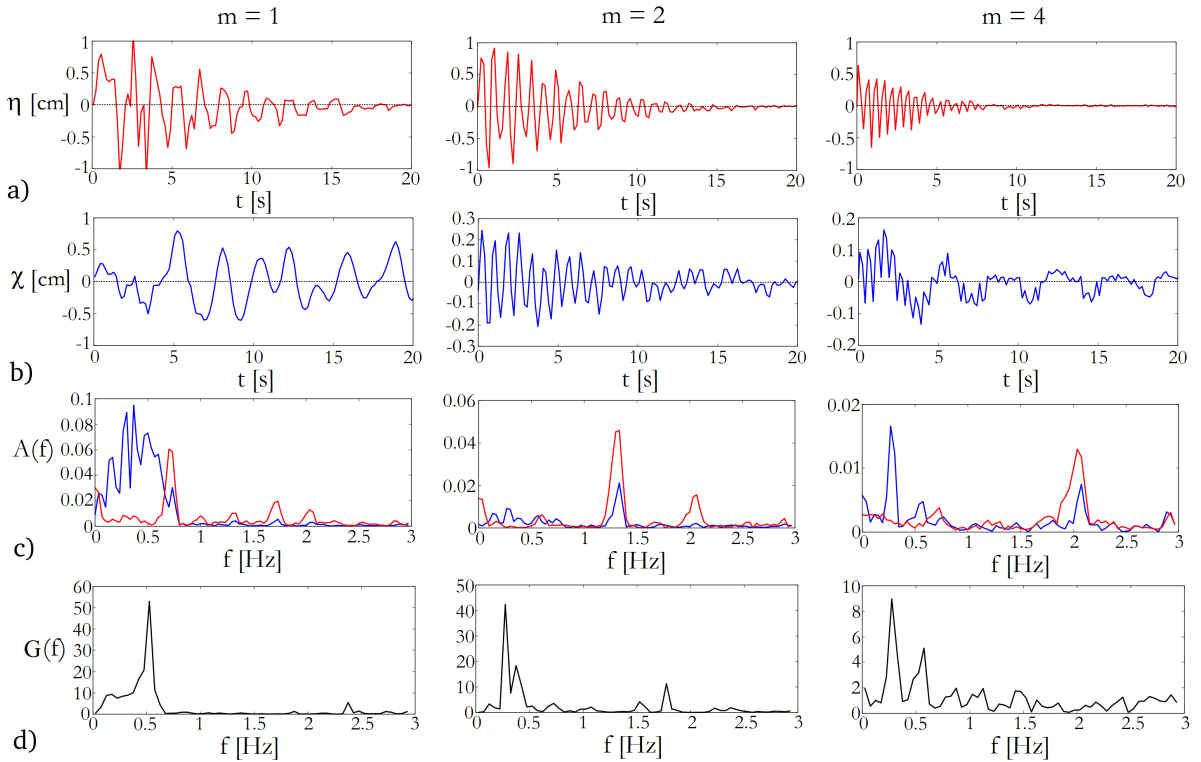


Figure 5.3: **Time series and spectra from three exemplary runs (configuration #1, cf. Table 3.3) of dominant modes $m = 1$, $m = 2$, and $m = 4$ from the left.** The panels of row a) show the water surface displacement as a function of time t from the initiation, as tracked in the close vicinity of the sidewall. The displacement of the pycnocline χ at the sidewall is presented in row b) (note, that here, unlike in the $\eta(t)$ plots, the vertical range is different in all three panels). The Fourier spectra of the $\eta(t)$ (red) and $\chi(t)$ (blue) records are visible in row c), whereas the panels in d) show the transfer function $G(f) = A_\chi(f)/A_\eta(f)$, i.e. the ratio of the spectra of the corresponding two spectra above.

The surface time series acquired at location $x = 0$ can be approximated as a sum of

decaying sinusoidal oscillations in the following form:

$$\eta(0, t) \approx \sum_{i=1}^N A_i \exp(-C_i t) \sin(\omega_i t + \varphi_i) , \quad (5.1)$$

where ω_i , φ_i and A_i denote the frequency, phase shift and initial amplitude of the i -th component, respectively, whereas $C_i(\omega_i)$ is the decay coefficient of the given mode. Eq. (5.1) was fitted to the time series with $N = 2$ as the limit. The standard deviations of the residuals indicated that such two-term sums were sufficient to account for over 90% of the observed displacements in all cases and in many cases even the single-mode fit ($N = 1$) was enough to reach the same precision. It is to be noted here that by using Eq. (5.1), the frequency-dependant coefficients of decay $C_i(\omega_i)$ could be extracted, theoretically, from the “sloshing” of the water surface with any arbitrary initial condition. We chose our initiation method with the different bumper configurations (shown in Fig. 3.6a) representing “quasi pure” modes only for the practical reason of making the regressions to the time series as simple as reasonably achievable.

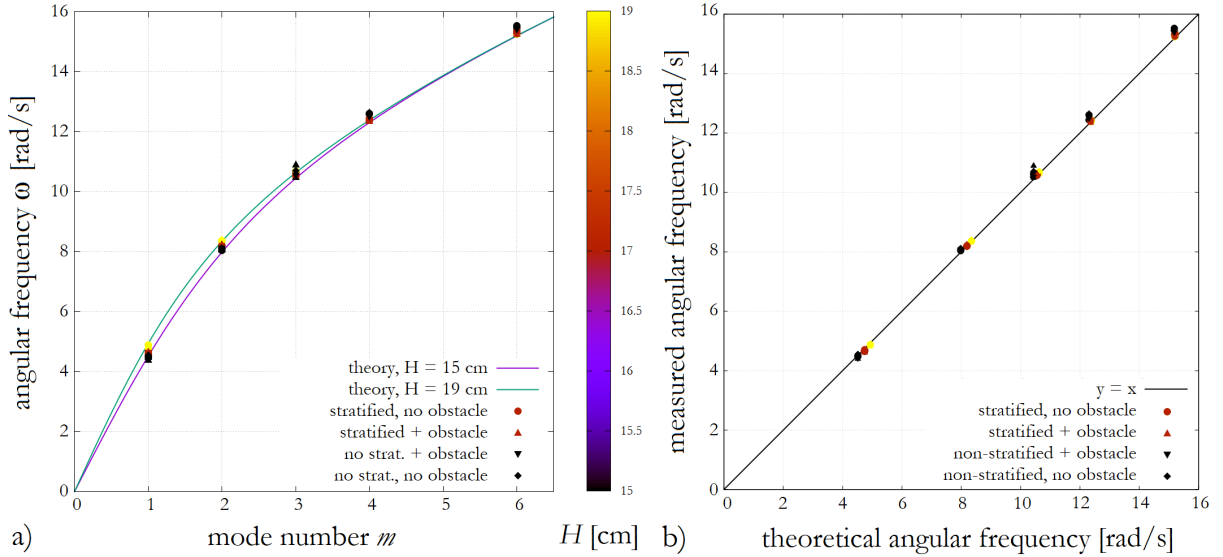


Figure 5.4: **(a) The dispersion relation of water surface waves Eq. (2.23) expressed as a function of dominant mode index m .** The solid curves represent the theoretical relationship for the shallowest ($H = 15$ cm) and deepest ($H = 19$ cm) configurations, and the data points indicate the measured values of angular frequency ω . The coloring is based on the total water height H . **(b) Contrasting the calculated angular frequency ω from Eq. (2.23) to its measured value.** The various experiment configurations are indicated by the shapes of the symbols in both panels (see legend).

The Fourier amplitude spectra $A_\eta(f)$ and $A_\chi(f)$ of the $\eta(t)$ and $\chi(t)$ signals are

presented in Fig. 5.3c with a color coding identical to the corresponding time series themselves. The frequencies of the largest spectral peaks of $A_\eta(f)$ from each experiment were found to be in good agreement (i.e. within 5%) with the linear dispersion relation of homogeneous (non-stratified) surface gravity waves, which reads as $\omega = \sqrt{gk \tanh(Hk)}$ (already presented in Sec. 2.4.3 by Eq. 2.23) where H is the total water depth, g is the gravitational acceleration, and the wave number k is to be taken at $k(m) = \pi m/L$ for the dominant standing wave mode excited in the given run (cf. Fig. 3.6). The match is demonstrated in Fig. 5.4. In terms of the $\omega(m)$ relation, no systematic bias was found from this simple (linear, undamped) theoretical formula regardless of whether the experiment included the obstacle or not, or even whether the water was stratified or homogeneous.

5.2.3 Source-filter dynamics

The surface waves exhibit faster damping than their internal counterparts and the dominant frequency components of the two may also largely differ. It is clearly visible from Fig. 5.3 that the “internal” $\chi(t)$ signals (panels in row b) possess more pronounced low-frequency variability than the $\eta(t)$ oscillations (row a), even in the $m = 2$ and 4 modes, where the classic, topography-induced baroclinic wave generation is practically inhibited – due to the lack of considerable velocity shear at the obstacle – as discussed earlier.

To understand this mechanism it is important to note that even if the surface seiche was a perfectly “monochromatic”, single-frequency source signal, its exponential decay would still unavoidably introduce nonzero amplitudes into the low-frequency range of its spectrum (see, e.g. [139]), making it suitable for the excitation of slow internal oscillations. The resulting signal at the pycnocline can thus be understood as the outcome of a resonance-like amplification of certain characteristic frequency bands of the surface source signal.

The transfer function $G(f)$ of this frequency “filtering”, a widely used tool, e.g. in acoustics [140], can be defined as $G(f) = A_\chi(f)/A_\eta(f)$. Such empirical transfer functions for the experiments of Fig. 5.3 are shown in the panels of row d). In all cases, the maxima of $G(f)$ appear well below the fundamental frequencies $f_i = \omega_i/(2\pi)$ of the source signal Eq. (5.1), consistently with the rule of thumb that interfacial internal propagation is typically around $\sqrt{\Delta\rho/\rho_0}$ times slower than that of surface waves. The question arises of what kind of process determines the observed low-frequency amplification bands of $G(f)$.

In the two-layer approximation, the equation 2.28 (in Subsection. 2.4.4) that describe the dispersion relation of small amplitude interfacial internal waves can be written as:

$$\omega(k) = \sqrt{\frac{gk(\rho_2 - \rho_1)}{\rho_1 \coth(h_1^{(2)}k) + \rho_2 \coth(h_2^{(2)}k)}} , \quad (5.2)$$

note that the equation's notations are presented in Subsection. 2.4.4; k the wavenumber, h_1 and h_2 are the thicknesses and ρ_1 and ρ_2 are the densities of the top and bottom fluid layers – the index ⁽²⁾ indicates the two layer configuration to the stratified system – respectively.

A straightforward way to contrast the linear theoretical dispersion relation with the observed wave propagation is taking the two-dimensional Fourier transform of space-time plots like the ones shown in Fig. 5.2. Then, the time axis is mapped onto the frequency domain ω and the spatial axis is transformed to the wavenumber (k) space. Marked spectral amplitudes are expected to occur along the $\pm\omega(k)$ dispersion relation curves. Examples of such spectra are presented in Fig. 5.5 for the cases of dominant surface seiche modes $m = 4$ and $m = 6$ in experiment series #3 (see Table 3.3) for the surface (panels a) and the pycnocline (panels b). In the surface spectra of panels a) the “quasi pure” initiation yielded sharp peaks (cf. Fig. 5.3) corresponding to the dominant modes (white circles) that indeed lie along the surface dispersion relation Eq. (2.23), plotted with black lines (cf. Fig. 5.4a). The spectra of the pycnocline motion exhibit much more disperse responses, nevertheless we also find that the formula of Eq. (5.2) shown again with black lines (cf. Fig. 5.4b) match the observed distribution of large amplitudes in the low wave-number domain. (Towards higher values of k , three-layer corrections may be necessary as shown e.g. in [74].)

Combining the transfer functions $G(f)$ of all five experimental runs (corresponding to different dominant m values) in a given stratification setting, one can define a cumulative transfer function $\overline{G}(f)$ by assigning the largest value of $G(f)$ obtained throughout all five runs to each frequency f , as represented by the gray shaded area of the combined spectrum in Fig. 5.6a. The dispersion relation Eq. (5.2) enables us to transform the $G(f)$ functions to the wave-number domain, as shown in Fig. 5.6b for four selected stratification settings. Here the frequency $f = \omega/(2\pi)$ is given on the horizontal axis and the wave-number on the vertical one is expressed in the nondimensional units of $L/\lambda = Lk/(2\pi)$, with λ being the internal wavelength and L the length of the tank. (This is a rescaled inverse of the positive branches of the solid black curves in Fig. 5.5b.) The curves therefore represent the inverse of the dispersion relation Eq. (5.2), and their color scale marks the corresponding normalized cumulative transfer function $\overline{G}(f)$ (the normalization was carried out by setting the maximum of the $G(f)$ function as unity for each stratification).

By reorganizing the cumulative transfer functions this way, one can notice that the

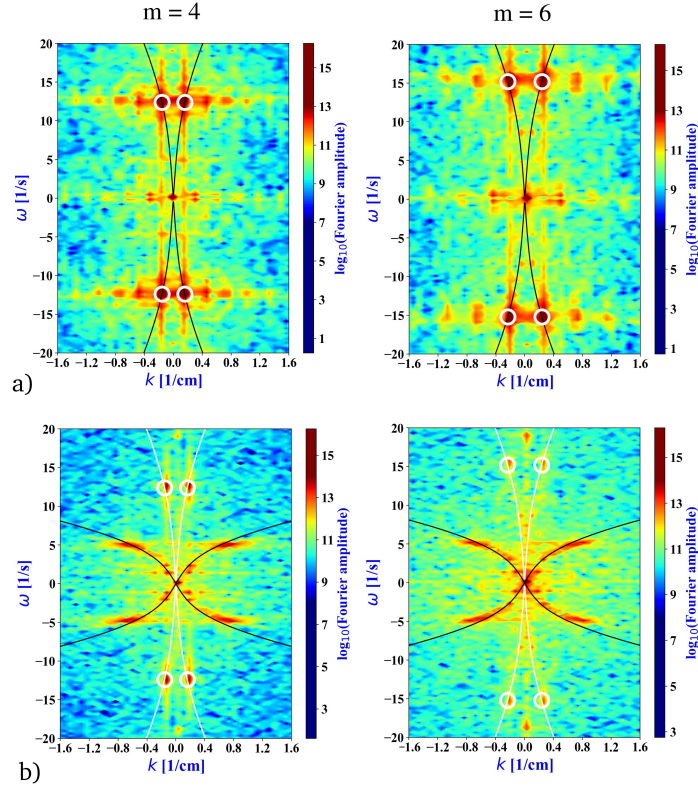


Figure 5.5: **Two-dimensional Fourier transforms of surface displacement $\eta(x, t)$ (a) and of the pycnocline displacement $\chi(x, t)$ (b) in the tank for dominant surface seiche mode $m = 4$ (left) and $m = 6$ (right), experimental configuration #3.** The white circles mark the dominant surface wave peak, whereas the black solid lines represent the respective dispersion relations Eqs. (2.23) and (5.2).

amplification peaks (high values of \overline{G} , colored yellow) tend to appear in the close vicinity of integer values of the nondimensional wave number, e.g. at $L/\lambda = 2; 3; 5$ and 8 , as marked by dotted horizontal lines in Fig. 5.6b. These low frequency resonance peaks are thus seem to be related to standing wave generation at the pycnocline – internal seiche modes – whose wavelengths can fit integer times into the tank. Despite having much lower oscillation frequencies than the main peak of the “source” signal, these modes can still get excited. It is due to the fact that the damping of the surface seiche excites considerable amplitudes in the low-frequency spectral domain with which the internal standing waves can resonate.

Although Fourier transform exhibits informative insight about the of the possible frequency domain, it doesn’t give localized information. therefore, for quasi-stationary signals we tested the wavelet spectrograms of the time series obtained using the so-called

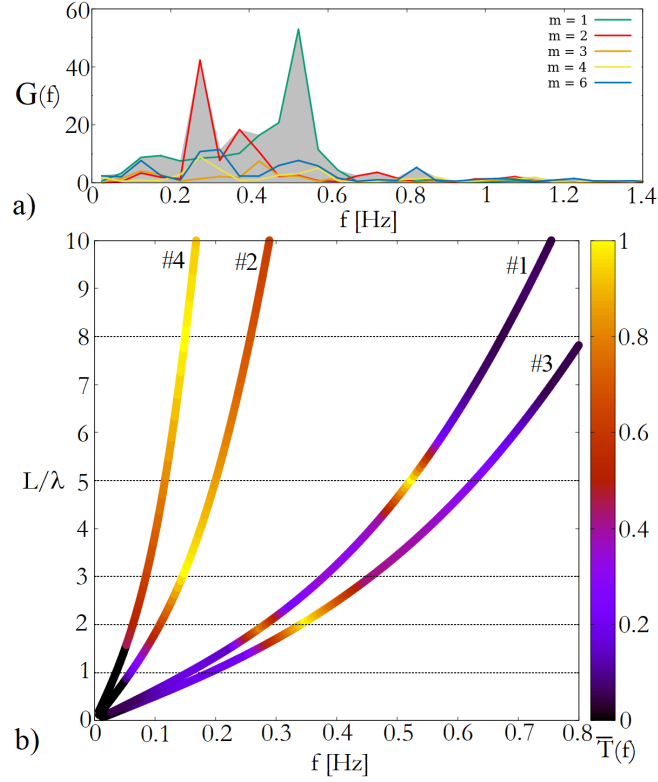


Figure 5.6: (a) The transfer functions $G(f)$ of all dominant excitation modes m in experiment series #1, and their cumulative transfer function (grey shaded area). (b) The internal wave (inverse) dispersion relations as a function of frequency f for four exemplary stratification settings (representing series #1, #2, #3, and #4, cf. Table 3.3). The coloring marks the normalized cumulative transfer functions $\bar{G}(f)$ as acquired from the corresponding experiment series.

Morlet wavelet (aka Gabor wavelet) yielded reassuring results, when comparing their patterns to the $G(f)$ transfer spectra. Wavelet transforms are generally more suitable to handle time series with time-dependent spectral structure. Some of our findings are presented in Fig. 5.7, showing an exemplary $G(f)$ transfer spectra (analogous to those presented in Fig. 5.3) and the corresponding wavelet spectrograms for the surface and interface time series extracted from the vicinity of the left-hand sidewall of the tank. Time scale (“period T ”), shown along the vertical axis represents the width of the Morlet window (when T increases, it means that the Morlet is becoming wider), and it gives higher wavelet coefficient values (color coding) when it fits locally to the time series. Thus, we can see the damping of surface modes (upper spectrogram), and the appearance and disappearance of various modes at the internal interface (bottom spectrogram).

On the bottom spectrogram, the notation is the following. The horizontal black

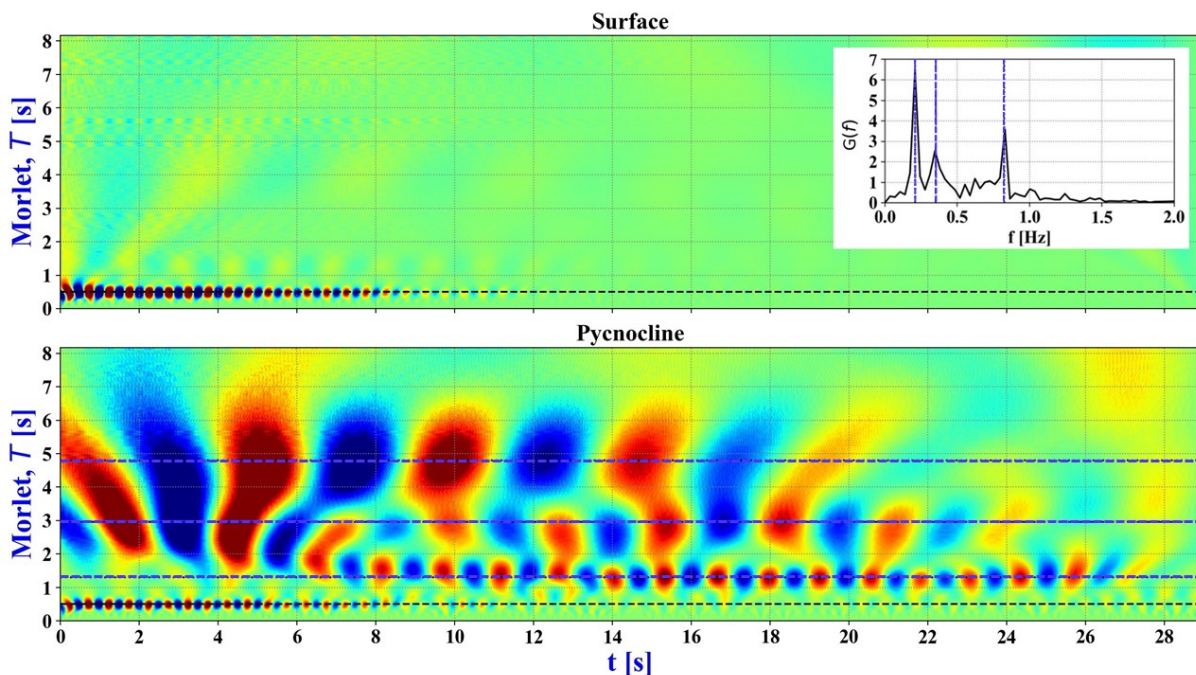


Figure 5.7: Morlet wavelet spectrograms of the time series of surface displacement $\eta(x, t)$ ('top') and of the pycnocline displacement $\chi(x, t)$ ('bottom') in the tank for dominant surface seiche mode $m = 4$, while the inset plot ('top left') represents the transfer function in experimental configuration #3. Time series extracted from the vicinity of the left-hand sidewall of the tank. The colors refer to the wavelet coefficient.

dashed line is always the fundamental surface mode from the simple surface dispersion relation of Eq. 2.23. Dashed blue lines belong to the peaks (simply $T = 1/f$) in the transfer function (see the subplot in Fig. 5.7). It is visible that the peaks of the transfer function $G(f)$ indeed coincide with actual detectable oscillations. (Which, as it turns out in our Fig. 5.6b of the new version, also coincide with internal seiche modes.)

5.2.4 Topographic energy conversion

The damping of surface waves in a stratified system is caused by the combination of factors such as the friction with the basin boundaries, diapycnal mixing, and barotropic-to-baroclinic energy conversion due to topographic effects. To separate the contribution of the latter we conducted control experiments with each studied stratification profile where the obstacle was removed from the tank. We then compared the observed decay rates with the ones acquired with the obstacle in place.

The scatter plot in Fig. 5.8a contrasts the the decay coefficient of the dominant

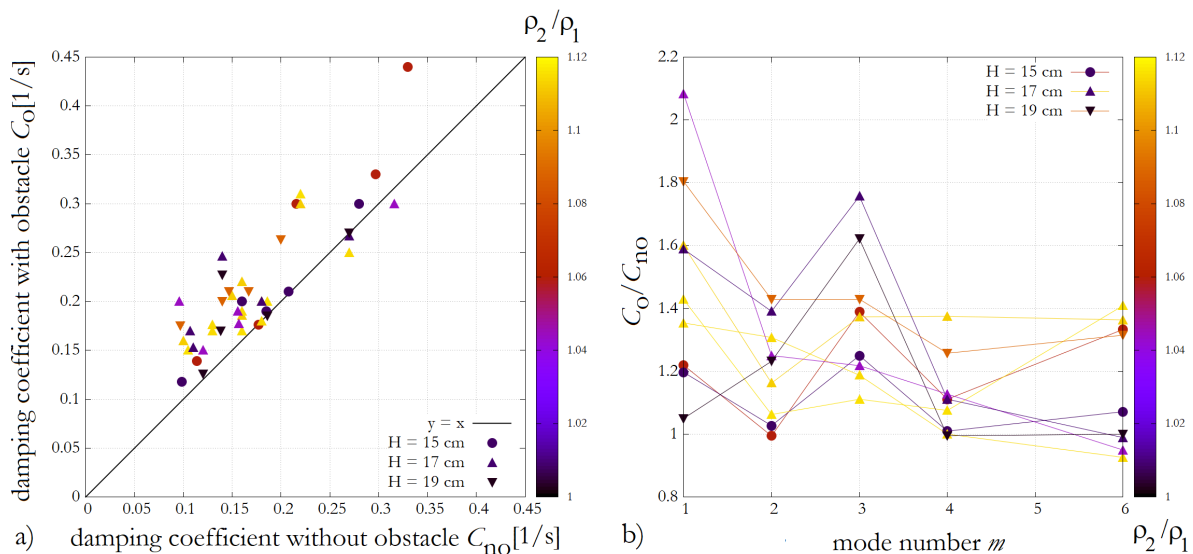


Figure 5.8: (a) Comparison of dominant mode surface seiche decay coefficients in paired experiments without (horizontal axis) and with (vertical axis) bottom obstacle. The solid line represents $y = x$. (b) The ratio of the damping coefficients C_o/C_{no} of paired experiments with and without obstacle as a function of dominant surface seiche mode index m . Symbol shapes and coloring mark the total water depth and the density ratio of the two layers, respectively, in both panels (see legend).

surface seiche mode C_o – from fitting formula (5.1) – in each experiment with obstacle (hence the index o), with the corresponding no-obstacle value C_{no} . It is clearly visible that almost all data points spread in the $C_o > C_{no}$ domain, but no systematic relationship could be found with the density ratio of the two layers (indicated by the coloring), or total water height H (marked by the different symbol shapes, see legend).

There is, however, a marked difference between the two configurations in terms of the m -dependence of the decay coefficients, as shown in Fig. 5.8b, where the C_o/C_{no} ratios are plotted for each experiment pair as a function of mode index m . Apparently, the relative increase of barotropic energy dissipation (damping) compared to the no-obstacle setting is the largest – up to a factor of 2.1 – at the odd wave-numbers $m = 1$ and 3 (note that the $m = 5$ mode could not be excited due to technical reasons, as mentioned earlier). This is in concert with the qualitative description provided in subsection 5.2.1, where we demonstrated that large amplitude internal waves having the same frequency as the surface wave are excited when the obstacle is situated below a surface seiche node.

5.3 Energy conversion in Gullmar fjord vs laboratory observations

In what follows, we discuss the implications and applicability of our findings to actual sill fjords in nature, e.g. the Gullmar fjord of Sweden, whose internal wave excitation dynamics served as motivation for our work. For this particular fjord [25] applied an analytical two-layer model for a simplified rectangular geometry and – despite its simplicity – have found a strikingly good agreement with field data when predicting the surface seiche decay coefficients C using only the approximate geometrical dimensions of the fjord, and the densities and thicknesses of the layers.

Their formula (based on an earlier work, [67]) as applied to our experimental geometry, takes the form

$$C = \frac{8h_2\omega^2 L}{\pi^2 g H h_1} c_0, \quad (5.3)$$

where, as before, ω denotes the forcing frequency. The approximations used for eq. (5.3) – besides the ones mentioned above – include linearity and the shallow-layer assumption, which manifests in the factor $c_0 = \sqrt{g\Delta\rho h_1 h_2 / (\rho H)}$ (Eq. 2.29), i.e. the phase velocity of the interfacial internal waves in the (non-dispersive) long-wave limit. This limit is encountered when $kH_r \ll 1$ holds, where k denotes the (horizontal) wavenumber and $H_r \equiv h_1 h_2 / H$ is referred to as the “reduced thickness”, a characteristic vertical scale of the system. Substituting the parameters of the Gullmar fjord or those of the Oslofjord (studied in [67]) one indeed gets $kH_r \approx 0.02$ and 0.002 , respectively, due to the fact that the forcing frequency ω is on the order of $\sim 10^{-4}$ rad/s in both cases, yielding small values for k ($= \omega/c_0$), well within the long-wave regime. In our laboratory setting, however, the internal waves are manifestly dispersive (cf. Figs. 5.5 and 5.6) and are found in the $H_r k > 1$ range even for the slowest excitation investigated. Hence here the full dispersion relation (2.28) has to be considered; (5.3) would significantly overestimate the decay coefficients.

The question arises of how relevant these experimental findings can then be for the better understanding of actual fjord systems. For instance, assuming an identical stratification profile to that of the Gullmar fjord, but a much shorter external (surface) seiche period of 100s, from the inverse of (2.28) we get $H_r k \approx 3.5$. Seiche periods of this timescale are not uncommon: the Norwegian Framfjorden for example exhibited surface standing waves with amplitudes reaching up to 1.5 m and with periods of 67–100s triggered by the giant 2011 Tohoku earthquake, whose epicenter was located in the distant Japan [141]. Our finding that the surface seiche-induced internal waves can be largely dispersive in-

icates that in such situations (short-period oscillatory forcing) a modified version of eq. (5.3) is to be applied, in which c_0 is replaced with the phase velocity $c = \omega/k(\omega)$, where $k(\omega)$ is the inverse function of (2.28) for a given forcing frequency ω .

Another related observation is that the propagating interfacial internal waves appear to follow the dispersion relation derived from a *linear* wave equation quite well, despite exhibiting vertical displacements χ that are not negligible when compared to the typical reduced height of $H_r \approx 3$ cm in the experiments (cf. Figs. 5.2 and 5.3). Generally, large interfacial amplitudes ($\chi \sim H_r$) are expected to necessitate considerable nonlinear corrections to the wave velocities, as demonstrated e.g. in a resonant two-sill configuration by [42]. In the present setting, however, the linear wave theory performed fairly well. This finding is of relevance for actual sill-fjord dynamics, since there, too, pycnocline displacement χ is often comparable to H_r . In the case of the Gullmar fjord, for instance, internal amplitudes of $\chi \approx 5 - 10$ m are typical [142], whereas the reduced height is $H_r \approx 19$ m [25]. Thus our experiments confirm that it indeed appears to be sufficient to apply linear wave theory in such situations, as far as the wave speeds are concerned.

A further nondimensional quantity that is of relevance for the barotropic-baroclinic energy conversion is the ratio $\langle\chi\rangle/\langle\eta\rangle$ of the time-average vertical displacement at the pycnocline and at a surface antinode. The decay coefficient C of the surface oscillation can also be measured using the natural timescale of the problem, the period of the dominant seiche mode, as C/ω . Expressing C/ω as a function of $\langle\chi\rangle/\langle\eta\rangle$ hence connects the ratio of the energy stored in the waves of the two layers (the energy scales with the respective squared amplitudes) and the rate of surface energy decay.

The result is shown in the log-log scatter plot of Fig.5.9 for the experiments in which the $\chi(t)$ record was available for evaluation. The data points appear to follow the empirical relationship $C/\omega \sim (\langle\chi\rangle/\langle\eta\rangle)^{0.28 \pm 0.04}$ (dashed line in Fig.5.9).

Taking the respective parameters from the Gullmar fjord field data as reported in [25] and [142] yielded the red data point in Fig.5.9, whose error bars represent the range in which the data scatter. Interestingly, this data point also appears in the vicinity of the fitted curve, which suggests that the dynamics in the experimental and natural settings are indeed connected. The detailed investigation of this finding would, however, require field data from other sill fjords of similar bathymetry as well, which is beyond the scope of the present study.

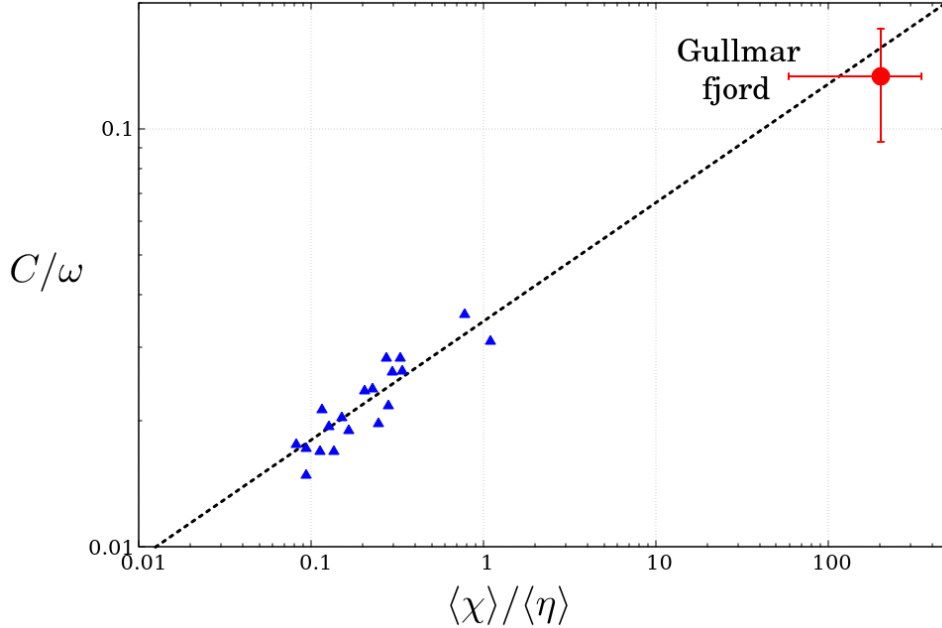


Figure 5.9: **Nondimensional decay coefficients as a function of pycnocline vs. surface average displacement ratios for laboratory experiments (blue triangles) and for the Gullmar fjord (red circle).** The dashed line represents the power law fit of $C/\omega = (0.035 \pm 0.002) \cdot (\langle \chi \rangle / \langle \eta \rangle)^{0.28 \pm 0.04}$

5.4 Discussion

In this experimental study, we analyzed the coupling between surface seiche modes and internal wave dynamics in a quasi-two-layer stratified system, and the effect of a topographic obstacle on the damping of the surface seiche. The decaying surface oscillations were initiated by a wave maker in a pulse-like manner, and the adjustable shape of this device enabled us to excite surface standing waves of rarely observable larger wave-numbers.

Two pathways of barotropic-to-baroclinic conversion were uncovered. Firstly, the “direct” excitation of short-wavelength propagating internal waves via the horizontal velocity shear emerging in the vicinity of the obstacle. These waves were easily noticeable along the pycnocline due to their relatively large amplitudes. Their periods matched the dominant sloshing timescale associated with the surface seiche. It is to be noted that the most pronounced wave excitation, and thus the most prominent increase in the decay coefficient of the surface seiche was detected in the situations where the surface (standing) waveform was such that a node of the surface displacement was located above the bottom obstacle, that – in the geometry investigated here – means seiches of odd wave-number

indices. (Only in these modes there is substantial current over the obstacle.)

Secondly, we found evidence for the excitation of slow, long wavelength internal seiche modes, whose half wavelength can fit roughly integer times onto the pycnocline between one sidewall and the obstacle (i.e. onto the half of the total basin length). The occurrence of such internal oscillations in this system is interesting as they have much lower characteristic frequencies than the surface seiche, i.e. the source signal. It appears, indeed, that a nontrivial source-filter dynamics can describe this phenomenon: the spectral structure of the decaying source signal includes non-zero amplitudes in the low-frequency range that can resonate with certain internal standing wave modes whose wavelengths are such that they fulfil the geometrical boundary conditions, representing a “band-pass filtering”.

Comparing the dominant seiche decay rates with those from control runs without bottom topography, we demonstrated that in almost all cases internal wave activity yields a detectable increase of the damping, also for even seiche mode indices, where the “short wave” excitation is inhibited, as discussed above. In these cases internal wave dynamics can be attributed to the aforementioned slow wave (internal seiche) excitation pathway, but even this lesser effect appeared to be enough to yield substantially larger damping than the flat-bottom control runs.

Our findings are of relevance for the better understanding of baroclinic wave excitation in quasi two-layer sill fjords, as they demonstrate that the waves generated in such systems can be treated fairly well using the dispersion relations of the linear two-layer theory in cases where the surface forcing frequencies are large, e.g. in earthquake-induced fjord seiches reported by [141]. We also demonstrated that in this particular system, non-linear corrections to internal wave speeds are negligible, despite the fact that internal wave amplitudes are often comparable to the characteristic vertical scale of the stratification H_r , similarly to the case of natural sill fjords.

Chapter 6

Combined wind-solar electricity production potential over north-western Africa

6.1 Introduction

Access to electricity can play a critical role in sustainable development in Africa [143, 144, 145]. In September 2015, United Nations member states adopted a comprehensive global development agenda known as the Sustainable Development Goals. The 17 goals cover everything from poverty, hunger, health, education, gender equality, water to climate, peace and justice, among others [146]. Goal 7 entitled “Ensure access to affordable, reliable, sustainable and modern energy for all” with an emphasize on renewable resources. In the past decade, the population with access to electricity increased by 1 billion people (reaching $\sim 90\%$ of the global population), still around 800 million individuals, mostly living in rural areas, lack this fundamental service [146]. There were promising improvements at several regions, particularly in Latin America and South-Eastern Asia, however the population growth in Africa was faster than the increase of access to electricity. The development of energy sector, especially the expansion of modern solar and wind resources is hindered by several factors in Africa including the lack of initial capital, lack of skilled manpower, weak maintenance service, poor infrastructure and institutional background, etc.[143, 147, 148].

It is a crucial fact that economic growth is vital to reduce poverty and improve life quality, especially because the majority of African economies belongs to low income and middle income countries. It is expected that a long term investment into renewable en-

ergy sources leads to a significant positive economical impact in most African countries, while in short terms, even negative growth may occur in western Africa [149, 150, 151] if renewable sources continue to rely mainly on wood [152]. Therefore, it is important to intensify switching to renewable energy resources (wind, solar) as a critical step towards sustainable development [153, 154]. Even in the lack of proper economic and infrastructural circumstances, the fact is that the climate over a large part of the African continent provides excellent opportunities for installing solar and wind electricity facilities, as we will demonstrate in this Chapter focusing on an area which extremely depends on fossil fuels to fulfil the need of energy.

The spatial and temporal variability of climate variables and intermittency of renewable electricity sources have a vast literature, for a recent review see Engeland et al. [155]. Somewhat less attention has been paid on combined (the other term is hybrid) solar and wind power systems, however the interest is continuously increasing [156, 157] [158, 159, 160]. Complementarity of various renewable resources, such as wind, solar and hydropower has been studied in all continents, Africa is somewhat underrepresented [156] [160]. Suitable geographic locations where wind and solar resources exhibit temporal anti-correlations have been identified in Australia [161], in the north-eastern part of the Arabian Peninsula (on a monthly time scale) [162], over the European subcontinent when solar and wind power are integrated across Europe [163, 164], in Sweden (grid integrated) from hourly to yearly timescales [165], in the Iberian Peninsula [166, 167], Argentina [168], China [169] and a couple of other locations (see also the literature in the reviews by Jurasz et al. [157], Solomon et al. [158] and Weschenfelder et al. [159]). These studies have been introduced simpler and more complicated measures to characterize complementarity starting from the temporal correlations on various timescales to the more demanding principal component analysis and canonical correlation analysis [167]. Note that temporal complementarity depends on the timescales considered, e.g., it can be present on seasonal or annual scales but it is practically negligible in hourly or daily intervals [157] [170].

In order to estimate wind and solar electricity production potential, we analyze ERA5 reanalysis data of high spatial and temporal resolution over north-western Africa. Our target location is centered around Algeria, including the Mediterranean Sea. The dominating geographic feature of the region is the Sahara, which lacks surface vegetation almost entirely. Low vegetation refers to crops and mixed farming, irrigated crops, short grass and tall grass in this area (Figure 6.2a), while high vegetation (evergreen trees, deciduous trees, mixed forest/woodland, and interrupted forest) is practically present only along the coasts of the Mediterranean Sea and the Atlantic Ocean (Figure 6.2b). Regardless of mountain ranges in the extreme northern part of Africa and Tassili n'Ajjer

mountains in the south of Algeria, huge land surface tends to be flat (Figure 6.2c). Data analysis revealed two peculiar features over the Sahara. A comparison of wind speeds at 10 m and 100 m altitudes indicates steep vertical wind profiles over the Sahara, where wind velocities at larger heights are comparable with wind velocities over open sea. This provides an optimal circumstance for on-shore wind electricity generation with capacity factors similar to the off-shore facilities demanding much larger initial capital.

The second peculiarity is observed by evaluating high temporal resolution (1 hour) wind and insolation records in the central part of region denoted by a black rectangle in Fig. 6.8. Namely, the wind at 100 m altitude is significantly intensifies during the nighttime periods over extended regions. This provides an opportunity to integrate wind and solar electricity in a grid, where the output is substantially smoother than in the case of either wind only or solar only generation. The most suitable area (centered at In-Salah province) is very far from the densely inhabited coastal regions, however as a first step, proper installations can supply the local population (Like In-Salah and Taman-rasset provinces, estimated total population is around 165 thousands inhabitants). For this reason, we do not consider any grid integration issue, we assume distributed energy production.

6.2 Data and methods

In this analysis we used the fifth generation ECMWF atmospheric reanalysis of the global climate ERA5 [171], which combines model data with global observations into a complete and consistent gridded ($0.25^\circ \times 0.25^\circ$) dataset on 137 pressure levels spanning from the surface of the Earth up to the 0.01 hPa level, from 1979 onward (regularly updated) with a temporal resolution of 1 hour. (In a preliminary version, ERA5 reanalysis backward extension is available from 1950 to 1978, too.) The time variable assigned to all data is in UTC (Universal Time Coordinated), fortunately the largest part of our target area belongs to the UTC+0 time zone. Table 6.1 lists the variables we evaluated in this study.

As for the wind component parameters of eastward (u -), northward (v -) wind speeds at altitude of 10 m ($u10$, $v10$), and 100 m ($u100$, $v100$), it is important to note that they represent averages over a model grid box and the native time step of 1 h. In the absence of measurement data, we could not validate the particular reanalysis time series we used, nevertheless in an earlier work [172], a very good agreement was concluded between properly averaged and scaled nacelle anemometer records at a hub height of 65 m and ERA-Interim $u10$ and $v10$ reanalysis parameters. Since meteorological observations are usually local to a particular point in space and time, differences are present, however they

do not affect significantly a statistical evaluation [172]. A recent intercomparison of five reanalysis data banks and tall tower wind observations concluded also that ERA5 surface winds offer the best agreement in correlating and reproducing the observed time evolution and variability [173]. Nevertheless a few times per year, the analysed low level winds (both at 10 m and 100 m), become unrealistically large in particular locations. For example, stored wind speeds at 100 m in the period of 1 October, 2018 - 30 November, 2018 are larger than $4.6 \times 10^4 \text{ ms}^{-1}$, therefore it is easy to filter them out as extreme outliers, and the period after this month is not taken in consideration in our analysis. Point errors (specific grid point at a given time instance) are corrected by linear interpolation.

Table 6.1: **ERA5 variables used in this work.** 'Id' refers to the short name of parameters in the ERA5 nomenclature. Note that *ssrd* is an accumulated parameter, mean flux (Wm^{-2}) is obtained by dividing with the integration time (3600 s). Geopotential height h is defined as the local geopotential z divided by the standard gravity at mean sea level ($g_0 = 9.80665 \text{ ms}^{-2}$).

Id	long name	units
<i>cvl</i>	Low vegetation cover	[0-1]
<i>cvh</i>	High vegetation cover	[0-1]
<i>z</i>	Geopotential	m^2s^{-2}
<i>u10</i>	10m u-component (eastward) of wind	ms^{-1}
<i>v10</i>	10m v-component (northward) of wind	ms^{-1}
<i>u100</i>	100m u-component (eastward) of wind	ms^{-1}
<i>v100</i>	100m v-component (northward) of wind	ms^{-1}
<i>ssrd</i>	Surface solar radiation downwards (accum.)	Jm^{-2}

The geographic region of our work (see Fig. 6.1) is located over north-western Africa. The spatial resolution is $0.25^\circ \times 0.25^\circ$, which means 93×101 (latitude \times longitude) grid cells. We examined nearly four decades with a temporal resolution of 3 hours, which was enough to represent diurnal variations with a reduced data mass. The four periods were the following: 01/01/1981 - 12/31/1990; 01/01/1991 - 12/31/2000; 01/01/2001 - 12/31/2010; and 01/01/2011 - 09/30/2018. Since we did not remark any observable differences between the decades in our particular statistical tests, we mostly present results for the last period. The main exception is the full resolution analysis focusing on the Sahara (Fig. 6.8b indicated by black rectangle in Fig. 6.8a), where 1 hour *ssrd* (shortwave solar radiation downward) and $s = \sqrt{u^2 + v^2}$ (wind speed) time series are evaluated in the period of 01/01/2007 - 09/30/2018 (33×33 grid cells, 102983 data points for each).

The temporal resolutions of 3 hours for the whole study area, or 1 hour for Central Algerian Sahara are not fine enough to consider issues in power system operation (usually

based on steps of 15 min). In this respect, our study is a conceptual one based on multi-annual statistical and correlation properties of wind and solar resources.

The parameter *ssrd* represents the amount of incoming flux of solar radiation on a horizontal unit surface. This parameter comprises both direct and diffuse solar radiation and cloud effects. Radiation from the Sun is partly reflected back to space by clouds and aerosol particles in the atmosphere and some of it is absorbed, the rest is incident on the Earth’s surface. To a reasonably good approximation, the parameter *ssrd* is the model equivalent of what would be measured by a pyranometer.

6.2.1 Spatial correlations of wind fields

In order to characterize spatial correlations of wind speeds between different geographic locations, we determined the Pearson correlation coefficient matrix R of the time series for each pair of grid points, a matrix of size 9393×9393 . The standard definition of R is

$$R^{i_s, j_s} = \frac{\langle [i_s(t) - \overline{i_s(t)}][j_s(t) - \overline{j_s(t)}] \rangle_t}{\sigma_{i_s} \sigma_{j_s}}, \quad (6.1)$$

where the overline indicate mean value, the nominator is a temporal mean value of the products, and σ_{i_s} and σ_{j_s} are standard deviations for the two grid points i and j . All calculations were performed in a Python environment (version 3.6) predominantly with the standard Numpy and Scipy packages, maps were drawn by the Basemap module.

Pearson correlation is the most common metric for the evaluation of a *linear association* between two time series, see. e.g., Table 1A in Ref. [157]. Its mathematically rigorous foundation requires memory-less, Gaussian distributed, infinitely long random sequences, none of which holds for environmental parameters. A somewhat more flexible metric for an evaluation of arbitrary but *monotonous association* between two time series is provided by the Spearman rank correlation coefficient:

$$\rho^{i_s, j_s} = \frac{\text{cov}[r^{(i_s)} r^{(j_s)}]}{\sigma_{i_r} \sigma_{j_r}}, \quad (6.2)$$

which is simply Pearson’s correlation coefficient applied to the *ranks* of the observations. Ranks are obtained by an assignment of ordering labels “first” (e.g. largest), “second” (second largest), etc. to a series of observations of a particular variable. This metric was used in a couple of complementarity studies, see Ref. [157], and most recently in [160, 170].

6.2.2 Wind electricity estimate

The wind turbine power curve provided by the manufacturers exhibits the relationship between a wind turbine output electric power and hub height wind speed [174]. After an appropriate rescaling (usually by the rated power), the power curves are very similar for various turbine constructions. Several operational functions are developed to provide an "universal" mathematical expression for normalized power curves. Note that the only purpose of such an operational form is to give a smooth relationship between input speed values and output power based entirely on empirical data; therefore neither the mathematical forms nor the number of parameters are unique [174]. We adopted the following semi-empirical form which was proven to provide a reasonable fit for recorded power output data [172, 175, 176]:

$$\begin{aligned}
 P(s) &= a_0(s - s_{ci})^\alpha & s_{ci} \leq s \leq s_x \\
 &= \frac{a_1}{1 + \exp[-(s - a_2)^\beta]} & s_x < s \leq s_{co} \\
 &= 0 & s < s_{ci}, \quad s > s_{co}
 \end{aligned} \tag{6.3}$$

Based on Ref. [176], where factory power curves were rescaled by the rated power for 6 different turbines and fitted by Eq. 6.3, the following parameters are adopted in the subsequent parametric model calculations: cut-in wind speed $s_{ci} = 2.5 \text{ ms}^{-1}$, crossover speed (crossover to the rated power plateau) $s_x = 10.0 \text{ ms}^{-1}$, and cut-out speed $s_{co} = 25.0 \text{ ms}^{-1}$. The further empirical parameters are $a_0 = 0.935$, $\alpha = 2.14$, $a_1 = 100\%$, $a_2 = 9.16 \text{ ms}^{-1}$, and $\beta = 1.05$ (see Fig. 4 in [176]).

The first equation in the piece-wise nonlinear set (3) reflects the power law dependence of the output power in the range between the cut-in speed s_{ci} and crossover speed s_x . The well-known theoretical value of the exponent is 3, the empirical data of factory power curves reflect somewhat lower values between 2 and 2.5. The second equation between the crossover speed s_x and the cut-out value s_{co} describes the regularized regime where the output quickly converges to the nominal peak power resulting in the well known plateau (optimal operating range). The form is a simple logistic function shifted properly to approach the rated power.

6.2.3 Combined solar and wind electricity estimate

As for an estimate of solar power alone, we use the following considerations. The electric output power of a photovoltaic (PV) panel depends linearly on the incoming flux of the

solar radiation. For an optimum positioning of a PV panel away from the equator, it should be properly tilted to receive more direct and less grazing incidence radiation. Jacobson and Jadhav [177] determined globally an optimal tilt angle and insolation gain relative to horizontal for all countries of the world. Considering our test area centered in the In-Salah region, Sahara, at the northern edge (33°N) the optimal tilt angle of *fixed PV panels* is around 28-29°, while at the southern edge (25°N) the optimum is around 24-26° (see Fig. 2 in [177]). Accordingly, the gain of short wave radiation flux is a factor between 1.10 and 1.15, see Fig. 5b in [177]. We use this correction factor by estimating PV output power as a function of downward solar radiation flux *ssrd*. Note that the optimal tilt angle and azimuth of a PV panel change hour by hour following the daily solar cycle and seasonal variation of the elevation of the Sun. However, such Sun-tracking mechanisms are expensive and demanding steady maintenance, therefore we consider the common compromise of fixing the tilt and azimuth (southern direction) which results in the maximal annual mean output [177].

Other known small corrections (e.g. the temperature of the PV panel, possible cloud shadowing, dust cover etc.) are omitted. Nevertheless, dust cover might be a serious issue in the Sahara. Several studies concluded that accumulation of dust on the surface of photovoltaic cells causes a significant degradation of electricity generation [178, 179, 180]. A recent experimental study [180] found that a sand cover of 100 gm⁻² decreases the output power by ~12%, however a weekly dry cleaning (brushes and clothes) reduces the power loss to less than 1%.

The simplest model of an aggregated output of solar and wind electricity P_{tot} as a function of time t consists of a single parameter, the resource fraction $0 \leq c \leq 1$ which is the ratio of wind and solar contribution to a total rated power of 100% (see e.g., [176]):

$$P_{tot}(t) = c \times P_{wind}(t) + (1 - c) \times 0.1 \times 1.125 \times ssrd(t) \quad (6.4)$$

Here the coefficient 0.1 on the right hand side follows from the practice that the rated output power (100%) of a solar panel is determined at 1000 Wm⁻² perpendicular insolation and at a panel temperature of 25°C, but we neglect temperature effects here. The factor 1.125 is simply the mean gain of insolation at optimal tilt angles, as discussed above. The wind power output $P_{wind}(t)$ is estimated by transforming the wind speed $s_{100}(t)$ with eq. 6.3. The two limiting values $c = 0$ and $c = 1$ belong to pure solar and pure wind electricity generation.

6.3 Results

6.3.1 Mean wind speeds and capacity factors

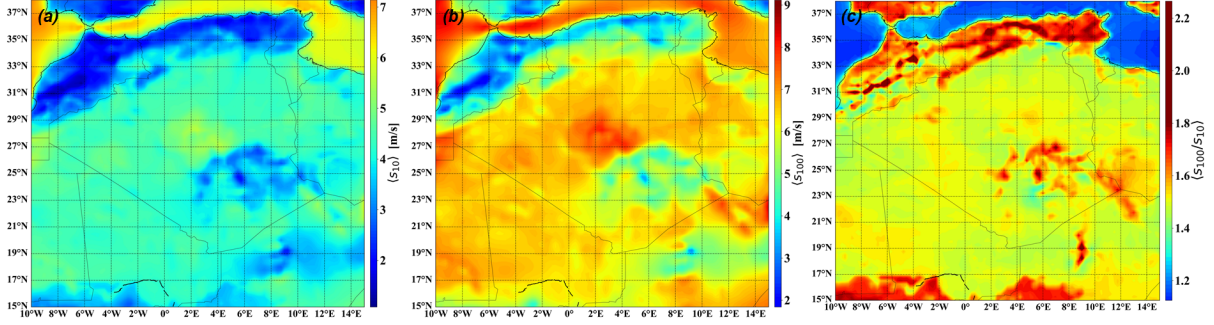


Figure 6.1: **Geographic distribution of mean wind speed** $s = \sqrt{u^2 + v^2}$ (a) at 10 m, and (b) at 100 m altitude. (c) **Temporal mean of instantaneous wind speeds ratio** s_{100m}/s_{10m} . The evaluated period is from 01/01/2011 to 09/30/2018. Note the different color scales.

Mean wind speeds at heights of 10 m and 100 m represented in Figs. 6.1a and 6.1b, determined from wind speed data-sets cover the period of almost 8 years with a resolution of 3 hours. It is shown in Fig. 6.1b that mean Saharan wind speeds at 100 m altitude are comparable to the open sea areas, as the Mediterranean Sea and the Atlantic Ocean, while it appears lower at 10 m altitude. It indicates that the vertical wind profile is steeper over the Sahara, that is suggested in Fig. 6.1c by the instantaneous ratios s_{100m}/s_{10m} which are substantially larger (1.5-1.6) than over the open sea (1.1-1.2). Although the highest wind speed ratios (>2) still associated with the Atlas, Tassili regions and coastal areas, the mean wind speeds are overly weak at both heights. In the North, the areas close to the coast – among the highest wind speed ratios (red dark coloring in Fig. 6.1c) and low surface wind speeds (blue-green coloring in Fig. 6.1a) – strongly overlap with zones covered by low and high vegetation (see Fig. 6.2a,b). Another interesting fact is that the same areas are characterized by high elevations in the northern mountain ranges as Tell Atlas, Saharan Atlas (see Fig. 6.2c). Tassili n’Ajjjer (southern mountain systems in Algeria) with no vegetation cover also encounters weak wind speeds; as weak as in the side of flat Sahara where the vegetation cover is low (example in the extreme South of the studied geography). Indeed, it is likely that complex orography and vegetation cover are the reasons of wind speed profile steepness in the considered region.

From the relatively large hub-height mean wind speeds at 100 m over the Sahara we imply that the capacity factors of wind electricity generation is reasonably comparable with off-shore wind farms. The *capacity factor* is simply the ratio of *total realized output*

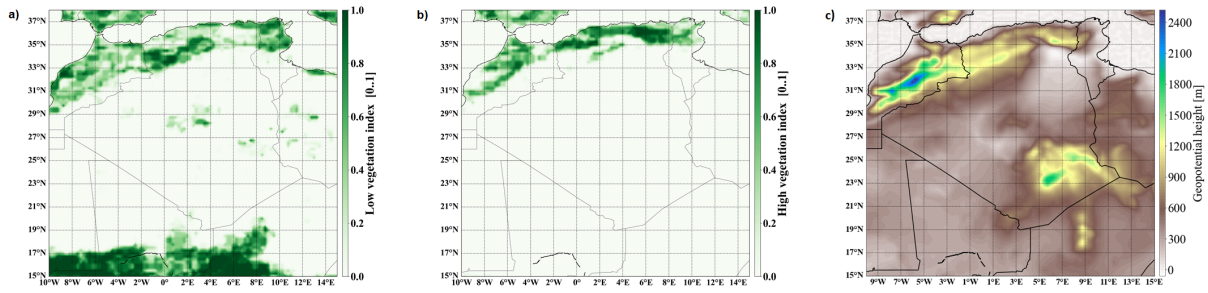


Figure 6.2: (a) 'Mean low vegetation cover index' (crops and mixed farming, irrigated crops, short grass and tall grass). (b) 'Mean high vegetation cover index' (evergreen trees, deciduous trees, mixed forest/woodland, and interrupted forest). (c) Mean geopotential height over the year 2018. Mean 'vegetation cover' indices $[0 \dots 1]$ between 2011-2019 from the ERA5 reanalysis data bank. Spatial and temporal resolutions are $0.25^\circ \times 0.25^\circ$ and 3 h, respectively.

and *rated output* for an extended period, usually one year. Its value is dimensionless ranging between 0 (no electricity output) and 1 (persistent full capacity output) or in percentage form (0-100%), as we adopted here. Wind speeds s_{100} transformed by Eq. 6.3 to mean capacity factors presented in Fig. 6.3a. This figure reveals that onshore nominal capacity factors are larger than 40-45% and expected particularly over the central region of Algeria (roughly Tademaït plateau in the north of In-Salah and the east of Adrar province), the land region of the highest mean wind speeds; while the low wind belt in Morocco characterized by the minimal capacity factors (see also Figs. 6.1a,b). The value is less than 1% in the region of Al Haouz, particularly around 31.25°N (lat), 8.0°W (lon).

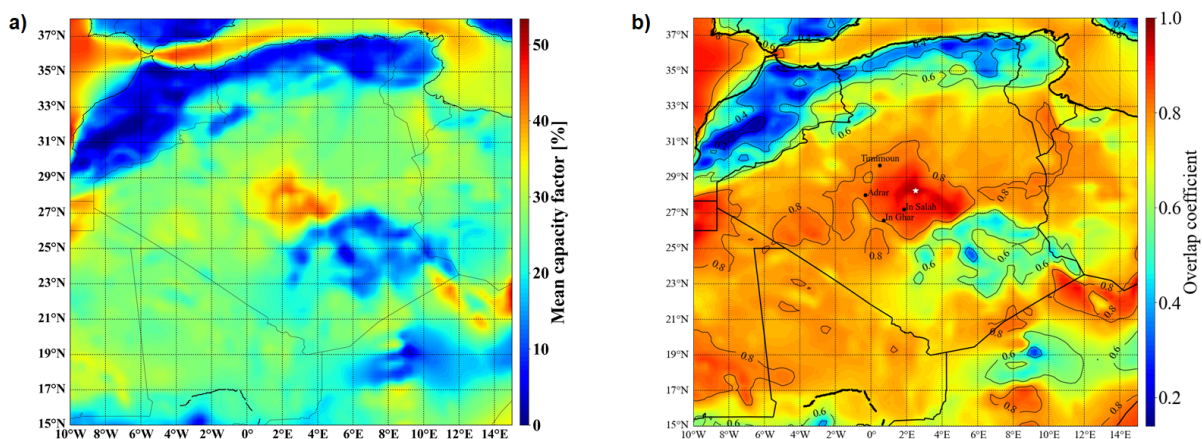


Figure 6.3: (a) Geographic distribution of the mean capacity factor (percentage values). (b) Geographic distribution of the overlap coefficient between the target location (white symbol) and all the other grid cells. Target location 28.25°N , 2.5°E . The evaluated period is 01/01/2011-09/30/2018 with a temporal resolution of 3h.

The practically windless area is located north-west behind the Atlas Mountains. (Notably, Morocco has a much larger off-shore than on-shore wind energy potential [181].) The situation is similar over the densely populated coastal regions in Algeria, unfortunately the low expected capacity factors question any reasonable installation of wind turbines.

A comparison of wind distributions between the location of the highest mean wind speed in Tademaït plateau (28.25°N, 2.5°E) is given by the *Overlap coefficient* Eq. (6.5) (see Refs. [182, 183]) for each grid cell is illustrated in Fig. 6.3b. The overlap coefficient is defined by the intersection area of two wind histograms over a period of almost 8 years (01/01/2011-30/09/2018) at the height of 100 m as

$$OVL_{0,i} = \int \min\{f_0(s_{100}), f_i(s_{100})\}d(s_{100}) , \quad (6.5)$$

where $f_0(s_{100})$ and $f_i(s_{100})$ are the empirical probability densities in fixed bins of width $d(s_{100}) = 1/6 \text{ ms}^{-1}$ for sites 0 (white symbol in Fig. 6.3b) and i . We see that low overlap coefficients coincide with the areas of low mean wind speed and vice versa, except the regions (mostly over seas) where the mean wind speed is higher than in the target cell. Fig. 6.3b shows that the wind speed distribution over Tademaït plateau area strongly overlapping ($OVL > 0.9$), surrounded by the region that is confined by the cities (Adrar, Timimun, In-Ghar) around In-Salah province ($OVL > 0.8$).

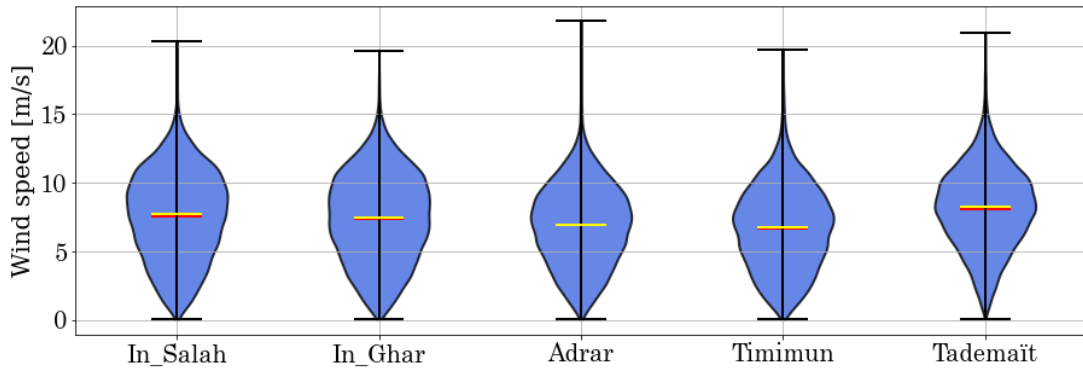


Figure 6.4: **Violin plots of wind speed distribution at five locations.** Red, yellow, and black lines represent mean, median, and the limit values respectively.

Fig. 6.4 illustrates five highly similar empirical probability distributions in the previously aforementioned area represented by violin plots. The wind speed in the region tends to be more normally distributed where the violin plot is approximately symmetric and peaked around the mean. Outliers greater than 15 ms^{-1} rarely occur up to $20\text{-}22 \text{ ms}^{-1}$, that is even turbines with a cut-out speed only about 20 ms^{-1} (typical minimum cut-out speed for turbines in the market) are expected to function steadily in this region.

6.3.2 Spatial correlations of wind speeds

Aggregation of electric output of several turbines over a given area (wind farm) is a common tool to increase total capacity factors and improve the quality of the output (decrease the variability). The quality of an aggregated output can be dramatically improved when the output of wind farms located on sites of strong negative correlations (anti-correlations) are integrated. By means of Eq. (6.1) described in Subsection 6.2.1, we estimated the Pearson correlation coefficient R between the time series of a specific target location and all the 93×101 grid points in order to see the potential of such possible spatial arrangement.

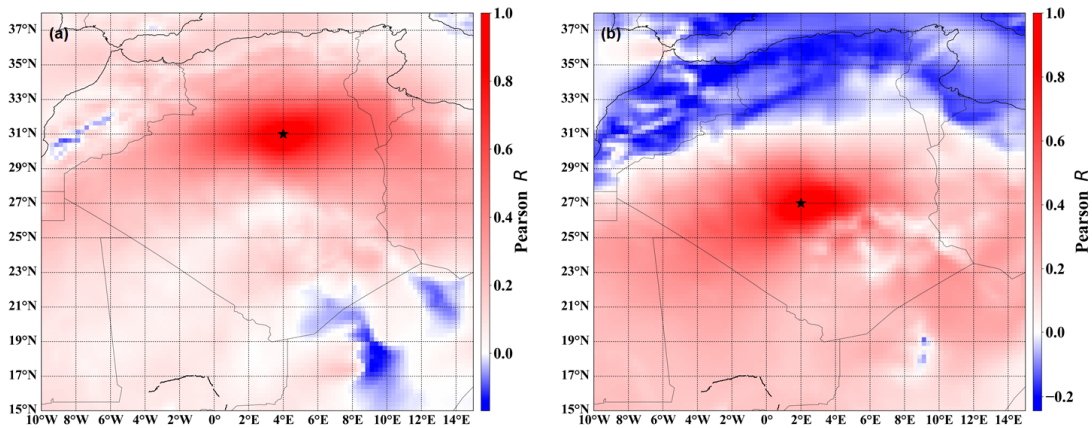


Figure 6.5: **Geographic distribution of the Pearson correlation coefficient R between the target location (black symbol) and all the other grid cells.** 100 m wind speed records are evaluated in the interval 01/01/2011 - 09/30/2018. (a) Target location 31°N, 4°E (~ 120 km north-east from the oasis town El Menia, Algeria); (b) 27°N, 2°E (~ 14 km south-east from the town In-Ghar, Algeria). Note that the color scales are strongly asymmetric.

Examples are shown in Figs. 6.5a,b for two Saharan locations (further locations are exhibited in Figs. 6.7a & Figs. 6.6a). All maps demonstrate that spatial correlations are very strong in vast geographic areas in each case ($R \approx 1$) and gradually decay over long distances. The patterns are rather complex, therefore the usual characterization by a single correlation length (assuming an exponential decay) would be an oversimplification (see Ref. [184] and references therein).

Over the Saharan region, as shown in Fig. 6.5a, the spatial correlations ($R \approx 1$) extend at least $\pm 4^\circ$ (± 380 km) in the zonal direction along 31°N latitude, while the meridional decay along 4°E longitude is faster ($\pm 2^\circ$, ± 222 km). Similar extension of strong positive correlations with the characteristic lengths at least $\pm 4^\circ$ (± 390 km) along latitude 27°N and ($\pm 2^\circ$, ± 230 km) along longitude 2°E in Fig. 6.5b, except that the pattern is

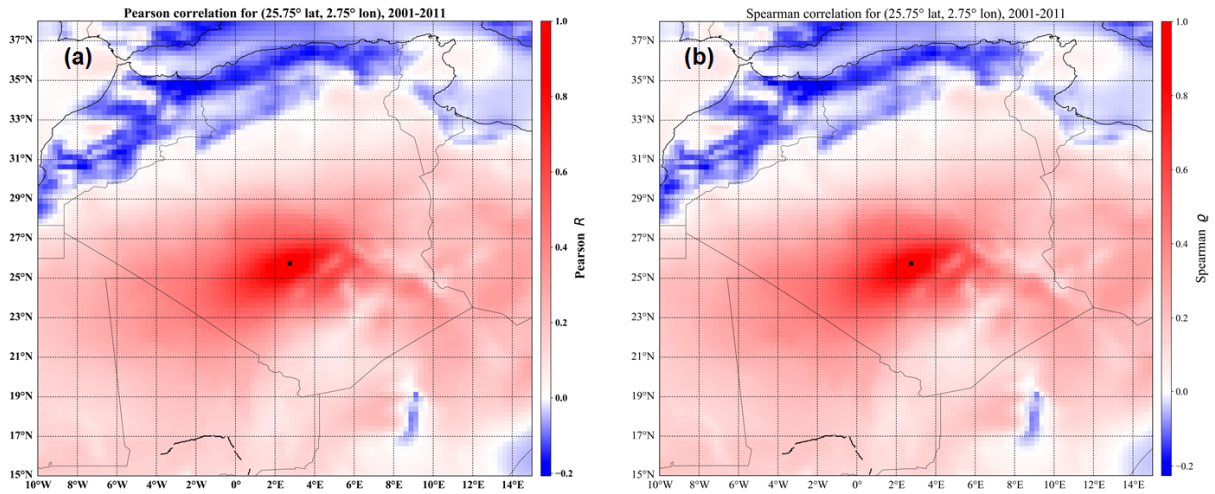


Figure 6.6: Geographic distribution of the (a) Pearson R and (b) Spearman ρ correlation coefficients between the target location (black symbol) and all the other grid cells. 100 m wind speed records are evaluated in the interval 01/01/2001-12/31/2010. Target location 25.75°N , 2.75°E (~ 70 km north-east from In-Salah, Algeria). Note that the color scales are strongly asymmetric. The patterns are almost identical, slightly lower negative values are in (b).

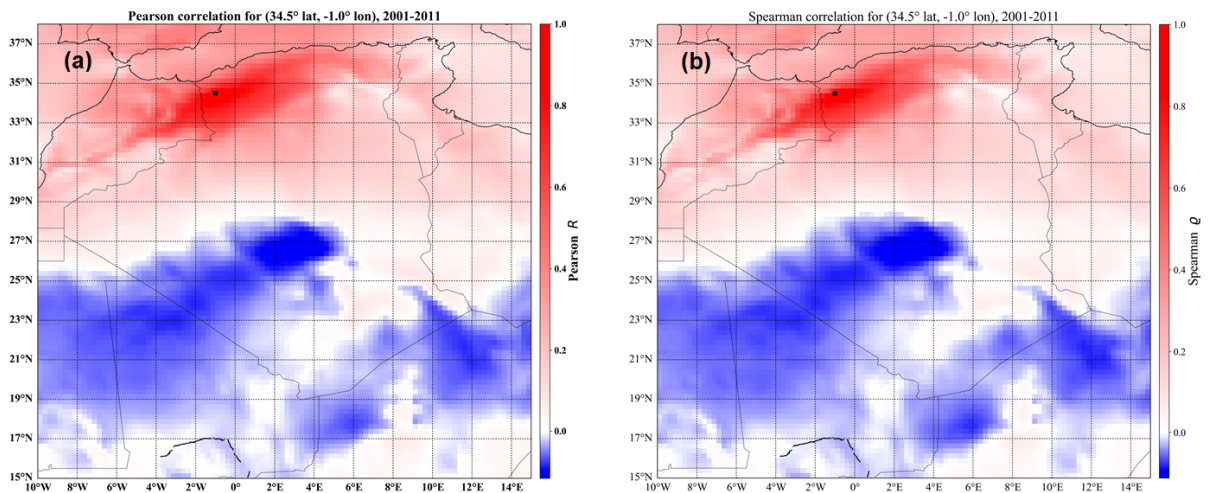


Figure 6.7: Geographic distribution of the (a) Pearson R and (b) Spearman ρ correlation coefficients between the target location (black symbol) and all the other grid cells. 100 m wind speed records are evaluated in the interval 01/01/2001-12/31/2010. Target location 34.5°N , 1°W (~ 16 km west from the town Ras El Ma, Algeria). Note that the color scales are strongly asymmetric.

asymmetric in the zonal direction. In Fig. 6.6a, the extension of strong correlations tend to be on the NE–SW and NW–SE directions for a distance at least $\pm 2^\circ$ (± 150 km). Another example in Figs. 6.7 for the north-west region of Algeria (34.5°N , 1°W) illustrates a strong correlation extending more than $\pm 2^\circ$ (± 283 km) along NE–SW axis tangential to Tell Atlas Mountains, and $\pm 1^\circ$ (± 146 km) in NW–SE axis. The above mentioned four figures illustrate general feature of spatial correlations for most grid-cells, weak anti-correlations appear for very large distances. The smallest negative correlation found is around $R = -0.25$ for a few locations. Generally, places of low wind and high wind regions are anti-correlated as in Fig. 6.5b. By inspecting a large number of such correlation maps, we can conclude that the exploitation of negative spatial correlations in an aggregated wind electricity production is not realistic over this geographic area.

Note that the consideration of Spearman rank correlation [Eq. 6.2] leads to the same conclusion, correlation maps are almost identical (Figures 6.6 a and b, and 6.7 a and b).

6.3.3 The correlations of wind speeds vs solar radiations

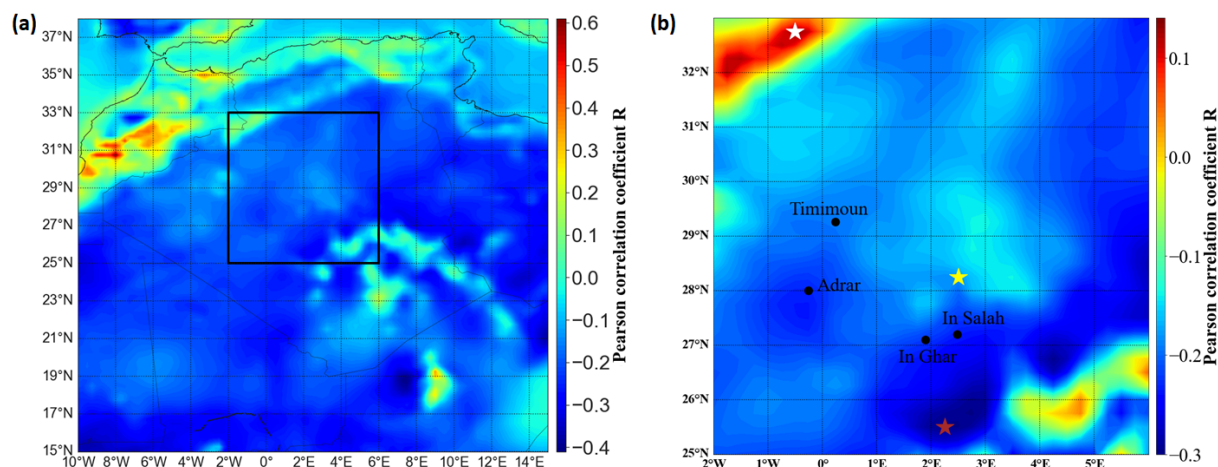


Figure 6.8: (a) **Geographic distribution of the Pearson correlation coefficient R between wind speed at 100 m and solar radiation in each grid cells.** Wind speed and incident solar radiation records evaluated in the interval 01/01/2011 - 09/30/2018 with a temporal resolution of 3 h. The black rectangle centered around In-Salah province, Sahara, is the location of enhanced analysis by a temporal resolution of 1 hour. (b) **Geographic distribution of the Pearson correlation coefficient R between wind speed at 100 m and solar radiation in each grid cells focused on the area indicated in (a).** Records are evaluated in the interval 01/01/2007 - 09/30/2018. Yellow, white and brown stars refer the points of the highest wind speed, highest R and lowest R , respectively. Note that the color scales are strongly asymmetric.

Despite the aggregation of wind electricity of negative spatial correlations is not an

option, the exploitation of negative temporal correlations of solar and wind electricity production might still be possible. After we estimated the Pearson correlation coefficient R between the time series of a wind speeds at 100 m s_{100} and surface solar radiation downward $ssrd$ in each geographic grid cell of all the 93×101 grid points (see the map in Fig. 6.8a), weak negative correlation coefficients appear in a large part of the map (blue area). The lowest negative value is $R \approx -0.4$, while it reaches a value ~ -0.3 in the region of Algeria, especially where wind speeds are high (28.25°N longitude 2.5°E in the region of In-Salah, see Fig. 6.8b specified by the black rectangle in Fig. 6.8a). Moderate positive correlations seem to be in windless zones over the high West Atlas mountains in Morocco (highest at 31.25°N , longitude 8°W), while northern coastline wind speeds and downward solar radiation are not correlated.

Wind speed temporal variations

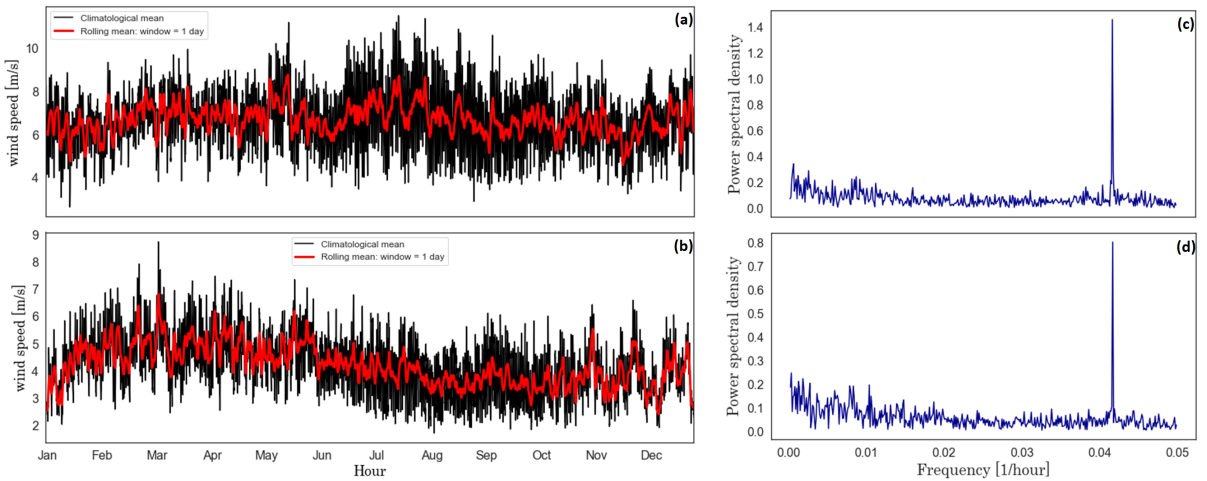


Figure 6.9: **Time series of climatological means (left) and their DFT (right).** The assessed period is between 01/01/2007 and 30/09/2018 for the grid cell (a) and (c) 25.5°N , 2.25°E and (b) and (d) 32.75°N , 0.5°W . Spatial and temporal resolutions are $0.25^\circ \times 0.25^\circ$ and 1 h.

In order to know the dominant frequencies of wind speed fluctuations at height of 100 m in the focus region (Fig. 6.8b), we estimated the *climatological means* which are exhibited by the time series in Figs. 6.9a,b. It is obtained by averaging hourly wind speeds over almost 12 years. The target geographic coordinates in Fig. 6.9a and b are 25.5°N , 2.25°E with the lowest cross-correlation coefficient of $R \approx -0.3$, and the other is at 32.75°N , 0.5°W with the highest value of $R \approx 0.12$. Both *power spectral densities* (see Fig. 6.9c,d) show that the wind speeds at 100 m in the period of 12 years between 2007

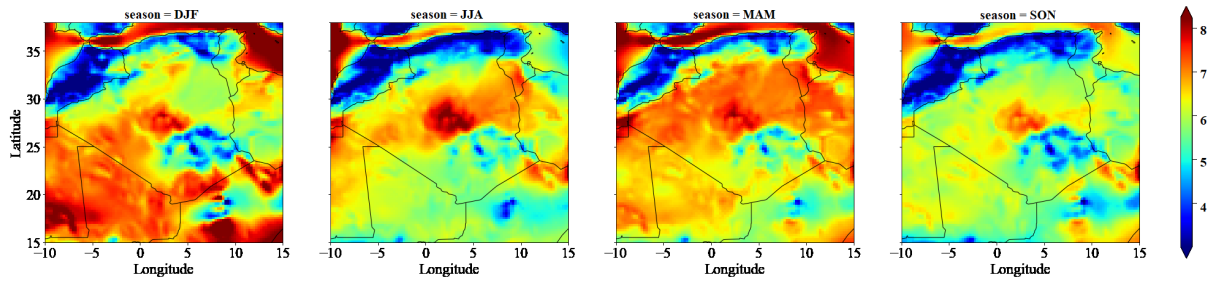


Figure 6.10: **Geographic distribution of seasonal mean wind speeds at 100 m over a period of 9 years (01/09/2011 - 30/09/2018)**. Spatial and temporal resolutions are $0.25^\circ \times 0.25^\circ$ and 3 h. Symmetric color scales.

and 2018 are characterised by a quasi-stable daily frequency of $f \approx 0.041 \text{ h}^{-1}$. For the case of considered locations in Fig. 6.4, similar power spectral densities were found.

Figs. 6.9a,c clearly illustrate that the typical climatological mean has a weak seasonal dependence, which is common in tropical climate. Nevertheless the daily variability visibly increases during the summer and early autumn periods, while the rest of the year exhibits weaker fluctuations around the mean. Fig. 6.10 confirms that the wind speeds at 100 m moderately change over seasons in the mid-Sahara (around In-Salah), the weakest are in autumn *SON* (September, October, November). Even though the mean wind speeds

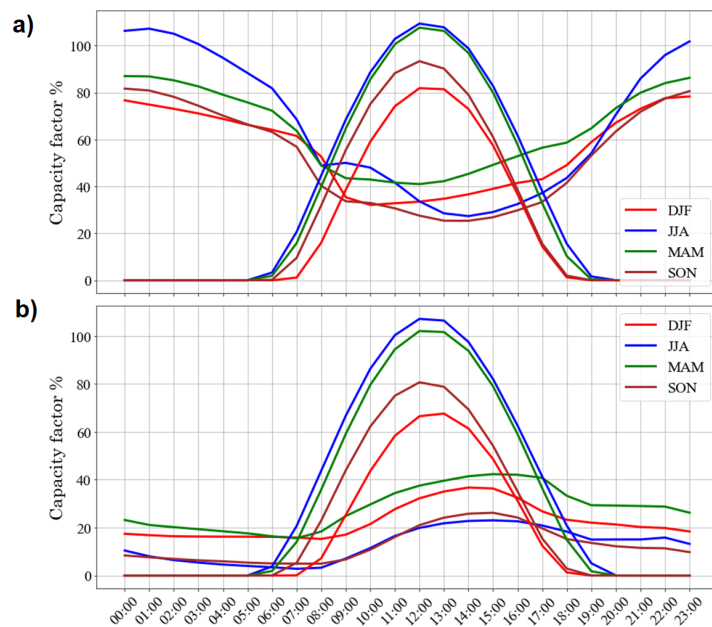


Figure 6.11: **Hourly mean wind and solar capacity factors in each season (a) at the geographic cell 25.5°N , 2.25°E , (b) at 32.75°N , 0.5°W** . Period of four years (01/01/2007 - 30/09/2018) with temporal resolution of 1h. Note that wind capacity factors are multiplied by 2 for a better visualization.

during a calendar year is the highest over the open sea areas, the mid-Sahara shows higher mean 100 m wind speeds in summer *JJA* and autumn *SON* than over the Mediterranean Sea.

A general insight to the trends of wind and solar energy production during a day is provided by the mean hourly capacity factors of wind and tilted solar panel for each season, separately. The results are plotted in Fig. 6.11a,b for two geographic locations (see caption Fig. 6.11). It reveals that the wind electric energy production of the night time can be much higher (up to 53.6% for the summer season at 01:00 UTC) than during the day (around 13.7% for the same season at 14:00 UTC). Our example location of a weak positive correlation exhibit a maximum wind energy during the day (21.2% in spring season at 15:00 UTC) and the minimum during the night (1.4% in summer at 7:00 UTC).

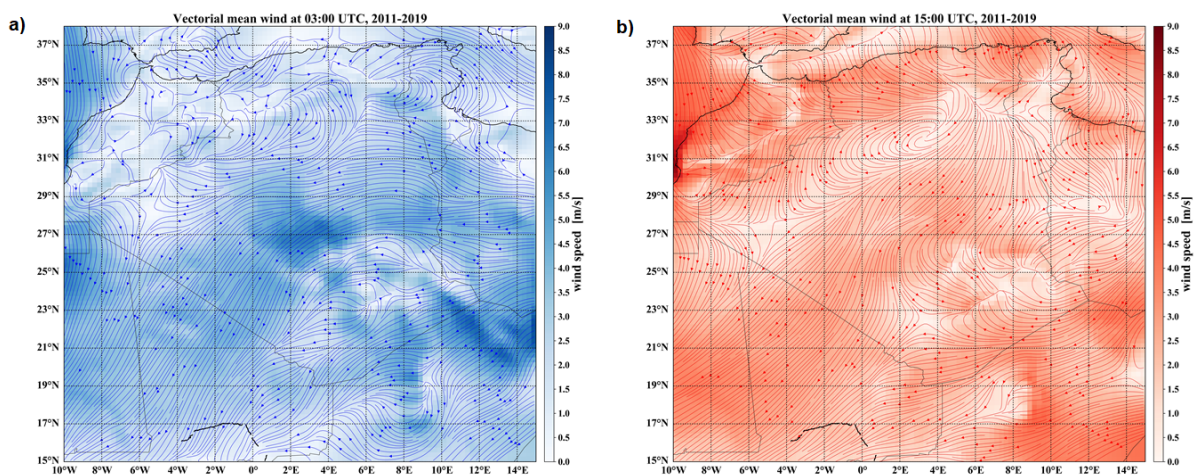


Figure 6.12: **Vectorial mean values of 100 m wind velocities between 2011-2019 from the ERA5 reanalysis data bank.** Spatial and temporal resolutions are $0.25^\circ \times 0.25^\circ$ and 3 h. The streamlines characterize mean flow directions, color scales denote magnitudes. (a) Nighttime vectorial mean values calculated for the interval 00:00-03:00 UTC for each day over the 9 years. (b) The same as (a) for a daytime interval (12:00-15:00 UTC).

Fig. 6.12a illustrates a nighttime (at 03:00 UTC), while Fig. 6.12b a daytime (at 15:00 UTC) mean flow field, where vectorial mean of 100 m wind velocities are calculated and visualized. Indeed, the flow fields exhibit very large westward coherent structures over very large distances, particularly at night over the Sahara. Such wind velocity patterns are strongly related to the continental scale westward and northward dust transport [185], [186]. It is different from the Atlas region where the mean wind fields indicate stronger turbulence. Similarly, the daytime mean wind fields are markedly different over the Atlas and the Sahara.

6.3.4 Combined wind-solar electricity production

An obvious renewable resource in desert areas is photovoltaic electricity generation. We evaluated the possible role of *ssrd* (surface solar radiation downward) in an energy portfolio. Particularly, we analysed the potential of aggregated wind-solar electricity production over the middle of Saharan region in Algeria (the area encompassed by black rectangle in Fig. 6.8a), where the expected capacity factors for wind electricity generation are the highest (Fig. 6.3a).

The simple model construction described in Subsection 6.2.3 is an upper limit, losses and other disturbing factors (warming of solar cells, dust cover, etc.) are not considered here. The linear combination of the two terms given by Eq. (6.4) means that the total

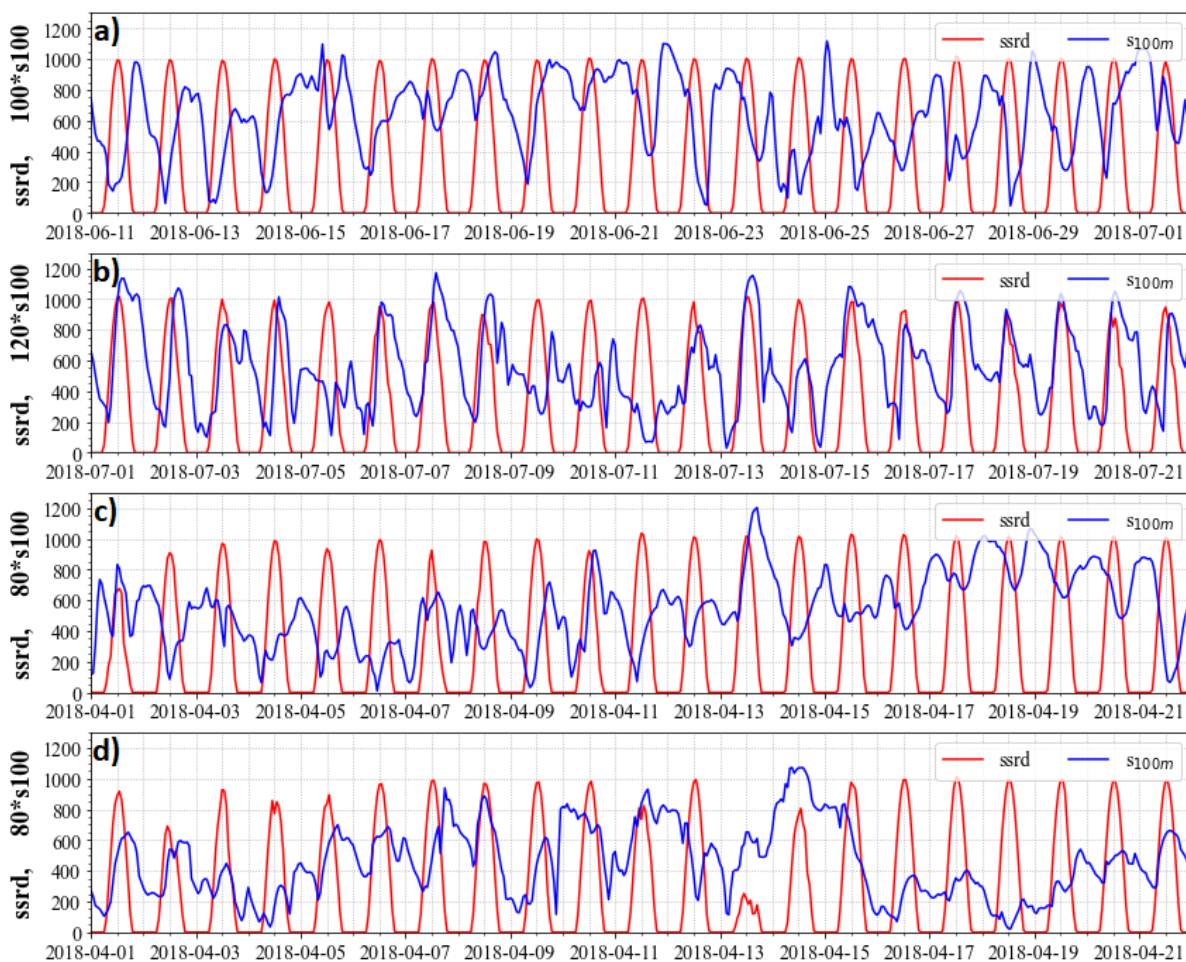


Figure 6.13: Time series of downward solar radiation flux at the surface (in units of Wm^{-2}) and 100 m wind speed (ms^{-1}) multiplied by 80, 100, or 120 for the sake of visualization. (3 weeks period in each plot). Location 25.5°N , 2.25°E , (a) June 2018 and (c) April 2018. At 32.75°N , 0.5°W , (b) July 2018 and (d) April 2018.

output integrated over a longer period is a linear function of the resource fraction c , where the slope is determined by the capacity factors of pure wind and pure solar generation. When the former is larger, the slope of the line is negative, in the opposite case the slope is positive.

Figure 6.13 – see the details in the caption – elucidates four examples of hourly time series of wind speed at 100 m and surface solar radiation downward. They were chosen from the year 2018 in both aforementioned locations of negative and positive Pearson correlation coefficients between $ssrd$ and s_{100} . For the case of location 25.5°N , 2.25°E , Fig. 6.13a,c illustrate that the wind speed at 100 m intensifies during nighttime more frequently, especially in the summer period when the mean magnitude is more or less constant, while the spring season clearly shows larger magnitude shifts in a time scale of about two weeks. If the wind speed s_{100} is positively correlated with $ssrd$, an aggregation of the two energy sources cannot smooth electric output.

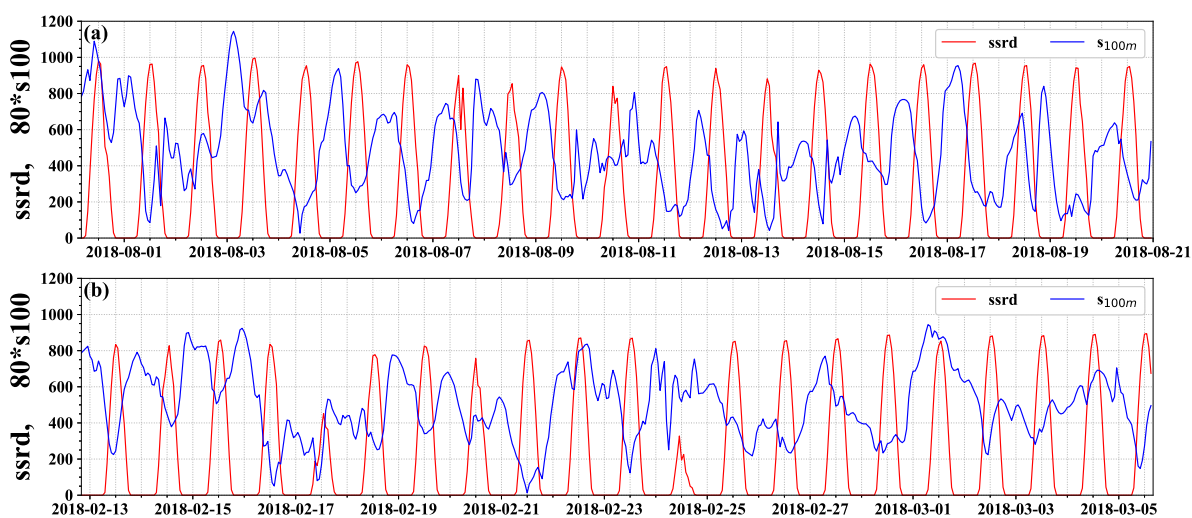


Figure 6.14: **Time series of downward solar radiation flux at the surface (in units of Wm^{-2}) and 100 m wind speed (ms^{-1}) multiplied by 80 for the sake of visualization.** 500-500 hours are plotted (about 3 weeks). (a) Location 27°N , 0° (10 km south-east from the town Sali, Algeria), August 2018; (b) 27°N , 2°E (14 km south-east from the town In-Ghar, Algeria), February 2018.

Negative values of the correlation coefficient R are moderate ($R > -0.3$) in a wide zone inside the mid-Algerian Sahara (blue color Fig. 6.8) where the wind speeds at 100 m are rather high in all seasons (check Fig. 6.10). The time series for two different locations (with $R \approx -0.21$) are illustrated in Figure 6.14 demonstrating that desert wind intensifies quiet often during the night periods. All examples shown are not cherry picking, this is the general tendency in this geographic region, and in every seasons. Moderate

correlation coefficients are the consequence of the very large standard deviation of $ssrd$ in the denominator of Eq. (6.1). Indeed, downward solar radiation varies each day between zero and 800-1000 Wm^{-2} , even in the northern edge of the region (33°N) is not less than 600 Wm^{-2} in the middle of the winter season.

When the main goal is to maximize renewable electricity production, the solution is simple: choose the resource which has the higher total capacity factor. The largest part of the Saharan region “solar-dominated”, therefore maximum production can be achieved by pure photovoltaic generation. The price is the strong oscillation: there is zero production during the nights. (Unfortunately, industrial scale renewable energy storage is not a option in Africa, because all known technology require very large investment capital [187]).

When the target of optimization is a smoother production, it is worth to consider the possible role of nighttime desert winds. One possible parameter to characterize the strength of fluctuations for a given time series is the *coefficient of variation* (CV) which is simply the ratio of *standard deviation* and the *long-time mean value*. We determined systematically CV as a function of resource fraction c [see Eq. (6.4)], and found that it has a unique minimum value (see Fig. 6.15a-inset) defining an optimal combination ratio c_{opt} with the smoothest possible output. Fig. 6.15a illustrates that this optimum is between 0.56 and 0.69 (P_{wind} proportion) depending on the particular location. At the optimal value of resource combination c_{opt} , the total output is obviously less than the maximum, therefore we determined the total capacity factor loss for each gridcell, which is the difference $[P_{tot}(c_{opt}) - P_{tot}(c_{max})]$. (Note that c_{max} is either 0 or 1 for solar-dominated or wind-dominated locations, see Eq. (6.4).) The result is shown in Fig. 6.15b. The large blue areas indicate that the capacity factor loss is only a few percent at the

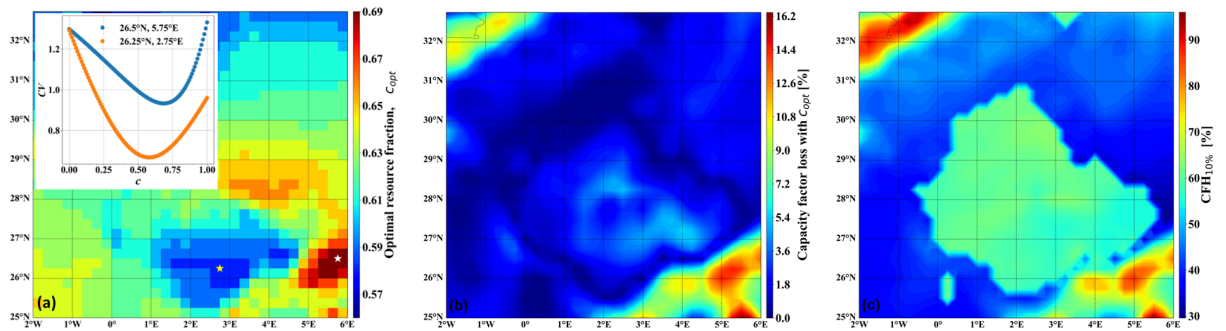


Figure 6.15: (a) **Geographic distribution of optimal resource fraction c_{opt} , where the coefficient of variation CV is minimal.** The inset illustrates the $CV(c)$ dependence for two sites: $26.5^\circ\text{N}, 5.75^\circ\text{E}$ (white star), and $26.25^\circ\text{N}, 2.75^\circ\text{E}$ (yellow star). (b) **Capacity factor loss with the optimal resource fraction c_{opt} relative to the maximum value.** (c) **The ratio $CFH_{10\%}$, its explanation is in the text.**

optimal resource combination c_{opt} for most locations.

The coefficient of variation CV shown in Fig. 6.15a-inset has very substantial drop at several places around c_{opt} , nevertheless one can demonstrate the improvement of the combined output power quality in more transparent ways. As an example, we determined the ratio of total time when the output is less than 10% at c_{opt} over the total time when the output is less than 10% at c_{max} , denoted by $CFH_{10\%}$ (*Capacity Factor Hiatus*). The geographic distribution of $CFH_{10\%}$ is shown in Fig. 6.15c. The blueish areas exhibit a dramatic improvement, the total time of low aggregated output at the optimal resource ratio c_{opt} is only 30-40% relative to the maximal output at c_{max} . The huge green island in the middle of the region unambiguously identifies the wind-dominated locations ($c_{max} = 1$), blue sites are solar-dominated ($c_{max} = 0$). The reason of the dampened improvement over wind-dominated areas ($CFH_{10\%} \approx 60\%$) is simply the fact that the wind speeds at 100 m almost never drop to zero. Still, the incorporation of solar electricity generation provides a much better quality aggregated output. Red areas ($CFH_{10\%} > 80\%$) indicate that there is negligible improvement of electric output quality, solar energy dominates there and wind speeds at 100 m are low during nighttime. The improvement over solar-dominated locations (blue in Fig. 6.15c) is more pronounced because any inclusion of nighttime wind electricity production immediately shortens the periods of zero output.

6.4 Discussion

Previous assessments of wind energy potential over Algeria have been mostly based on surface measurements of meteorological stations or reanalysis wind fields at 10 m standard height and common extrapolation methodologies to estimate wind strengths at assumed hub-heights of 80-100 m. The list of most relevant studies and their key features are the following: Merzouk [188], 10 years, 64 weather stations, annual wind map; Djamaï and Merzouk [189] wind farm potential at around Ardar, 5 years of WAsP data; Stambouli *et al* [190], overview of Algeria's whole energy sector, particular emphasize on renewable resource potentials; Boudia *et al* [191], 5 years, 87 weather stations, wind maps at 10 m height; Daaou Nedjari *et al* [192], 10 years, 95 weather stations, probability distributions, wind maps for 10 m and 80 m; Boudia and Santos [193], 33 years of ERA Interim data, validation by 42 ground stations for 2014, probability distributions, regional wind resource maps; Ounis and Aries [194], 17 years of ERA Interim data, evaluation of various probability distributions; most recently Guezgouz *et al* [160], solar and wind energy complementarity in Algeria for the year 2019 with 1 h temporal resolution, wind data from MERRA-2 reanalysis (10 m, extrapolated), insolation data from CAMS reanalysis.

The wind maps are similar to our Fig. 6.1a, however maximum mean values are shifted somewhat westward, around Adrar (27.87°N, 0.28°W). The wind maps by Nedjari *et al* in Ref. [192] (Fig. 3 for 10 m and Fig. 5 for 80 m) and Guezgouz *et al* [160] exhibit a good agreement with ours, with the windiest places centered around In-Salah (27.18°N, 2.48°E).

All the above listed studies are based on wind fields at the 10 m standard height, and extrapolations are used for higher altitudes. However, extrapolation of 10 m wind speeds to 100 m by e.g., the usual power law approximation may result in erroneous results. A particularly spectacular example is presented in Supplementary Fig. 2 by Sterl *et al* [156]. The mean daily cycle of surface wind (thus the extrapolated speed too) exhibits an enhancement during the daylight periods, nevertheless ERA5 100 m wind speeds have the very opposite tendency of an enhancement during the nights.

As for the recent resource compatibility study by Guezgouz *et al*, they also use reanalysis data (MERRA-2 and CAMS) of high temporal resolution for the year of 2019. The spatial resolution is somewhat lower ($0.5^\circ \times 0.5^\circ$), and 10 m wind speeds are extrapolated by the common power law with the exponent of $1/7$. They do not investigate energy mix in the study, the Spearman correlation coefficient Eq. (6.2) is used as a complementarity index. Still, they found similar daily anti-correlations between solar and wind resources at around the same locations as we obtained.

We think that our simple model framework of electricity integration scheme by Eq. (6.4), the characterization of the output quality by the coefficient of variation (CV) and by the capacity factor loss at an optimal combination ratio (Fig. 6.15b) or the capacity factor hiatus ($CFH_{10\%}$, Fig. 6.15c) provide a quick and transparent methodology to identify suitable geographic locations, where installation of combined wind and solar electricity systems are promising.

Combining several energy sources in electricity generation under an *Integrated Renewable Energy System* increases our options to satisfy the human need of daily energy usage in eco-friendly ways without high dependence on fossil fuels, or large storage capacity. Since we do not expect other available sources in the region considered than wind and solar capacities, we suggest to integrate electric outputs of the locally abundant energy resources. Such integration seems to be feasible without an extended grid, relying on local scale aggregation.

Chapter 7

General conclusion

Our experimental research projects aimed to investigate wave phenomena in the marine environment which is characterized by quasi-two-layer stratified water. Such properties are found in Scandinavian fjords, namely the Gullmar fjord, where the stratification effect is strongly manifested. This environment is characterized by a top layer of brackish water inflow from Skagerrak coastal waters that is affected by glacier runoff and Kattegat outflow. In contrast, the bottom layer is almost stagnant and contains rarely renovated salty water. As a result, there exists a relatively strong pycnocline between them [25, 142]. We mainly examined the amplification of interfacial waves through vertical energy conversion as well as their source and mechanism in small scale processes with rectangular wavetanks. We obtained our results based on the measured and calculated physical parameters: amplitude A , wavelength λ , velocity U , frequency ω . Thus, we could test the observed dispersion relation and compare it to the linear dispersion relation of the interfacial internal wave. Our research on the concerned type of stratification was divided in two projects.

I. Laboratory modelling to the dead water phenomenon was conducted through establishing 11 density profile series, towing a ship toy on a surface of two-layer stratification, with each pull characterized by a constant velocity U . Our finding is summarized as follows:

- When the ship moves on a two-layer stratified water, part of its kinetic energy is converted to sequential interfacial internal waves with pronounced amplitudes comparable to the layer thickness, propagating with an equivalent phase velocity. The ship was towed with a constant velocity rather than a constant force. We found that the generated waves resonate at a critical velocity $U^* \approx 0.8c_0^{(2)}$ ($c_0^{(2)}$ is the two-layer long wave velocity) and exhibit different behaviors for sub- and supercritical

wavelengths which depend on the vertical density profile of the stratification. The scaled critical flow velocity under the ship bow in the upper layer was found to be $U_f^* \approx c_0^{(2)}$.

- Despite that the large amplitude of the generated interfacial wave is featured in the dead water phenomenon, and the fact that nonlinear waves can only be described by means of nonlinear theory [91, 94], the linear theory surprisingly performs fairly well and could give an adequate description to the relationship between the wave phase velocity and its wavenumber.
- The linear three-layer approximation (Eq. 2.30) by Fructus and Grue [99] of the freely propagating wave predicted the phase velocity $c^{(3)}$ of the wave that is characterized by subcritical wavenumber k at $U \lesssim 0.8c_0^{(2)}$. However, the supercritical wavenumber at $U \gtrsim 0.8c_0^{(2)}$ is set by a fixed effective buoyancy frequency ($N_{eff} \approx 0.48.N_2$) linearly related to the buoyancy frequency of the pycnocline N_2 . Then the coalescence of these two fundamental wave motions indicates the maximum amplification of interfacial internal waves in the dead water phenomenon.

II. We performed laboratory modelling to the effect of bottom topography and stratification on the damping of seiche modes m ($m=1, 2, 3, 4, 6$), and the interfacial internal wave amplification by the barotropic to baroclinic energy conversion in two-layer stratified medium within fjords system. This was done at the presence of bottom sill and a control series where it was absent. Our finding is constituted in two types of internal waves, which were generated at the interface through the energy conversion from surface seiche -- from sloshing motion to the surface -- that lead to its damping:

- The short wave with period of surface seiche is excited by the horizontal flow above the obstacle, and its amplitude is at maximum when a seiche node is exactly above the obstacle. However, it is absent if the the obstacle's location coincides with anti-node of the seiche (in the case of one dominant surface frequency) which makes the odd seiche modes decay faster -- when the obstacle is situated in the middle of the basin -- for the same stratification. Large period internal seiche resonates with wavelength fit integer number to the wavetank length which exists either in the presence or absence of the bottom obstacle.
- Although the surface seiche exhibits nonlinear behavior (considerable amplitude), the dispersion relation of the linear wave theory -- for waves in homogeneous water -- worked fairly well on the tested damping mode frequencies, which were observed

on surface of stratified water. Likewise, the linear internal wave dispersion relation indeed describes the pattern that the observed interfacial internal waves follow (generated through the energy conversion from the aforementioned modes). It describes baroclinic waves generated in the real quasi-two-layer sill fjords quite well in cases where the surface forcing frequencies are large. While the three-layer correction for such system within the range of large wavenumbers is negligible.

As a secondary project for the thesis, we statistically evaluated the complementarity of wind-solar energy resources for electricity production over north-western Africa – the region with extreme dependence on fossil fuels – including the Mediterranean sea, with a focus centered around Algeria, particularly In-Salah region. We analyzed ERA5 reanalysis data of high spatial (latitude: $0.25^\circ \times$ longitude: 0.25°) and temporal resolutions (3h, and 1h for In-Salah) of wind speeds at altitude of 10m (s_{10m}) and 100m (s_{100m}), and downward solar radiation flux *ssrd*. We aimed to explore the suitability and to identify the optimal location of integrating wind and photo-voltaic electricity production. Our findings are summarized as follows:

- Wind speeds at 100 m over the Sahara are comparable to those over the open sea with maximum mean speed at Tademaït plateau In-Salah, and unexpectedly higher speeds in Summer (JJA) Autumn (SON) seasons than Mediterranean sea. In contrast, we observed low wind speeds along Tell Atlas, Saharan Atlas in the north and Tassili n’Ajjer in the south.
- We found the existence of utilisable daily anti-correlations between local wind speeds at altitude of 100m and solar radiations over the Sahara.
- In addition to the fact that the Algerian Sahara exhibits a high potential of wind speeds at altitude of 100m and solar radiations, the linear model for electricity output aggregation from the wind and solar resources (by Eq. 6.4) suggests that the optimal resource combinations in this region for smooth electricity output is between 60-40% and 70-30% (wind-solar), and low capacity factor loss to the maximum electricity output (pure wind $c_{max} = 1$ or pure solar $c_{max} = 0$) between 0% and 5% in a large area in either wind dominated or solar dominated resources.

Bibliography

- [1] Z. Zhongming, L. Linong, Y. Xiaona, Z. Wangqiang, L. Wei, *et al.*, “Ar6 climate change 2021: The physical science basis,” 2021.
- [2] O. Edenhofer, R. Pichs-Madruga, Y. Sokona, K. Seyboth, P. Matschoss, S. Kadner, T. Zwickel, P. Eickemeier, G. Hansen, S. Schlömer, *et al.*, “Ipcc special report on renewable energy sources and climate change mitigation,” *Prepared By Working Group III of the Intergovernmental Panel on Climate Change, Cambridge University Press, Cambridge, UK*, 2011.
- [3] J. A. Scales and R. Snieder, “What is a wave?,” *Nature*, vol. 401, pp. 739–740, 10 1999.
- [4] W. Alpers, P. Brandt, and A. Rubino, “Internal waves generated in the straits of gibraltar and messina: Observations from space,” *Remote Sensing of the European Seas*, pp. 319–330, 2008.
- [5] R. F. Ivanovic, P. J. Valdes, R. Flecker, L. J. Gregoire, and M. Gutjahr, “The parameterisation of mediterranean–atlantic water exchange in the hadley centre model hadcm3, and its effect on modelled north atlantic climate,” *Ocean Modelling*, vol. 62, pp. 11–16, 02 2013.
- [6] E. G. Morozov, K. Trulsen, M. G. Velarde, and V. I. Vlasenko, “Internal tides in the strait of gibraltar,” *Journal of Physical Oceanography*, vol. 32, pp. 3193–3206, 11 2002.
- [7] M. BRUNO, R. MAÑANES, J. J. ALONSO, A. IZQUIERDO, L. TEJEDOR, and B. A. KAGAN, “Vertical structure of the semidiurnal tidal currents at camarinal sill, the strait of gibraltar,” *Oceanologica Acta*, vol. 23, pp. 15–24, 01 2000.
- [8] J. J. del Rosario, M. B. Mejías, and A. Vázquez-López-Escobar, “The influence of tidal hydrodynamic conditions on the generation of lee waves at the main sill of

- the strait of gibraltar,” *Deep Sea Research Part I: Oceanographic Research Papers*, vol. 50, pp. 1005–1021, 08 2003.
- [9] L. St. Laurent and C. Garrett, “The role of internal tides in mixing the deep ocean,” *Journal of Physical Oceanography*, vol. 32, pp. 2882–2899, 10 2002.
- [10] W. Alpers, “Theory of radar imaging of internal waves,” *Nature*, vol. 314, pp. 245–247, 03 1985.
- [11] V. Klemas, “Remote sensing of ocean internal waves: An overview,” *Journal of Coastal Research*, vol. 282, pp. 540–546, 05 2012.
- [12] C. R. Jackson and J. Apel, “An atlas of internal solitary-like waves and their properties,” *Contract*, vol. 14, no. 03-C, p. 0176, 2004.
- [13] J. Nycander, “Generation of internal waves in the deep ocean by tides,” *Journal of Geophysical Research*, vol. 110, 2005.
- [14] F. Nansen, *The oceanography of the North polar basin*. Longmans, Green, And Co. ; Christiania, 1902.
- [15] N. Zeilon, *On tidal boundary-waves and related hydrodynamical problems*. Uppsala [U.A.] Almqvist & Wiksell, 1912.
- [16] N. Zeilon, *Experiments on boundary tides : a preliminary report*. Göteborg Elander, 1934.
- [17] F. Pétrélis, S. L. Smith, and W. R. Young, “Tidal conversion at a submarine ridge,” *Journal of Physical Oceanography*, vol. 36, pp. 1053–1071, 06 2006.
- [18] S. G. Llewellyn Smith and W. R. Young, “Conversion of the barotropic tide,” *Journal of Physical Oceanography*, vol. 32, pp. 1554–1566, 05 2002.
- [19] S. Falahat, J. Nycander, F. Roquet, A. M. Thurnherr, and T. Hibiya, “Comparison of calculated energy flux of internal tides with microstructure measurements,” *Tellus A: Dynamic Meteorology and Oceanography*, vol. 66, p. 23240, 10 2014.
- [20] R. D. Ray and D. E. Cartwright, “Estimates of internal tide energy fluxes from topex/poseidon altimetry: Central north pacific,” *Geophysical Research Letters*, vol. 28, pp. 1259–1262, 04 2001.

- [21] N. V. Zilberman, J. M. Becker, M. A. Merrifield, and G. S. Carter, “Model estimates of m2 internal tide generation over mid-atlantic ridge topography,” *Journal of Physical Oceanography*, vol. 39, pp. 2635–2651, 10 2009.
- [22] P. E. Renaud, M. Włodarska-Kowalczyk, H. Trannum, B. Holte, J. M. Węśławski, S. Cochrane, S. Dahle, and B. Gulliksen, “Multidecadal stability of benthic community structure in a high-arctic glacial fjord (van mijenfjord, spitsbergen),” *Polar Biology*, vol. 30, pp. 295–305, 08 2006.
- [23] M. W. Stacey, “Review of the partition of tidal energy in five canadian fjords,” *Journal of Coastal Research*, vol. 2005, p. 731, 07 2005.
- [24] A. Stigebrandt, “Barotropic and baroclinic response of a semi-enclosed basin to barotropic forcing from the sea,” *Fjord Oceanography*, pp. 141–164, 1980.
- [25] R. Parsmar and A. Stigebrandt, “Observed damping of barotropic seiches through baroclinic wave drag in the gullmar fjord,” *Journal of Physical Oceanography*, vol. 27, pp. 849–857, 06 1997.
- [26] J. R. Apel and D. T. Gjessing, “Internal wave measurements in a norwegian fjord using multifrequency radars,” *Johns Hopkins APL Technical Digest*, vol. 10, p. 295–306, 12 1989.
- [27] F. R. Cottier, F. Nilsen, R. Skogseth, V. Tverberg, J. Skarðhamar, and H. Svendsen, “Arctic fjords: a review of the oceanographic environment and dominant physical processes,” *Geological Society, London, Special Publications*, vol. 344, pp. 35–50, 2010.
- [28] B. Boehrer and M. Schultze, “Stratification of lakes,” *Reviews of Geophysics*, vol. 46, 05 2008.
- [29] W. D. Williams and J. E. Sherwood, “Definition and measurement of salinity in salt lakes,” *International Journal of Salt Lake Research*, vol. 3, pp. 53–63, 03 1994.
- [30] N. Skliris, R. Marsh, S. A. Josey, S. A. Good, C. Liu, and R. P. Allan, “Salinity changes in the world ocean since 1950 in relation to changing surface freshwater fluxes,” *Climate Dynamics*, vol. 43, pp. 709–736, 04 2014.
- [31] N. Skliris, R. Marsh, J. V. Mecking, and J. D. Zika, “Changing water cycle and freshwater transports in the atlantic ocean in observations and cmip5 models,” *Climate Dynamics*, vol. 54, pp. 4971–4989, 05 2020.

- [32] D. W. Kirkland, J. P. Bradbury, and W. E. Dean, “The heliothermic lake: a direct method of collecting and storing solar energy,” *Open-File Report*, 1980.
- [33] R. A. Plumb, *Atmosphere, ocean and climate dynamics*. Academic, 2007.
- [34] M. Lappa, *Thermal convection : patterns, evolution and stability*. Wiley, 2009.
- [35] G. Ingram Taylor, “Effect of variation in density on the stability of superposed streams of fluid,” *Proceedings of the Royal Society of London. Series A, Containing Papers of a Mathematical and Physical Character*, vol. 132, pp. 499–523, 08 1931.
- [36] J. W. Miles, “On the stability of heterogeneous shear flows,” *Journal of Fluid Mechanics*, vol. 10, p. 496, 06 1961.
- [37] T. Andow, K. Hanawa, and Y. Toba, “Experimental study on internal waves in a stratified shear flow,” *Journal of the Oceanographical Society of Japan*, vol. 37, pp. 179–192, 11 1981.
- [38] M. Nikurashin, R. Ferrari, N. Grisouard, and K. Polzin, “The impact of finite-amplitude bottom topography on internal wave generation in the southern ocean,” *Journal of Physical Oceanography*, vol. 44, pp. 2938–2950, 11 2014.
- [39] J. da Silva, M. Buijsman, and J. Magalhaes, “Internal waves on the upstream side of a large sill of the mascarene ridge: a comprehensive view of their generation mechanisms and evolution,” *Deep Sea Research Part I: Oceanographic Research Papers*, vol. 99, pp. 87–104, 05 2015.
- [40] M. Münnich, “The influence of bottom topography on internal seiches in stratified media,” *Dynamics of Atmospheres and Oceans*, vol. 23, pp. 257–266, 01 1996.
- [41] J. Xing and A. M. Davies, “Influence of multiple sills upon internal wave generation and the implications for mixing,” *Geophysical Research Letters*, vol. 36, 07 2009.
- [42] J. Boschan, M. Vincze, I. M. Jánosi, and T. Tél, “Nonlinear resonance in barotropic-baroclinic transfer generated by bottom sills,” *Physics of Fluids*, vol. 24, p. 046601, 04 2012.
- [43] M. Johnsson, J. A. M. Green, and A. Stigebrandt, “Baroclinic wave drag from two closely spaced sills in a narrow fjord as inferred from basin water mixing,” *Journal of Geophysical Research*, vol. 112, 11 2007.

- [44] C. Wunsch and R. Ferrari, “Vertical mixing, energy, and the general circulation of the oceans,” *Annual Review of Fluid Mechanics*, vol. 36, pp. 281–314, 01 2004.
- [45] C. Garrett, “Internal tides and ocean mixing,” *science*, vol. 301, p. 1858–1859, 2003.
- [46] M.-P. Lelong and E. Kunze, “Can barotropic tide–eddy interactions excite internal waves?,” *Journal of Fluid Mechanics*, vol. 721, pp. 1–27, 03 2013.
- [47] E. G. Morozov, *Oceanic Internal Tides: Observations, Analysis and Modeling*. Springer International Publishing, 2018.
- [48] C. Vic, A. C. Naveira Garabato, J. A. M. Green, A. F. Waterhouse, Z. Zhao, A. Melet, C. de Lavergne, M. C. Buijsman, and G. R. Stephenson, “Deep-ocean mixing driven by small-scale internal tides,” *Nature Communications*, vol. 10, 05 2019.
- [49] S. J. Hawkins, A. L. Allcock, A. E. Bates, L. B. Firth, I. P. Smith, S. Swearer, A. Evans, P. Todd, B. Russell, and C. McQuaid, *Tides, the Moon and the kaleidoscope of ocean mixing*, in: *Oceanography and Marine Biology: An Annual Review, Volume 58*. CRC Press, 11 2020.
- [50] E. V. Stanev and M. Ricker, “Interactions between barotropic tides and mesoscale processes in deep ocean and shelf regions,” *Ocean Dynamics*, vol. 70, pp. 713–728, 03 2020.
- [51] M. Rattray, “On the coastal generation of internal tides,” *Tellus*, vol. 12, pp. 54–62, 02 1960.
- [52] P. P. Niiler, “On the internal tidal motions in the florida straits,” *Deep Sea Research and Oceanographic Abstracts*, vol. 15, pp. 113–123, 02 1968.
- [53] T. H. Bell, “Topographically generated internal waves in the open ocean,” *Journal of Geophysical Research*, vol. 80, pp. 320–327, 01 1975.
- [54] A. Stigebrandt and J. Aure, “Vertical mixing in basin waters of fjords,” *Journal of Physical Oceanography*, vol. 19, pp. 917–926, 07 1989.
- [55] D. C. Chapman and G. S. Giese, “A model for the generation of coastal seiches by deep-sea internal waves,” *Journal of Physical Oceanography*, vol. 20, pp. 1459–1467, 09 1990.

- [56] A. Stigebrandt, “Resistance to barotropic tidal flow in straits by baroclinic wave drag,” *Journal of Physical Oceanography*, vol. 29, pp. 191–197, 02 1999.
- [57] J. P. Antenucci and J. Imberger, “Energetics of long internal gravity waves in large lakes,” *Limnology and Oceanography*, vol. 46, pp. 1760–1773, 11 2001.
- [58] J. P. Antenucci and J. Imberger, “The seasonal evolution of wind/internal wave resonance in lake kinneret,” *Limnology and Oceanography*, vol. 48, pp. 2055–2061, 09 2003.
- [59] M. Inall, F. Cottier, C. Griffiths, and T. Rippeth, “Sill dynamics and energy transformation in a jet fjord,” *Ocean Dynamics*, vol. 54, 07 2004.
- [60] B. Cushman-Roisin, A. J. Willmott, and N. R. Biggs, “Influence of stratification on decaying surface seiche modes,” *Continental Shelf Research*, vol. 25, pp. 227–242, 01 2005.
- [61] L. Boegman and G. N. Ivey, “The dynamics of internal wave resonance in periodically forced narrow basins,” *Journal of Geophysical Research: Oceans*, vol. 117, pp. n/a–n/a, 11 2012.
- [62] J. Park, J. MacMahan, W. V. Sweet, and K. Kotun, “Continuous seiche in bays and harbors,” *Ocean Science*, vol. 12, pp. 355–368, 03 2016.
- [63] A. Staalstrøm and L. P. Røed, “Vertical mixing and internal wave energy fluxes in a sill fjord,” *Journal of Marine Systems*, vol. 159, pp. 15–32, 07 2016.
- [64] M. I. Castillo, O. Pizarro, N. Ramírez, and M. Cáceres, “Seiche excitation in a highly stratified fjord of southern chile: the reloncaví fjord,” *Ocean Science*, vol. 13, pp. 145–160, 02 2017.
- [65] E. Roget, E. Khimchenko, F. Forcat, and P. Zavialov, “The internal seiche field in the changing south aral sea (2006–2013),” *Hydrology and Earth System Sciences*, vol. 21, pp. 1093–1105, 02 2017.
- [66] M.-A. Xue, O. Kargbo, and J. Zheng, “Seiche oscillations of layered fluids in a closed rectangular tank with wave damping mechanism,” *Ocean Engineering*, vol. 196, p. 106842, 01 2020.
- [67] A. Stigebrandt, “Vertical diffusion driven by internal waves in a sill fjord,” *Journal of Physical Oceanography*, vol. 6, pp. 486–495, 07 1976.

- [68] D. Chapman and G. Giese, “Seiches,” *Encyclopedia of Ocean Sciences*, pp. 344–350, 2001.
- [69] R. de Carvalho Bueno, T. Bleninger, H. Yao, and J. A. Rusak, “An empirical parametrization of internal seiche amplitude including secondary effects,” *Environmental Fluid Mechanics*, vol. 21, pp. 209–237, 09 2020.
- [70] A. M. Davies, J. Xing, and A. J. Willmott, “Influence of open boundary conditions and sill height upon seiche motion in a gulf,” *Ocean Dynamics*, vol. 59, pp. 863–879, 07 2009.
- [71] Z. Wynne, T. Reynolds, D. Bouffard, G. Schladow, and D. Wain, “A novel technique for experimental modal analysis of barotropic seiches for assessing lake energetics,” *Environmental Fluid Mechanics*, vol. 19, pp. 1527–1556, 03 2019.
- [72] A. Stigebrandt, “Baroclinic wave drag and barotropic to baroclinic energy transfer at sills as evidenced by tidal retardation, seiche damping and diapycnal mixing in fjords,” *Dynamics of Internal Gravity Waves*, vol. 11, pp. 73–82, 1999.
- [73] M. Vincze, P. Kozma, B. Gyüre, I. M. Jánosi, K. Gábor Szabó, and T. Tél, “Amplified internal pulsations on a stratified exchange flow excited by interaction between a thin sill and external seiche,” *Physics of Fluids*, vol. 19, p. 108108, 10 2007.
- [74] M. Vincze and T. Bozóki, “Experiments on barotropic–baroclinic conversion and the applicability of linear n-layer internal wave theories,” *Experiments in Fluids*, vol. 58, 09 2017.
- [75] M. Korosec, “Spectacular lee wave clouds across the adriatic sea on monday, feb 25th,” 02 2019.
- [76] G. A. Lawrence, “Steady flow over an obstacle,” *Journal of Hydraulic Engineering*, vol. 113, pp. 981–991, 08 1987.
- [77] C. J. Wright, R. B. Scott, P. Ailliot, and D. Furnival, “Lee wave generation rates in the deep ocean,” *Geophysical Research Letters*, vol. 41, pp. 2434–2440, 04 2014.
- [78] R. B. Scott, J. A. Goff, A. C. Naveira Garabato, and A. J. G. Nurser, “Global rate and spectral characteristics of internal gravity wave generation by geostrophic flow over topography,” *Journal of Geophysical Research*, vol. 116, 09 2011.

- [79] M. Bruno, J. Juan Alonso, A. Cózar, J. Vidal, A. Ruiz-Cañavate, F. Echevarría, and J. Ruiz, “The boiling-water phenomena at camarinal sill, the strait of gibraltar,” *Deep Sea Research Part II: Topical Studies in Oceanography*, vol. 49, pp. 4097–4113, 01 2002.
- [80] W. H. WHITE, “The norwegian north polar expedition, 1893–6,” *Nature*, vol. 74, pp. 485–486, 09 1906.
- [81] F. Nansen, *The Norwegian North Polar expedition 1893-1896 scientific results. 5.* Christiania Dybwad, 1906.
- [82] O. S. Eiff and P. Bonneton, “Lee-wave breaking over obstacles in stratified flow,” *Physics of Fluids*, vol. 12, pp. 1073–1086, 05 2000.
- [83] B. R. Sutherland, *Internal gravity waves.* Cambridge University Press, 2010.
- [84] B. Gyüre and I. M. Jánosi, “Stratified flow over asymmetric and double bell-shaped obstacles,” *Dynamics of Atmospheres and Oceans*, vol. 37, pp. 155–170, 08 2003.
- [85] S. B. VOSPER, I. P. CASTRO, W. H. SNYDER, and S. D. MOBBS, “Experimental studies of strongly stratified flow past three-dimensional orography,” *Journal of Fluid Mechanics*, vol. 390, pp. 223–249, 07 1999.
- [86] S. Vosper, “Inversion effects on mountain lee waves,” *Quarterly Journal of the Royal Meteorological Society*, vol. 130, pp. 1723–1748, 07 2004.
- [87] J. Sachsperger, S. Serafin, and V. Grubišić, “Lee waves on the boundary-layer inversion and their dependence on free-atmospheric stability,” *Frontiers in Earth Science*, vol. 3, 11 2015.
- [88] J. Sachsperger, S. Serafin, V. Grubišić, I. Stiperski, and A. Paci, “The amplitude of lee waves on the boundary-layer inversion,” *Quarterly Journal of the Royal Meteorological Society*, vol. 143, pp. 27–36, 12 2017.
- [89] Y. Yuan, J. Li, and Y. Cheng, “Validity ranges of interfacial wave theories in a two-layer fluid system,” *Acta Mechanica Sinica*, vol. 23, pp. 597–607, 09 2007.
- [90] J. R. Apel, “A new analytical model for internal solitons in the ocean,” *Journal of Physical Oceanography*, vol. 33, pp. 2247–2269, 11 2003.
- [91] J. Grue, “Nonlinear dead water resistance at subcritical speed,” *Physics of Fluids*, vol. 27, p. 082103, 08 2015.

- [92] E. R. Johnson and G. G. Vilenski, “Flow patterns and drag in near-critical flow over isolated orography,” *Journal of the Atmospheric Sciences*, vol. 61, pp. 2909–2918, 12 2004.
- [93] L. Lacaze, A. Paci, E. Cid, S. Cazin, O. Eiff, J. G. Esler, and E. R. Johnson, “Wave patterns generated by an axisymmetric obstacle in a two-layer flow,” *Experiments in Fluids*, vol. 54, 10 2013.
- [94] J. Grue, D. Bourgault, and P. S. Galbraith, “Supercritical dead water: effect of non-linearity and comparison with observations,” *Journal of Fluid Mechanics*, vol. 803, pp. 436–465, 08 2016.
- [95] H. F. Robey, “The generation of internal waves by a towed sphere and its wake in a thermocline,” *Physics of Fluids*, vol. 9, pp. 3353–3367, 11 1997.
- [96] J. Grue, “Calculating *FRAM*'s dead water,” *The Ocean in Motion*, pp. 41–53, 2018.
- [97] T. Miloh, M. P. Tulin, and G. Zilman, “Dead-water effects of a ship moving in stratified seas,” *Journal of Offshore Mechanics and Arctic Engineering*, vol. 115, pp. 105–110, 05 1993.
- [98] R. W. Yeung and T. C. Nguyen, “Waves generated by a moving source in a two-layer ocean of finite depth,” *Journal of Engineering Mathematics*, vol. 35, pp. 85–107, 1999.
- [99] D. Fructus and J. Grue, “Fully nonlinear solitary waves in a layered stratified fluid,” *Journal of Fluid Mechanics*, vol. 505, pp. 323–347, 04 2004.
- [100] J. Pedlosky, *Waves in the Ocean and Atmosphere: Introduction to Wave Dynamics*. Springer, New York, 2013.
- [101] F. K. Browand and C. D. Winant, “Blocking ahead of a cylinder moving in a stratified fluid: An experiment,” *Geophysical Fluid Dynamics*, vol. 4, pp. 29–53, 09 1972.
- [102] B. W. WILSON, “Seiches,” *Advances in Hydroscience*, pp. 1–94, 1972.
- [103] S. R. Massel, *Internal Gravity Waves in the Shallow Seas*. Cham Springer International Publishing, 2015.
- [104] P. Drazin, “Internal gravity waves with shear,” 1979.

- [105] J. E. Lewis, B. M. Lake, and D. R. S. Ko, “On the interaction of internal waves and surface gravity waves,” *Journal of Fluid Mechanics*, vol. 63, pp. 773–800, 05 1974.
- [106] C. Koop and L. Redekopp, “The interaction of long and short internal gravity waves: theory and experiment,” *Journal of Fluid Mechanics*, vol. 111, pp. 367–409, 1981.
- [107] R. R. Long, “Some aspects of the flow of stratified fluids: Ii. experiments with a two-fluid system,” *Tellus*, vol. 6, pp. 97–115, 05 1954.
- [108] D. Ko and Y. Cho, “A laboratory experiment on the surface and internal waves in two-layered fluids,” *Ocean Engineering*, vol. 146, pp. 257–267, 12 2017.
- [109] I. Ten and M. Kashiwagi, “Hydrodynamics of a body floating in a two-layer fluid of finite depth. part 1. radiation problem,” *Journal of Marine Science and Technology*, vol. 9, pp. 127–141, 10 2004.
- [110] D. P. Renouard and J.-M. Baey, “Two experimental studies of internal waves generated by tide-topography interaction,” *Dynamics of Atmospheres and Oceans*, vol. 19, pp. 205–232, 10 1993.
- [111] L. Boegman, G. N. Ivey, and J. Imberger, “The degeneration of internal waves in lakes with sloping topography,” *Limnology and Oceanography*, vol. 50, pp. 1620–1637, 09 2005.
- [112] P. Aghsaei and L. Boegman, “Experimental investigation of sediment resuspension beneath internal solitary waves of depression,” *Journal of Geophysical Research: Oceans*, vol. 120, pp. 3301–3314, 05 2015.
- [113] W. Xia, X. Zhao, R. Zhao, and X. Zhang, “Flume test simulation and study of salt and fresh water mixing influenced by tidal reciprocating flow,” *Water*, vol. 11, p. 584, 03 2019.
- [114] J. M. K. Dake and D. R. F. Harleman, “Thermal stratification in lakes: Analytical and laboratory studies,” *Water Resources Research*, vol. 5, pp. 484–495, 04 1969.
- [115] C. Gladstone, L. J. Ritchie, R. S. J. Sparks, and A. W. Woods, “An experimental investigation of density-stratified inertial gravity currents,” *Sedimentology*, vol. 51, pp. 767–789, 06 2004.
- [116] J. F. Price, R. A. Weller, and R. Pinkel, “Diurnal cycling: Observations and models of the upper ocean response to diurnal heating, cooling, and wind mixing,” *Journal of Geophysical Research*, vol. 91, p. 8411, 1986.

- [117] R. Ferrari and D. L. Rudnick, “Thermohaline variability in the upper ocean,” *Journal of Geophysical Research: Oceans*, vol. 105, pp. 16857–16883, 07 2000.
- [118] T. B. Benjamin, “Internal waves of permanent form in fluids of great depth,” *Journal of Fluid Mechanics*, vol. 29, pp. 559–592, 09 1967.
- [119] J.-L. Pinault, “Resonantly forced baroclinic waves in the oceans: Subharmonic modes,” *Journal of Marine Science and Engineering*, vol. 6, p. 78, 07 2018.
- [120] M. Economidou and G. R. Hunt, “Density stratified environments: the double-tank method,” *Experiments in Fluids*, vol. 46, pp. 453–466, 10 2008.
- [121] G. Oster, “Density gradients,” *Scientific American*, vol. 213, pp. 70–76, 08 1965.
- [122] S. Davarpanah Jazi, M. G. Wells, J. Peakall, R. M. Dorrell, R. E. Thomas, G. M. Keevil, S. E. Darby, J. Sommeria, S. Viboud, and T. Valran, “Influence of coriolis force upon bottom boundary layers in a large-scale gravity current experiment: Implications for evolution of sinuous deep-water channel systems,” *Journal of Geophysical Research: Oceans*, vol. 125, no. 3, p. e2019JC015284, 2020.
- [123] A. Cuthbertson, J. Laanearu, M. Carr, J. Sommeria, and S. Viboud, “Blockage of saline intrusions in restricted, two-layer exchange flows across a submerged sill obstruction,” *Environmental Fluid Mechanics*, vol. 18, no. 1, pp. 27–57, 2018.
- [124] S. B. Dalziel, G. O. Hughes, and B. R. Sutherland, “Whole-field density measurements by ‘synthetic schlieren’,” *Experiments in Fluids*, vol. 28, pp. 322–335, 04 2000.
- [125] L. Gostiaux, H. Didelle, S. Mercier, and T. Dauxois, “A novel internal waves generator,” *Experiments in Fluids*, vol. 42, pp. 123–130, 10 2006.
- [126] L. Boegman, G. N. IVEY, and J. IMBERGER, “The energetics of large-scale internal wave degeneration in lakes,” *Journal of Fluid Mechanics*, vol. 531, pp. 159–180, 05 2005.
- [127] D. A. HORN, J. IMBERGER, and G. N. IVEY, “The degeneration of large-scale interfacial gravity waves in lakes,” *Journal of Fluid Mechanics*, vol. 434, pp. 181–207, 05 2001.
- [128] M. J. Mercier, R. Vasseur, and T. Dauxois, “Resurrecting dead-water phenomenon,” *Nonlinear Processes in Geophysics*, vol. 18, pp. 193–208, 03 2011.

- [129] I. Stiperski, S. Serafin, A. Paci, H. Ágústsson, A. Belleudy, R. Calmer, K. Horvath, C. Knigge, J. Sachsperger, L. Strauss, and V. Grubišić, “Water tank experiments on stratified flow over double mountain-shaped obstacles at high-reynolds number,” *Atmosphere*, vol. 8, p. 13, 01 2017.
- [130] H. Mu, X. Chen, and Q. Li, “Laboratory experiments on an internal solitary wave over a triangular barrier,” *Journal of Ocean University of China*, vol. 18, pp. 1061–1069, 08 2019.
- [131] G. La Forgia, C. Adduce, and F. Falcini, “Laboratory investigation on internal solitary waves interacting with a uniform slope,” *Advances in Water Resources*, vol. 120, pp. 4–18, 10 2018.
- [132] D. Bourgault and C. Richards, “A laboratory experiment on internal solitary waves,” *American Journal of Physics*, vol. 75, pp. 666–670, 07 2007.
- [133] C. Kranenburg and J. D. Pietrzak, “Internal lee waves in turbulent two-layer flow,” *Journal of Hydraulic Engineering*, vol. 115, pp. 1352–1370, 10 1989.
- [134] “Instructions for lego 4005 tug boat,” 1982.
- [135] J. R. Carpenter, E. W. Tedford, E. Heifetz, and G. A. Lawrence, “Instability in stratified shear flow: Review of a physical interpretation based on interacting waves,” *Applied Mechanics Reviews*, vol. 64, 11 2011.
- [136] O. Motygin and N. Kuznetsov, “The wave resistance of a two-dimensional body moving forward in a two-layer fluid,” *Journal of Engineering Mathematics*, vol. 32, pp. 53–72, 1997.
- [137] D. Durran, “Lee waves and mountain waves,” *Encyclopedia of Atmospheric Sciences*, pp. 1161–1169, 2003.
- [138] B. R. Sutherland, “Large-amplitude internal wave generation in the lee of step-shaped topography,” *Geophysical Research Letters*, vol. 29, pp. 16–1–16–4, 08 2002.
- [139] A. P. French, *Vibrations and waves, M.I.T. introductory physics series, Taylor & Francis*. Boca Raton Crc Press, 1971.
- [140] K. N. Stevens, *Acoustic phonetics*. MIT Press, 2000.
- [141] S. Bondevik, B. Gjevik, and M. B. Sørensen, “Norwegian seiches from the giant 2011 tohoku earthquake,” *Geophysical Research Letters*, vol. 40, pp. 3374–3378, 07 2013.

- [142] L. Arneborg and B. Liljebladh, “The internal seiches in gullmar fjord. part i: Dynamics,” *Journal of Physical Oceanography*, vol. 31, pp. 2549–2566, 09 2001.
- [143] D. L. McCollum, L. G. Echeverri, S. Busch, S. Pachauri, S. Parkinson, J. Rogelj, V. Krey, J. C. Minx, M. Nilsson, A.-S. Stevance, and K. Riahi, “Connecting the sustainable development goals by their energy inter-linkages,” *Environmental Research Letters*, vol. 13, p. 033006, 03 2018.
- [144] N. S. Ouedraogo, “Opportunities, barriers and issues with renewable energy development in africa: a comprehensible review,” *Current Sustainable/Renewable Energy Reports*, vol. 6, pp. 52–60, 04 2019.
- [145] F. D. Longa and B. van der Zwaan, “Heart of light: an assessment of enhanced electricity access in africa,” *Renewable and Sustainable Energy Reviews*, vol. 136, p. 110399, 02 2021.
- [146] U. Nations, “The sustainable development goals report,” 2020.
- [147] A. Boudghene Stambouli, Z. Khiat, S. Flazi, H. Tanemoto, M. Nakajima, H. Isoda, F. Yokoyama, S. Hannachi, K. Kurokawa, M. Shimizu, H. Koinuma, and N. Yassaa, “Trends and challenges of sustainable energy and water research in north africa: Sahara solar breeder concerns at the intersection of energy/water,” *Renewable and Sustainable Energy Reviews*, vol. 30, pp. 912–922, 02 2014.
- [148] A. López-Ballesteros, J. Beck, J. Helmschrot, and M. Saunders, “Harmonised observations of climate forcing across africa: an assessment of existing approaches and their applicability,” *Environmental Research Letters*, vol. 15, p. 075003, 07 2020.
- [149] Q. Wang, L. Wang, and R. Li, “Renewable energy and economic growth revisited: The dual roles of resource dependence and anticorruption regulation,” *Journal of Cleaner Production*, vol. 337, p. 130514, 02 2022.
- [150] S. Adams, E. K. M. Klobodu, and A. Apio, “Renewable and non-renewable energy, regime type and economic growth,” *Renewable Energy*, vol. 125, pp. 755–767, 09 2018.
- [151] M. S. Ben Aïssa, M. Ben Jebli, and S. Ben Youssef, “Output, renewable energy consumption and trade in africa,” *Energy Policy*, vol. 66, pp. 11–18, 03 2014.

- [152] I. K. Maji, C. Sulaiman, and A. S. Abdul-Rahim, “Renewable energy consumption and economic growth nexus: A fresh evidence from west africa,” *Energy Reports*, vol. 5, p. 384–392, 11 2019.
- [153] D. M. Ibrahim and S. A. Hanafy, “Do energy security and environmental quality contribute to renewable energy? the role of trade openness and energy use in north african countries,” *Renewable Energy*, vol. 179, pp. 667–678, 12 2021.
- [154] A. Oppong, M. Jie, K. N. Acheampong, and M. A. Sakyi, “Variations in the environment, energy and macroeconomic interdependencies and related renewable energy transition policies based on sensitive categorization of countries in africa,” *Journal of Cleaner Production*, vol. 255, p. 119777, 05 2020.
- [155] K. Engeland, M. Borga, J.-D. Creutin, B. François, M.-H. Ramos, and J.-P. Vidal, “Space-time variability of climate variables and intermittent renewable electricity production – a review,” *Renewable and Sustainable Energy Reviews*, vol. 79, pp. 600–617, 11 2017.
- [156] S. Sterl, S. Liersch, H. Koch, N. P. M. v. Lipzig, and W. Thiery, “A new approach for assessing synergies of solar and wind power: implications for west africa,” *Environmental Research Letters*, vol. 13, p. 094009, 09 2018.
- [157] J. Jurasz, F. Canales, A. Kies, M. Guezgouz, and A. Beluco, “A review on the complementarity of renewable energy sources: Concept, metrics, application and future research directions,” *Solar Energy*, vol. 195, pp. 703–724, 01 2020.
- [158] S. Abebe Asfaw, M. Child, U. Caldera, and C. Breyer, “Exploiting wind-solar resource complementarity to reduce energy storage need,” *AIMS Energy*, vol. 8, pp. 749–770, 2020.
- [159] F. Weschenfelder, G. de Novaes Pires Leite, A. C. Araújo da Costa, O. de Castro Vilela, C. M. Ribeiro, A. A. Villa Ochoa, and A. M. Araújo, “A review on the complementarity between grid-connected solar and wind power systems,” *Journal of Cleaner Production*, vol. 257, p. 120617, 06 2020.
- [160] M. Guezgouz, J. Jurasz, M. Chouai, H. Bloomfield, and B. Bekkouche, “Assessment of solar and wind energy complementarity in algeria,” *Energy Conversion and Management*, vol. 238, p. 114170, 06 2021.
- [161] A. A. Prasad, R. A. Taylor, and M. Kay, “Assessment of solar and wind resource synergy in australia,” *Applied Energy*, vol. 190, pp. 354–367, 03 2017.

- [162] A. Z. Sahin, “Applicability of wind-solar thermal hybrid power systems in the north-eastern part of the arabian peninsula,” *Energy Sources*, vol. 22, pp. 845–850, 10 2000.
- [163] D. Heide, L. von Bremen, M. Greiner, C. Hoffmann, M. Speckmann, and S. Bofinger, “Seasonal optimal mix of wind and solar power in a future, highly renewable europe,” *Renewable Energy*, vol. 35, pp. 2483–2489, 11 2010.
- [164] W. Zappa and M. van den Broek, “Analysing the potential of integrating wind and solar power in europe using spatial optimisation under various scenarios,” *Renewable and Sustainable Energy Reviews*, vol. 94, pp. 1192–1216, 10 2018.
- [165] J. Widen, “Correlations between large-scale solar and wind power in a future scenario for sweden,” *IEEE Transactions on Sustainable Energy*, vol. 2, pp. 177–184, 04 2011.
- [166] S. Jerez, R. Trigo, A. Sarsa, R. Lorente-Plazas, D. Pozo-Vázquez, and J. Montávez, “Spatio-temporal complementarity between solar and wind power in the iberian peninsula,” *Energy Procedia*, vol. 40, pp. 48–57, 2013.
- [167] F. Santos-Alamillos, D. Pozo-Vázquez, J. Ruiz-Arias, L. Von Bremen, and J. Tovar-Pescador, “Combining wind farms with concentrating solar plants to provide stable renewable power,” *Renewable Energy*, vol. 76, pp. 539–550, 04 2015.
- [168] T. Guozden, J. P. Carbajal, E. Bianchi, and A. Solarte, “Optimized balance between electricity load and wind-solar energy production,” *Frontiers in Energy Research*, vol. 8, 02 2020.
- [169] L. Liu, Z. Wang, Y. Wang, J. Wang, R. Chang, G. He, W. Tang, Z. Gao, J. Li, C. Liu, L. Zhao, D. Qin, and S. Li, “Optimizing wind/solar combinations at finer scales to mitigate renewable energy variability in china,” *Renewable and Sustainable Energy Reviews*, vol. 132, p. 110151, 10 2020.
- [170] J. Jurasz, J. Mikulik, P. B. Dąbek, M. Guezgouz, and B. Kaźmierczak, “Complementarity and ‘resource droughts’ of solar and wind energy in poland: An era5-based analysis,” *Energies*, vol. 14, p. 1118, 02 2021.
- [171] H. Hersbach, B. Bell, P. Berrisford, S. Hirahara, A. Horányi, J. Muñoz-Sabater, J. Nicolas, C. Peubey, R. Radu, D. Schepers, A. Simmons, C. Soci, S. Abdalla, X. Abellan, G. Balsamo, P. Bechtold, G. Biavati, J. Bidlot, M. Bonavita, G. Chiara, P. Dahlgren, D. Dee, M. Diamantakis, R. Dragani, J. Flemming, R. Forbes,

- M. Fuentes, A. Geer, L. Haimberger, S. Healy, R. J. Hogan, E. Hólm, M. Janisková, S. Keeley, P. Laloyaux, P. Lopez, C. Lupu, G. Radnoti, P. Rosnay, I. Rozum, F. Vamborg, S. Villaume, and J. Thépaut, “The era5 global reanalysis,” *Quarterly Journal of the Royal Meteorological Society*, vol. 146, pp. 1999–2049, 06 2020.
- [172] P. Kiss, L. Varga, and I. M. Jánosi, “Comparison of wind power estimates from the ecmwf reanalyses with direct turbine measurements,” *Journal of Renewable and Sustainable Energy*, vol. 1, p. 033105, 05 2009.
- [173] J. Ramon, L. Lledó, V. Torralba, A. Soret, and F. J. Doblas-Reyes, “What global reanalysis best represents near-surface winds?,” *Quarterly Journal of the Royal Meteorological Society*, vol. 145, pp. 3236–3251, 08 2019.
- [174] M. Lydia, S. S. Kumar, A. I. Selvakumar, and G. E. Prem Kumar, “A comprehensive review on wind turbine power curve modeling techniques,” *Renewable and Sustainable Energy Reviews*, vol. 30, pp. 452–460, 02 2014.
- [175] P. Kiss and I. M. Jánosi, “Limitations of wind power availability over europe: a conceptual study,” *Nonlinear Processes in Geophysics*, vol. 15, pp. 803–813, 11 2008.
- [176] I. M. Jánosi, “Model study of combined wind and solar electricity production in hungary,” *Journal of Renewable and Sustainable Energy*, vol. 5, p. 033102, 05 2013.
- [177] M. Z. Jacobson and V. Jadhav, “World estimates of pv optimal tilt angles and ratios of sunlight incident upon tilted and tracked pv panels relative to horizontal panels,” *Solar Energy*, vol. 169, pp. 55–66, 07 2018.
- [178] C. Fountoukis, B. Figgis, L. Ackermann, and M. A. Ayoub, “Effects of atmospheric dust deposition on solar pv energy production in a desert environment,” *Solar Energy*, vol. 164, pp. 94–100, 04 2018.
- [179] S. Pulipaka and R. Kumar, “Analysis of soil distortion factor for photovoltaic modules using particle size composition,” *Solar Energy*, vol. 161, pp. 90–99, 02 2018.
- [180] T. M. Alnasser, A. M. Mahdy, K. I. Abass, M. T. Chaichan, and H. A. Kazem, “Impact of dust ingredient on photovoltaic performance: An experimental study,” *Solar Energy*, vol. 195, pp. 651–659, 01 2020.
- [181] P. M. M. Soares, D. C. A. Lima, A. Semedo, W. Cabos, and D. V. Sein, “Climate change impact on northwestern african offshore wind energy resources,” *Environmental Research Letters*, vol. 14, p. 124065, 12 2019.

- [182] H. F. Inman and E. L. Bradley, “The overlapping coefficient as a measure of agreement between probability distributions and point estimation of the overlap of two normal densities,” *Communications in Statistics - Theory and Methods*, vol. 18, pp. 3851–3874, 01 1989.
- [183] A. M. Franco-Pereira, C. T. Nakas, B. Reiser, and M. Carmen Pardo, “Inference on the overlap coefficient: The binormal approach and alternatives,” *Statistical Methods in Medical Research*, vol. 30, pp. 2672–2684, 10 2021.
- [184] G. Ren, J. Wan, J. Liu, and D. Yu, “Spatial and temporal correlation analysis of wind power between different provinces in china,” *Energy*, vol. 191, p. 116514, 01 2020.
- [185] C. Lamancusa and K. Wagstrom, “Global transport of dust emitted from different regions of the sahara,” *Atmospheric Environment*, vol. 214, p. 116734, 10 2019.
- [186] I. Koren, Y. J. Kaufman, R. Washington, M. C. Todd, Y. Rudich, J. V. Martins, and D. Rosenfeld, “The bodélé depression: a single spot in the sahara that provides most of the mineral dust to the amazon forest,” *Environmental Research Letters*, vol. 1, p. 014005, 10 2006.
- [187] O. Krishan and S. Suhag, “An updated review of energy storage systems: Classification and applications in distributed generation power systems incorporating renewable energy resources,” *International Journal of Energy Research*, vol. 43, pp. 6171–6210, 11 2018.
- [188] N. Merzouk, “Wind energy potential of algeria,” *Renewable Energy*, vol. 21, pp. 553–562, 11 2000.
- [189] M. Djamai and N. K. Merzouk, “Wind farm feasibility study and site selection in adrar, algeria,” *Energy Procedia*, vol. 6, pp. 136–142, 2011.
- [190] A. B. Stambouli, Z. Khiat, S. Flazi, and Y. Kitamura, “A review on the renewable energy development in algeria: Current perspective, energy scenario and sustainability issues,” *Renewable and Sustainable Energy Reviews*, vol. 16, pp. 4445–4460, 09 2012.
- [191] S. M. Boudia, A. Benmansour, and M. A. Tabet Hellal, “Wind resource assessment in algeria,” *Sustainable Cities and Society*, vol. 22, pp. 171–183, 04 2016.

- [192] H. Daaou Nedjari, S. K. Haddouche, A. Balehouane, and O. Guerri, “Optimal windy sites in algeria: Potential and perspectives,” *Energy*, vol. 147, pp. 1240–1255, 03 2018.
- [193] S. M. Boudia and J. a. A. Santos, “Assessment of large-scale wind resource features in algeria,” *Energy*, vol. 189, p. 116299, 12 2019.
- [194] H. Ounis and N. Aries, “On the wind resource in algeria: Probability distributions evaluation,” *Proceedings of the Institution of Mechanical Engineers, Part A: Journal of Power and Energy*, vol. 235, pp. 1187–1204, 11 2020.